

Republic of Iraq
Ministry of Higher Education and Scientific Research
University of Misan/College of Engineering
Department of Civil Engineering



BEHAVIOR OF DEEP BEAMS WITH EMBEDDED FUNCTIONALLY GRADED CONCRETE STRUTS

By

Hussein Kareem Hashim

B.Sc. Civil Engineering, 2017

A THESIS

Submitted in Partial Fulfillment of the
Requirements for the Master of Science Degree in Civil Engineering

The University of Misan

June 2025

Thesis Supervisor: Prof. Dr. Abdulkhaliq A. Jaafer

Assist. Prof. Dr. Hayder Al-Khazraji

بِسْمِ اللَّهِ الرَّحْمَنِ الرَّحِيمِ

فَأَمَّا الزَّبَدُ فَيَذْهَبُ جُفَاءً^ص وَأَمَّا مَا يَنْفَعُ
النَّاسَ فَيَمْكُثُ فِي الْأَرْضِ^ج كَذَلِكَ يَضْرِبُ
اللَّهُ الْأَمْثَالَ

سورة الرعد - الآية 17

ABSTRACT

This study experimentally investigates the influence of alternative shear reinforcement systems on the shear performance of deep beams. It also aims to identify the optimal distribution of concrete types in hybrid deep beams to minimize cost and weight while maintaining structural integrity. Fifteen deep beam specimens were cast, each with identical dimensions: 1200 mm in length, 500 mm in depth, and 150 mm in width. All specimens were tested under a single-point loading system with a constant shear span-to-effective depth ratio ($a/d = 1$). The key variables examined in this study were the shape and type of reinforcement used in the strut region, as well as the hybridization of concrete. High-strength concrete was applied in high-stress regions including the strut, strut ribs, and tie region, while normal-strength concrete was used in the remaining regions. The specimens were divided into four groups. The first group, serving as the control beams, consisted of four beams with conventional strut reinforcement. Two had triangular strut reinforcement and two had arched reinforcement; each pair utilized either high- or normal-strength concrete. The second group comprised four hybrid arched deep beams with conventional reinforcement, which varied in the number of added ribs supporting the arch action and in tie reinforcement methods. The third group featured hybrid arched reinforcement using angle steel sections (40×40×4) mm instead of conventional strut reinforcement. These specimens varied in the quantity of steel and in the inclusion of ribs made from angle sections. The fourth group included four specimens with triangular hybrid reinforcement using angle steel sections (40×40×4) mm, which varied in the amount of steel used and in the partial replacement of tie reinforcement.

The arched hybrid beams showed improvements over the normal-strength concrete control beam in first cracking load, ultimate load capacity, stiffness,

ductility, and energy absorption by 33.3%, 74.2%, 99%, 40%, and 108.3%, respectively. Compared to the high-strength concrete control beam, improvements were 20%, 31.7%, 63.3%, 16%, and 30.4%, respectively.

The triangular hybrid beams demonstrated enhancements in ultimate load capacity, stiffness, ductility, and energy absorption by 75%, 235.6%, 116.4%, and 77.2%, respectively, compared to the normal-strength concrete control beam. Against the high-strength concrete control beam, the corresponding improvements were 25.6%, 77%, 96%, and 51.8%, respectively.

SUPERVISOR CERTIFICATION

I certify that the preparation of this thesis entitled " **Behavior of Deep Beams with Embedded Functionally Graded Concrete Struts**" was presented by " **Hussein Kareem Hashim**", and prepared under my supervision at The University of Misan, Department of Civil Engineering, College of Engineering, as a partial fulfillment of the requirements for the degree of Master of Science in Civil Engineering (Structural Engineering).

Signature:

Prof. Dr. Abdulkhaliq A. Jaafer

Date:

Signature:

Assist. Prof. Dr. Hayder Al-Khazraji

Date:

In view of the available recommendations, I forward this thesis for discussion by the examining committee.

Signature:

Assist Prof. Dr. Mortada Abass Abd Ali

(Head of Civil Eng. Department)

Date:

EXAMINING COMMITTEE'S REPORT

We certify that we, the examining committee, have read the thesis titled **(Behavior of Deep Beams with Embedded Functionally Graded Concrete Struts)** which is being submitted by (**Hussein Kareem Hashim**), and examined the student in its content and in what is concerned with it, and that in our opinion, it meets the standard of a thesis for the degree of Master of Science in Civil Engineering (Structures).

Signature:

Signature:

Name: Prof. Dr. Abdulkhaliq A. Jaafer Name: Assist. Prof. Dr. Hayder Al-

Khazraji

(Supervisor)

(Co-supervisor)

Date: / /2025

Date: / /2025

Signature:

Signature:

Name:

Name:

(Chairman)

(Member)

Date: / /2025

Date: / /2025

Signature:

Name:

(Member)

Date: / /2025

Approval of the College of Engineering:

Signature:

Name: Prof. Dr. Abbas Oda Dawood

Dean, College of Engineering

Date: / /2025

DEDICATION

- ❖ To Imam Al-Mahdi (may Allah hasten his reappearance)
- ❖ To Sayyed Hassan Nasrallah

ACKNOWLEDGEMENTS

In the name of Allah, the Most Gracious and the Most Merciful, all praise to Allah for His strength and His blessing in completing this thesis.

I would like to express my cordial thanks and deepest gratitude to my supervisors, **Prof. Dr. Abdulkhaliq A. Jaafer** and **Assist. Prof. Dr. Hayder Al-Khazraji** whom I had the honor of being under their supervision, for their advice, help, and encouragement during the course of this study.

I would like to extend my thanks to **Prof. Dr. Abbas Oda Dawood** Dean of the College of Engineering, and **Assist Prof. Dr. Murtada Abass Abd Ali**, the Head of Civil Engineering Department.

Special thanks go to **my parents, my brothers, my wife, my friends and my son (Mohammed Al-Mahdi)**

TABLE OF CONTENTS

Abstract.....	I
Supervisor Certification.....	III
EXAMINING COMMITTEE’S REPORT.....	IV
DEDICATION.....	V
ACKNOWLEDGEMENTS	VI
TABLE OF CONTENTS	VII
LIST OF TABLES.....	XI
LIST OF FIGURES.....	XIII
CHAPTER ONE:INTRODUCTION.....	1
1.1 General.....	1
1.2 Deep Beam Definition	3
1.3 Behavior of Deep Beam.....	4
1.4 Failure Modes and Cracking Patterns.....	4
1.4.1 Diagonal-splitting failure	5
1.4.2 Shear-Compression failure.....	5
1.4.3 Compression strut failure	5
1.4.4 Anchorage failure.....	5
1.4.5 Bearing failure.....	5
1.4.6 Flexural failure	5
1.5 Hybrid Concrete.....	6
1.6 High Strength Concrete (HSC)	9

1.7	Aims of the study	10
1.8	Thesis Organization	10
CHAPTER TWO:LITERATURE REVIEW.....		12
4.1.....		26
4.2.....		26
4.3.....		26
1.9	Deep Beams Incorporating Steel Sections.....	26
CHAPTER THREE:EXPERIMENTAL PROGRAM		46
3.1	Introduction.....	46
1.1	Specimens Description and Coding	46
1.11	Materials Properties	51
1.11.1	Cement	51
1.11.2	Fine Aggregate (Sand)	52
1.11.3	Coarse Aggregate (Gravel)	53
1.11.4	Water	54
1.11.5	Silica Fume.....	54
1.11.6	Super Plasticizer.....	55
1.11.7	Steel Bars.....	56
1.11.8	Steel Sections	57
1.11.9	Welding Wires	57
1.12	Proportions of Concrete Mix	58
1.13	Mixing Methods.....	59
1.13.1	Normal Strength Concrete (NSC).....	59
1.13.2	High Strength Concrete (HSC)	60
1.14	Concrete Testing	60

1.14.1	Workability test.....	61
1.14.2	Compressive strength.....	61
1.14.3	Tensile Strength	62
1.14.4	Flexural Strength.....	64
1.14.5	Modulus of Elasticity (E_c):.....	64
1.15	Preparation of Test Specimens	65
1.15.1	Curing the Specimens.	69
1.16	Instrumentation and Equipment of the Test	69
1.16.1	Flexural Test Machine.....	69
1.16.2	Data Logger.....	70
1.16.3	Strain Gauges	71
1.16.4	Deflection measurement (LVDT)	71
1.17	Testing Procedure	72
CHAPTER Four:RESULTS		AND
DISCUSSION 72		
2.3	General.....	72
2.4	Ultimate Load	73
2.4.1	First group	73
2.4.2	Second group (G2)	74
2.4.3	Third group (G3)	76
2.4.4	Fourth group (G4)	79
3.3	Load - Deflection Curves.....	81
2.4.5	Control Beam Specimens (G1)	82
2.4.6	Hybrid Beams – Arch Strut Specimens	83
2.4.6.1	Reinforced Specimens with Steel Bars.....	83

2.4.6.2 Reinforced Specimens with Steel Section	85
2.4.7 Hybrid Beams – Triangle Strut Specimens.....	87
2.5 Effective Stiffness	89
2.6 Ductility index	91
2.7 Energy Absorption Capacity.....	94
2.8 Cracks propagation characteristics	97
2.8.1.1 First group specimens	97
2.8.1.2 Second Group Specimens (G2)	102
2.8.1.3 Third Group Specimens (G3)	106
2.8.1.4 Fourth Group Specimens (G4)	111
2.9 Concrete Surface Strain	114
2.9.1 Compressive strain	116
2.9.1.1 Strut strain.....	116
2.9.1.2 Strut-Ribs strain	116
2.9.2 Tensile strain	117
CHAPTER FIVE: CONCLUSIONS AND RECOMMENDATIONS...	119
3.3 Conclusions.....	119
3.4 Recommendation for Future Works	121
references	130

LIST OF TABLES

Table 3.1 Used parameters.	46
Table 3.2 details of deep beams.....	47
Table 3.3 Chemical composition of cement.	52
Table 3.4 Properties of cement.	52
Table 3.5 Grading of the fine aggregates.	52
Table 3.6 Grading of the fine aggregates.	54
Table 3.7 Typical properties for Silica fume [65].	55
Table 3.8 Chemical and physical properties of Silica fume.....	55
Table 3.9 Properties of Super Plasticizer[66]	56
Table 3.10 Properties of reinforcing bars (average) [67]	56
Table 3.11 Properties of steel sections (average) [68]	57
Table 3.12 Properties of welding wires [69].	58
Table 3.13 Proportions of High Strength Concrete (Trail Mix).....	59
Table 3.14 Proportions of Normal Strength Concrete.....	59
Table 3.15 Slump test results [70].	61
Table 3.16 Compressive strength test results.	62
Table 3.17 Splitting test results.	63
Table 3.18 Rupture test results.	64
Table 3.19 Modulus of Elasticity test results.	65
Table 4.1 Ultimate Load and Failure Modes for (G1)	74
Table 4.2 Ultimate Load and Failure Modes for (G2)	76
Table 4.3 Ultimate Load and Failure Modes for (G3)	78
Table 4.4 Ultimate Load and Failure Modes for (G4)	81

Table 4.5 The effective stiffness test results for the tested beams	89
Table 4.6 Ductility index results for all tested specimens.....	92
Table 4.7 Toughness results of all examined specimens.....	95
Table 4.8 The Concrete Surface Strain for All Tested Specimens.....	115

LIST OF FIGURES

Figure 1.1 An example of deep beam.	2
Figure 1.2 ACI limitations for Deep Beam.	3
Figure 1.3 Effective depth ratio (a/d) of the deep beam.	3
Figure 1.4 Common failure modes in deep beam.	6
Figure 1.5 Trajaction of stress in deep beams.	9
Figure 2.1 (a) The ANSYS-obtained crack patterns, and (b) cracks produced during the experiment.	13
Figure 2.2 (a) Specifications of the first group's deep beams, and (b) Specifications of the second group's deep beams .	14
Figure 2.3. Different (a/d) ratio using in the study of .	15
Figure 2.4 Reinforcement Details for the using samples in this study .	16
Figure 2.5 Relationship between design factors and dimensionless diagonal tension cracking strength $V_{cr,t}/(\sqrt{f_c'}bd)$.	17
Figure 2.6 (a)The relationship between the web reinforcement ratio and initial stiffness. (b)Web Reinforcement Ratio and Stiffness at Maximum Load Relationship. (c)The relationship between the web reinforcement ratio and stiffness at failure .	18
Figure 2.7 Reinforcement Details and dimensions for the using deep beams in study of reference.	19
Figure 2.8. Specimen dimensions and the distribution of load technique	20
Figure 2.9. Failure modes for the deep beams	20
Figure 2.10. Specimen cross sections and its details .	25
Figure 2.11 The holes are strengthened with steel palates and studs .	26
Figure 2.12. Cross sectional details of the tested beams [.	28
Figure 2.13 Cross section and the embedded I-section steel plate	28
Figure 2.14 Type of the strut's reinforcement .	29

Figure 2.15 Specimen reinforcement details using steel plates.	30
Figure 2.16 Types of the tested deep beams.	31
Figure 2.17 Details of the specimens and loading.	32
Figure 2.18 Details and dimensions of the tested specimen and loading.	33
Figure 2.19 The loading and specimen's dimensions of the deep beams.	34
Figure 2.20 Dimensions and cross section details of the beams.	35
Figure 2.21 Cross sections details and dimensions of the tested beams.	36
Figure 2.22 Dimensions and layered method of the graded concrete	36
Figure 2.23 Dimensions and hybridization method of the tested beams.	38
Figure 2.24 Dimensions and hybridization arrangement of the deep beams.	39
Figure 2.25 hybridization method of tested deep beams	39
Figure 2.26 Hybrid deep beam models for this study.	40
Figure 2.27 Hybrid deep beam models for this study.	41
Figure 2.28 Details of the geometry of the Hybrid deep beams.	42
Figure 2.29 Details of the Hybrid deep beams.	43
Figure 2.30 Details of the Hybrid deep beams.	44
Figure 3.1 Group one (G1) deep beams details.	48
Figure 3.2 Group two (G2) deep beams details.	49
Figure 3.3 Group three (G3) deep beams details.	50
Figure 3.4 Group four (G4) deep beams details.	51
Figure 3.5 Sieve analysis of fine aggregate compared to standard limits.	53
Figure 3.6 Stages of hand-sieving, washing and packing gravel.	53
Figure 3.7 Sieve analysis of coarse aggregate compared to standard limits.	54
Figure 3.8 Reinforcement bar testing machine.	56
Figure 3.9 Steel section used in this study.	57

Figure 3.10 welding wire type.	58
Figure 3.11 Mixer (1) for normal strength concrete.	59
Figure 3.12 Mixer (2) for high strength concrete.	60
Figure 3.13 Slump test for (A)HSC, (B)NSC.	61
Figure 3.14 Sampling and curing of concrete specimens.	62
Figure 3.15 Compressive strength test.	62
Figure 3.16 Splitting tensile strength test for (A)HSC, (B)NSC.	63
Figure 3.17 Flexural strength test for (A)HSC, (B)NSC.	64
Figure 3.18 Modulus of Elasticity test.	65
Figure 3.19 Formwork Details.	66
Figure 3.20 Reinforcement Details.	66
Figure 3.21 Welding process.	67
Figure 3.22 Preparing specimens for casting process.	67
Figure 3.23 Casting process procedure.	68
Figure 3.24 Separating plate lifting and vibrator use.	68
Figure 3.25 Finishing process.	69
Figure 3.26 Curing process.	69
Figure 3.27 Flexural Test Machine.	70
Figure 3.28 Data logger.	70
Figure 3.29 Concrete strain gauges and their glue.	71
Figure 3.30 Linear variable differential transformers (LVDT).	71
Figure 3.31 painting specimens.	72
Figure 3.32 rubber pads locations.	73
Figure 3.33 Marking cracks in the tested beams	73
Figure 3.34 Test setting	74

Figure 4.1. Load - Deflection Curves for specimens of control beams.	83
Figure 4.2 Load - Deflection Curves for the second group specimens (G2).	85
Figure 4.3 Load - Deflection Curves for third group specimens (G3).	86
Figure 4.4 Load - Deflection Curves for fourth group specimens (G4).	88
Figure 4.5 The effective stiffness results for all the tested beams	90
Figure 4.6 Calculating the ductility ratio using displacement ratio method	92
Figure 4.7 Ductility index results for all tested specimens.	93
Figure 4.8 Toughness results of all examined specimens	95
Figure 4.9 Cracks propagation for specimen G1-CO-1.	98
Figure 4.10 Cracks propagation for specimen G1-CO-2.	99
Figure 4.11 Cracks propagation for specimen G1-CO-3.	101
Figure 4.12 Cracks propagation for specimen G1-CO-4.	102
Figure 4.13 Cracks propagation for specimen G2-HA-B-1.	103
Figure 4.14 Cracks propagation for specimen G2-HA-B-2.	104
Figure 4.15 Cracks propagation for specimen G2-HA-B-3.	105
Figure 4.16 Cracks propagation for specimen G2-HA-B-4.	106
figure 4.17 cracks propagation for specimen G3-HA-S-1.	108
Figure 4.18 Cracks propagation for specimen G3-HA-S-2.	109
Figure 4.19 Cracks propagation for specimen G3-HA-S-3.	110
Figure 4.20 Cracks propagation for specimen G4-HT-S-1.	112
Figure 4.21 Cracks propagation for specimen G4-HT-S-2.	112
Figure 4.22 Cracks propagation for specimen G4-HT-S-3.	113
Figure 4.23 Cracks Propagation For (G4-HT-S-4).	113
Figure 4.24 Strain gauges location.	115
Figure 4.25 Compressive Strain For All Tested Specimens	116

Figure 4.26 Compressive Strain at the middle of the ribs.	117
Figure 4.27 The tensile strain results for all tested specimens	118

LIST OF SYMBOLES

f'_c	Cylinder concrete compressive strength in MPa
f_{cu}	Cube Compressive Strength in MPa
\emptyset	Diameter of Reinforcement bar mm
ϵ_c	Concrete Strain
E_c	Concrete modulus of elasticity, GPa
f_r	Modulus of Rupture of Concrete in MPa
f_t	Tensile Strength of Concrete in MPa
f_y	Steel Rebar Yield Stress in MPa
Δ_y	Yield Deflection in mm
Δ_u	Ultimate Deflection in mm

LIST OF ABBREVIATIONS

ASCE	American Society of Civil Engineers
ASTM	American Society of Testing and Materials
LWC	Lightweight Concrete
ECC	Engineering Cementitious Composite
R.C	Reinforcement Concrete
FRP	Fiber-reinforced polymer
CFRP	Carbon fiber reinforced polymer
GFRP	Glass Fiber Reinforced Polymer
RPC	Reactive powder concrete
UHPC	Ultra-High Performance Concrete
SFHSC	Steel fiber high strength concrete
HSC	High Strength Concrete
NSC	Normal strength concrete
SF	Steel fiber
IQS	Iraqi Standard
w/c	Water-to-cement ratio
R.O	Reverse Osmosis

CHAPTER ONE: INTRODUCTION

1.1 General

Reinforced concrete structures are extensively utilized in contemporary construction because of their durability, adaptability, and long service life. Among various structural components, beams play a crucial role in transferring loads and ensuring stability. While traditional beams are commonly used, many situations require structural elements with increased depth and enhanced load-bearing capacity. With ongoing infrastructure development and urban expansion, there is a growing demand for efficient and cost-effective structural solutions. Deep beams offer a promising solution by combining strength, flexibility, and diverse design options.

Reinforced concrete deep beams are among the most widely used structural elements in contemporary construction due to their diverse mechanical properties. Their ability to carry substantial loads with minimal flexural deformation makes them ideal for use in high-rise buildings, foundation walls, and water tanks where walls span between column supports and function as deep beams [1–3]. They are also commonly employed in offshore structures, supporting strip footings or raft slabs [4], pile caps [5], complex foundation systems [6], transfer girders, and in resisting horizontal loads on floor slabs [7,8], as illustrated in Fig. 1.1.

This renders them optimal for situations when strength is important and vertical space is permitted. Deep girders also provide architectural adaptability, allowing for imaginative designs that meet both functional and aesthetic requirements [7].

Deep beams may be categorized into numerous types, including simply supported or continuous beam based on support conditions, with or without openings

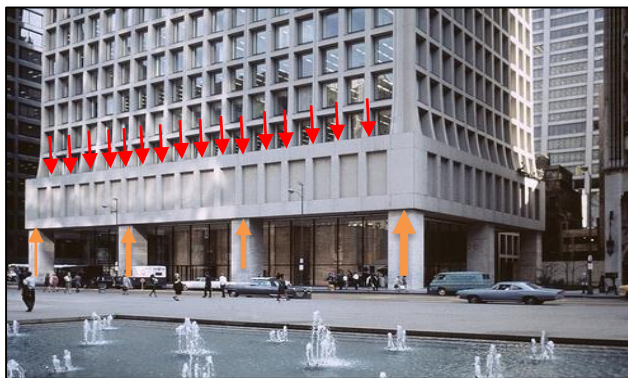
depending on the existence of openings, and rectangular, I, L, or T-sections according to the cross-sectional shape.



(a) Pier of bridges



(b) pile caps



(c) the Brunswick Building in Chicago.



(d) Marine applications

Figure 1.1 An example of deep beam [1-5].

In civil engineering, the relationship between materials and structural performance has long been a focus, especially when it comes to concrete structure optimization. Hybrid concrete systems, which combine several components to improve the mechanical properties of conventional concrete, have attracted interest recently. In the case of deep beams, where shear strength is an important consideration in determining the strength of the structure, this investigation is particularly relevant.

1.2 Deep Beam Definition

Reinforced concrete deep beams are structural elements with a greater depth than usual with regard to their length, but a section that is thinner perpendicular to the length or depth is smaller. According to ACI Code 318-19, reinforced concrete deep beams are defined as those whose point load is located two times the depth of the whole member from the supports' face, or whose clear span does not exceed four times the member's total depth [9], see Fig 1.2.

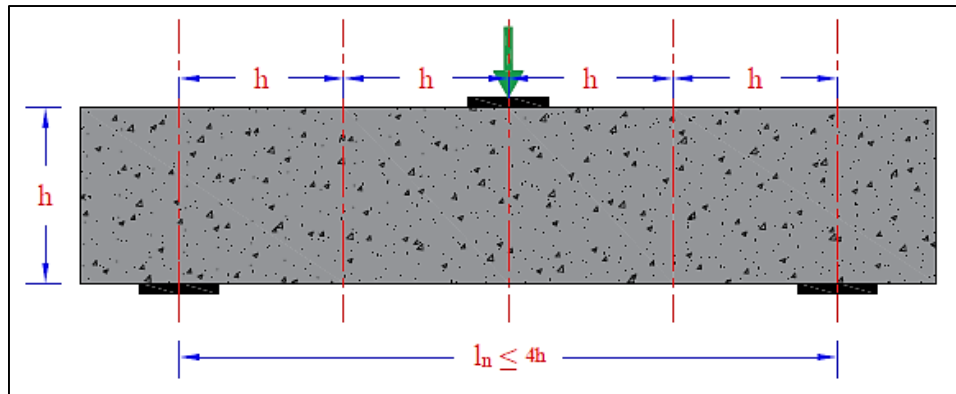


Figure 1.2 ACI limitations for Deep Beam [9].

Numerous factors influence the behavior of deep beams, including loading type, applied load location, percentage of tension reinforcement, amount and type of web reinforcement, clear span to effective depth ratio (l_n/d), shear span to effective depth ratio (a/d) see Fig 1.3, reinforcement, concrete's compressive strength, anchoring of reinforcement, and supporting area width. Because there are so many variables, creating an inclusive design approach is difficult [10-12].

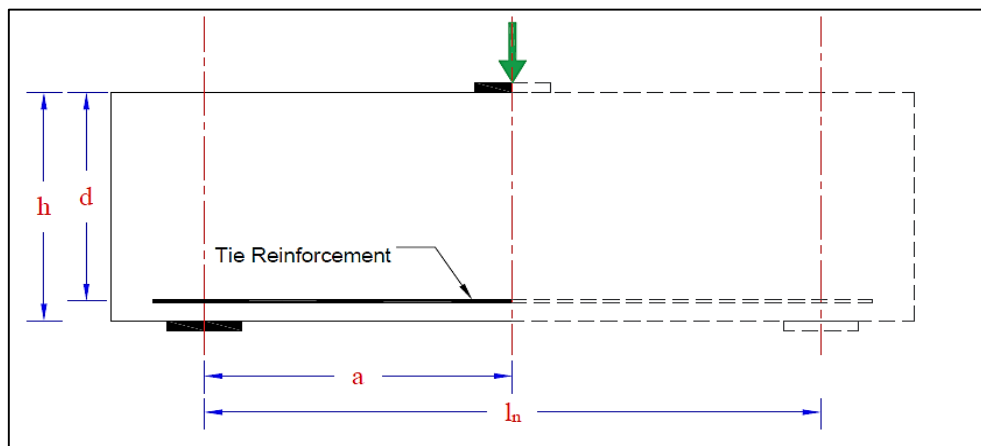


Figure 1.3 Effective depth ratio (a/d) of the deep beam.

1.3 Behavior of Deep Beam

A thorough understanding of the behavior of deep beams under load is essential for effective structural analysis and design. Unlike conventional beams, deep beams exhibit distinct load distribution patterns, shear transfer mechanisms, and moment resistance characteristics.

Enhancing the structural performance of deep beams requires a comprehensive understanding of the underlying principles of shear strength. Due to their relatively large span-to-effective depth ratio (a/d), deep beams exhibit more complex stress distributions compared to conventional beams, often resulting in significant shear stresses that challenge traditional design methodologies. The total shear capacity of these members is largely governed by the interaction of multiple shear transfer mechanisms, including strut-and-tie action, aggregate interlock, concrete compression strength, and shear friction. Recent studies have demonstrated that various improvement techniques can be enhanced shear strength. One promising enhancement technique involves the use of hybrid concrete, where incorporating different types of concrete can improve both bond behavior and the overall energy absorption capacity of deep beams. As engineers continue to investigate innovative materials and reinforcement strategies to boost structural performance, such findings open new pathways for future research. Consequently, advancing structural design methodologies requires a deep understanding of these mechanisms, validated by experimental evidence [15].

1.4 Failure Modes and Cracking Patterns

The failure modes of the deep beams varies depending on several factors, such as the type of loading, the ratio (a/d), the method of reinforcement, etc. Fig 1.4 shows the most common failure modes.

1.4.1 Diagonal-splitting failure

This occurs at the midpoint of the beam's depth when it is aligned with the strut. The fractures spread in both directions towards the loading plate and the bearing plate. This breakdown happens rapidly when the vertical steel reinforcement is not adequate.

1.4.2 Shear-Compression failure

This failure may be identified by deformation around the loading or bearing plate. It develops when the tensile strength exceeds the compressive strength (over-reinforcement).

1.4.3 Compression strut failure

This mechanism of failure occurs in concrete deep beams with low compressive strengths or in beams with significant vertical and horizontal shear reinforcement ratios.

1.4.4 Anchorage failure

This failure transpires at the extremities of the primary reinforcement at the beam's base when the development length or anchorage length of the tensile reinforcement is insufficient or absent of any mechanical anchoring.

1.4.5 Bearing failure

This mode often appears in beams subjected to loads near the support, exhibiting indications of bearing failure, as a local failure surrounding the steel bearing plate.

1.4.6 Flexural failure

This collapse transpires near the mid-span on the underside of the deep beam. This failure occurs when the (a/d) ratio is comparatively high.

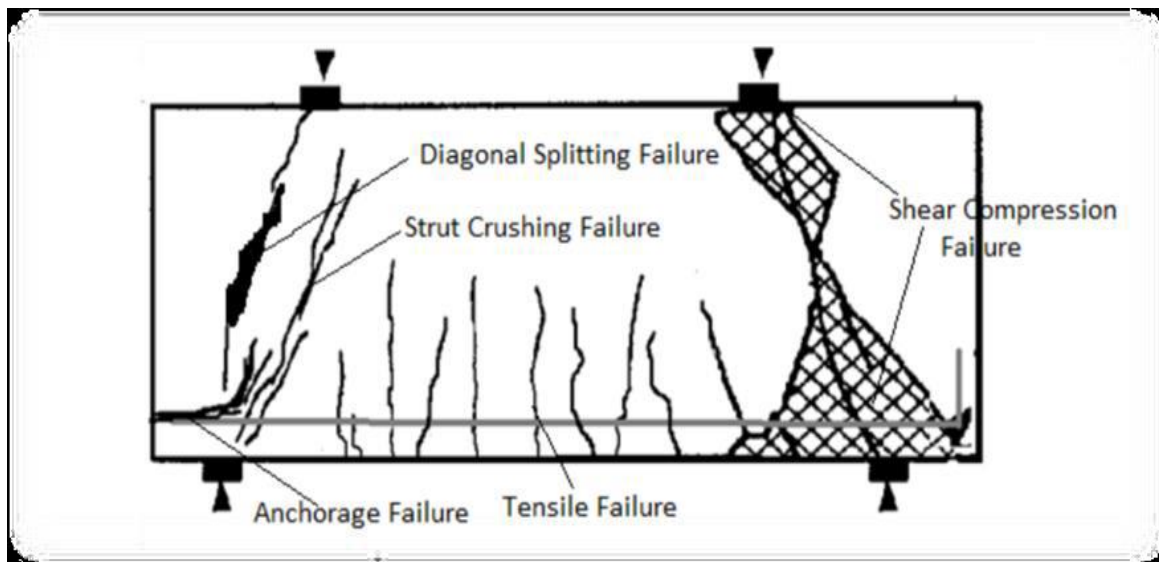


Figure 1.4 Common failure modes in deep beam[15].

1.5 Hybrid Concrete

Hybrid concrete refers to the deliberate combination of two or more types of concrete with varying properties such as strength, modulus of elasticity, or durability within a single structural element. This approach seeks to optimize performance by employing ordinary or recycled concrete in areas subjected to lower stress, while utilizing high-strength concrete in critical load-bearing zones. Several factors motivate the use of hybrid concrete specifically in deep beams:

- 1- Cost-effectiveness: Advanced materials such as steel fiber-reinforced concrete (SFRC) and high-strength concrete tend to be expensive. By limiting their application to critical regions, construction costs can be significantly reduced.
- 2- Improved Performance: In areas subjected to high stress such as near supports and load application points high-strength or fiber-reinforced concrete enhances shear capacity and improves resistance to cracking.
- 3- Sustainability: Utilizing recycled concrete aggregates or lower-grade concrete in low-stress regions reduces the environmental impact of construction.

- 4- Material Usage Optimization: Aligned with the principles of efficient structural design, hybrid concrete allows designers to tailor material distribution according to the stress requirements within the beam.

Recently, engineers have shown considerable interest in hybrid systems due to their cost-effectiveness and superior load-bearing capabilities [16]. In this study, a hybrid concrete system is implemented.

Functionally graded concrete (FGC) is considered one of the applications of hybrid concrete and can be regarded as an alternative technical term. This is because FGC typically involves two types of concrete with different strength levels, making it essentially a form of hybrid concrete designed to enhance performance by tailoring material properties according to stress distribution.

Since deep beams are entirely composed of disturbed regions (D-regions), significant stress concentrations are found at the strut zones, supports, and points of load application. To enhance performance in these critical areas, high-strength concrete (HSC) is used in the strut regions, while normal-strength concrete (NSC) is applied in the remaining parts of the beam. Given that the strut region primarily experiences compressive stress, the use of an arch was proposed, as the arch is a structural form inherently capable of withstanding high compressive loads, additionally, arch action plays a significant role in the behavior of concrete structural elements, especially in deep beams and structures subjected to heavy loads. Arch action refers to the ability of a structure to transfer loads through curved paths resembling an arch, where vertical forces are converted into horizontal compressive forces that flow toward supports or load-bearing points. This behavior reduces shear stresses in the mid-span region and helps enhance structural stability.

In deep beams, arch action enables a more efficient load distribution compared to conventional methods, allowing the structure to carry higher loads with less

material usage. Moreover, arch action improves the beam's resistance to both bending and shear simultaneously, making the understanding of this phenomenon essential for accurate and effective design and evaluation of deep concrete elements. Therefore, this study incorporates an arched geometry into the hybrid deep beam design, utilizing arching action principles to more effectively transmit forces to the supports. Employing lighter or lower-strength concrete in the lower stress regions can reduce cost without substantially impacting cracking resistance or load capacity [17].

By tracing the shape of the trajectory of stress in deep beams (see Fig.1.5), it is observed that one of the proposed stress trajectories follows curved paths rather than the straight lines seen in conventional beams. This curved, or arching, form of stress transfers often referred to as arched stress flow illustrates how compressive forces travel along nonlinear trajectories within the beam's depth, and it somewhat corresponds with the arch shape proposed in this study. These curved stress trajectories demonstrate how the load is transmitted from the point of application toward the supports through a combination of compression and tension paths.

The traction of stress represents the vector field of tensile forces along these curved lines, indicating how internal stresses align tangentially to these trajectories. This curved stress pattern is fundamental to understanding deep beam behavior, as it emphasizes that stresses are not uniformly distributed but instead concentrate along these arching paths. Proper recognition of this curved traction of stress enables more accurate modeling and efficient design, ensuring reinforcement is placed precisely where tensile forces develop along the curved stress trajectories.

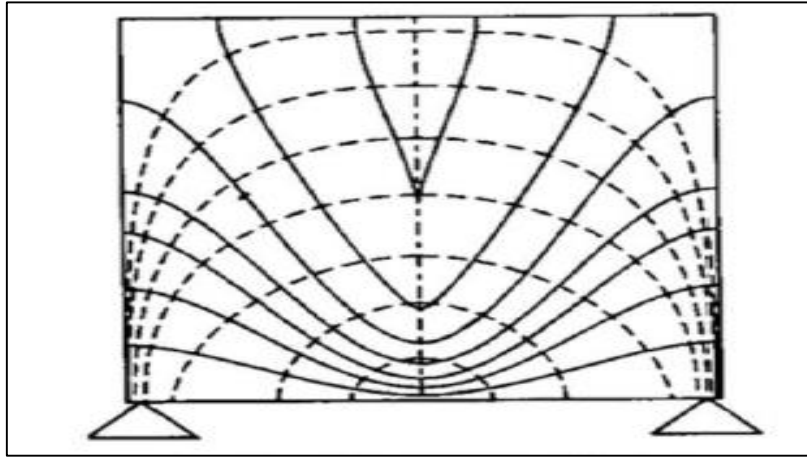


Figure 1.5 Trajectory of stress in deep beams.

1.6 High Strength Concrete (HSC)

High-strength concrete (HSC) has experienced notable growth over the past decade, largely due to advancements in field production techniques that utilize low water-cement ratios and high-quality water-reducing admixtures, in addition to its high compressive strength ($f'_c \geq 55$ MPa), which is important in engineering applications that require this strength. Despite its advantages, HSC tends to become more brittle as its compressive strength increases, often resulting in smoother shear failure surfaces [18].

High-strength concrete is commonly employed in the structural frames of large-scale buildings. In applications such as skyscrapers, high-rise buildings, and long-span bridges, the use of conventional concrete would necessitate excessively large columns and beams, resulting in impractical or inefficient designs. In contrast, high-strength concrete enables the creation of slender, more elegant structural elements, thereby maximizing usable interior space and enhancing architectural aesthetics. Additionally, structures built with high-strength concrete benefit from increased longevity, superior load-bearing capacity, and improved durability [19]. As a result of the above an important advantage of high-strength concrete is its potential for material efficiency. By enabling smaller cross-sectional areas, it allows for reductions in the total volume of concrete required. This is particularly significant in terms of sustainability, as cement production is

a major contributor to carbon dioxide emissions. Therefore, reducing cement content in high-strength concrete not only improves cost efficiency but also supports environmental objectives through decreased carbon footprints.

1.7 Aims of the study

The aims of this study are to:

1. Design and construct functionally graded concrete (FGC) deep beams with reduced cement content that fulfill the required structural limit states.
2. Evaluate the influence of various concrete strength, strut geometries, cement contents, and casting methods on the load-deflection behavior, strain distribution, and cracking patterns of deep beams.
3. Investigate the development and effectiveness of the strut-and-tie mechanism (STM) in both FGC and normal-strength concrete (NSC) deep beams.
4. Explore an alternative method of reinforcing the strut using L-shaped steel sections and assess its impact on both the strut's load-bearing capacity and the overall structural behavior of the deep beam, while examining the efficacy of this reinforcement technique in enhancing the structural performance and failure resistance of deep beams.

1.8 Thesis Organization

Five chapters make up this thesis, which describes a study on the behavior of deep beams with embedded functionally graded concrete struts. This may be simply described as follows:

- **Chapter 1:** provides an overview of deep beams, their uses, high-strength concrete, and functionally graded concrete.
- **Chapter 2:** It includes a review of previous studies and applications involving reinforced concrete deep beams with different concrete types and strut reinforcement configurations.

- **Chapter 3:** The experimental program is described, covering the manufacturing, detailing, instrumentation, and test setup of the specimens. This chapter also presents the measurable properties of the materials used in the experiments.
- **Chapter 4:** This chapter presents the experimental results and discussion, showcasing the data collected from each test through tables, graphs, and figures. The data includes stresses, crack formation, and load–deflection responses. Additionally, the chapter provides a comparative analysis of the specimens' performance.
- **Chapter 5:** It This section presents conclusions drawn from the obtained results and offers recommendations for further research.

CHAPTER TWO: LITERATURE REVIEW

2.1 Introduction

This chapter provides a brief review of the prior researches achieved to investigate the performance of deep beams. A variety of studies relevant to deep beams were examined and analyzed. Global research on deep beams has been documented, including the most important results. The literature related to the current investigation has been classified into three categories for clarity. The first category comprises the researches related to the behavior of reinforced concrete deep beams. The second were focused on researches talking about the use of high-strength concrete in the analysis and design of reinforced concrete deep beams. Finally, the third category included the previous studies that deals with the performance of hybrid deep beams. The concluding remarks and the research gap are also presented.

2.2 Factors Affecting RC Deep Beam Behavior

Deep beam behavior is studied, as is the effect of varying different variables on behavior, including section height, kind and ratio of reinforcement, shear span to depth ratio, etc.

Amornpinnyo and Teerawong in 2014 [20], examined the influence of the horizontal to vertical reinforcement ratios and the (a/h) ratio on the shear behavior of reinforced concrete deep beams. The range of test factor related to (a/h) ratios, were from 1.5 to 2, and the horizontal to vertical reinforcement ratios were (1, 3.11 and 0.32). The main findings of the study were showned that the ratio of horizontal to vertical reinforcements did not influence the final load capacity of deep beams with identical (a/h) ratios. Also, it was found that the transition from horizontal to vertical reinforcement in deep beams with (a/d) ratio of 1.5 alters the failure modes from shear compression failure to diagonal compression failure

The behavior of RC deep beam with dimensions $150 \times 350 \times 700$ mm under two point loads was investigated by Suresh and Kulkarni in 2016 [21]. The purpose of the research was to compare the numerical findings obtained from the finite element software ANSYS-14.5 with the actual behavior of reinforced concrete deep beams. Considering the varying percentage of tension reinforcement and the concrete compressive strength (f'_c), experimental and analytical results showed that increasing both the compressive strength (f'_c) and tensile reinforcement ratio resulted in higher values of both initial cracking load and ultimate loads. The compressive strength (f'_c) also contributed to improving the shear strength of the deep beams. The crack patterns were identical in the experimental and FEA results, demonstrating good agreement between the two methods in evaluating the structural behavior of deep beams, as shown in Fig 2.1.

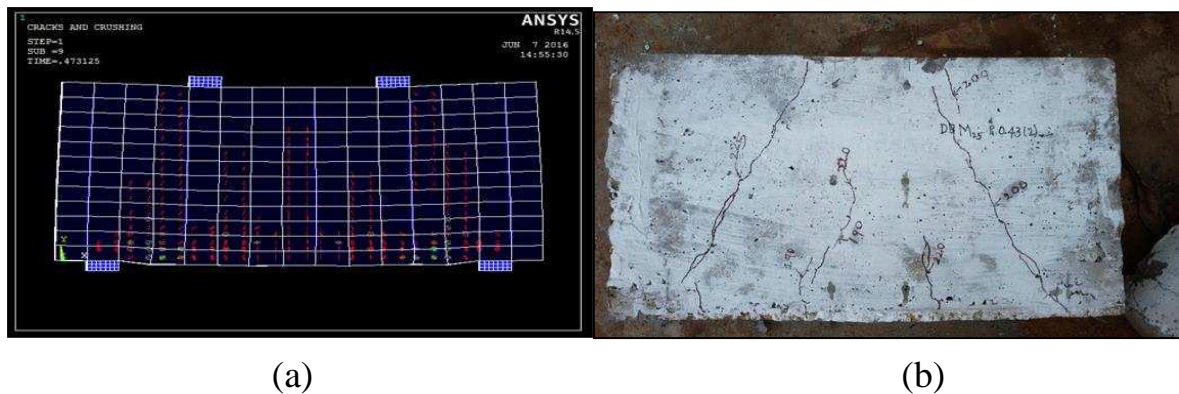


Figure 2.1 (a) The ANSYS-obtained crack patterns, and (b) cracks produced during the experiment [21].

Ismail in 2016 [22], conducted an experimental investigation on twenty-four simply supported RC deep beams that were tested under two-point concentrated loads. The specimens were divided into two groups. As shown in Fig 2.2a, all samples in the first group had identical dimensions of $100 \times 400 \times 1800$ mm and the same percentage of longitudinal reinforcement. In contrast, the samples in the second group shared a constant shear span-to-depth ratio of 1.67 and a longitudinal reinforcement ratio of 1.4%; however, as illustrated in Fig 2.2b, their geometries varied. The second group aimed to investigate the effect of size in the absence of web reinforcement. The primary objective of this

study was to examine how the behavior and shear strength of RC deep beams were influenced by various parameters, including shear span-to-depth ratio ($a/h=0.91, 1.29, \text{ and } 1.67$), member depth, concrete compressive strength, horizontal shear reinforcement ($0\text{-}0.215\%$), and stirrup reinforcement ($0\text{-}1.26\%$). The findings revealed that the shear capacity and behavior of RC deep beams were significantly governed by the shear span-to-depth ratio. Variations in the (a/h) ratio affected the development of arch action, which is the dominant shear transfer mechanism in deep beams. Since arch action is responsible for transferring loads directly to the supports, the ultimate shear capacity and overall structural performance were closely related to the concrete's compressive strength. Furthermore, the study found that incorporating a minimum amount of shear reinforcement improved the beams' shear strength by approximately 20%. However, increasing the amount of shear reinforcement beyond this minimum did not result in a proportional increase in shear capacity.

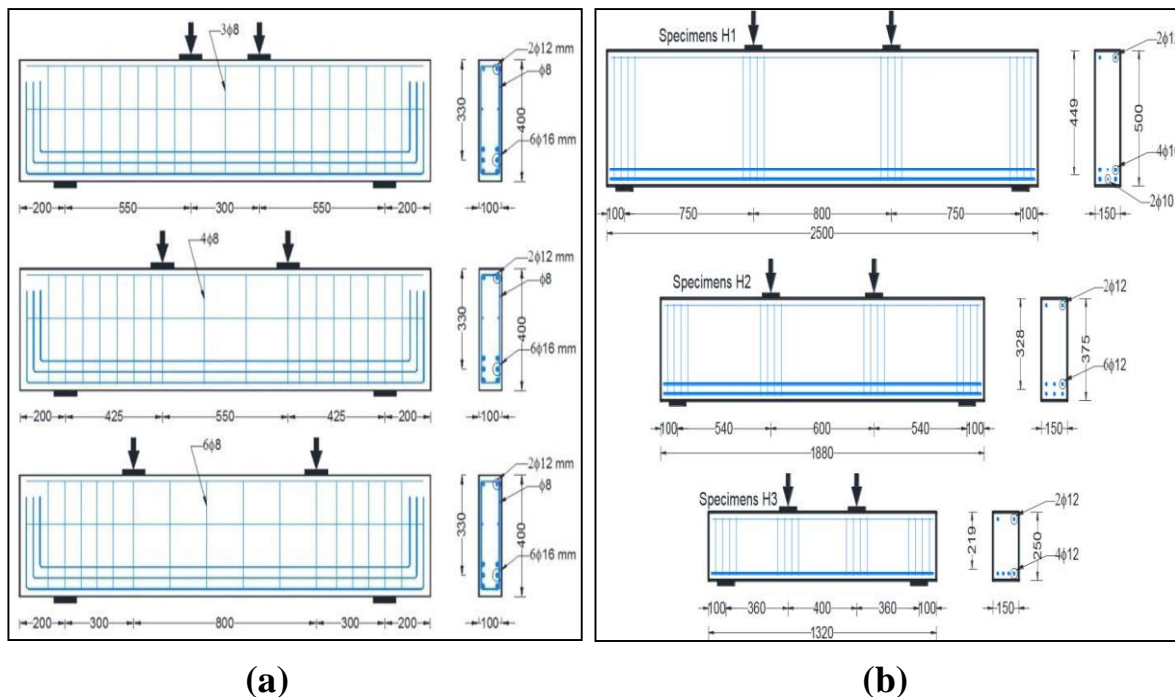


Figure 2.2 (a) Specifications of the first group's deep beams, and (b) Specifications of the second group's deep beams [22].

Demir et al, in 2019 [23], carried out an experimental investigation to explore the influence of section height (h), compressive strength (f_c'), and the shear span to effective depth ratio (a/d) on the behavior of eleven reinforced

concrete deep beams subjected to three-point loading. The compressive strength ranges from 18 to 32 MPa, the aspect ratio (a/d) was from 1.4 to 1.86, and the sectional height was between 400 and 600 mm. The findings indicated that the section height substantially influences the shear strength of reinforced concrete deep beams, accompanied by a slight rise in the maximum crack widths. An increase in the compressive strength of concrete results in enhanced ultimate load capacity and reduced maximum crack width, while an increase in the a/d ratio leads to diminished ultimate load capacity and enhanced maximum cracking width.

Jabir et al, in 2020 [24], examined the effects of varying factors such as (a/d) ratios (0.75, 1.25, and 1.75) on toughness, stiffness, ductility, and ultimate loads of RC deep beam. Experimental tests were conducted on three deep beam specimens under four-point loads as shown in Fig 2.3.

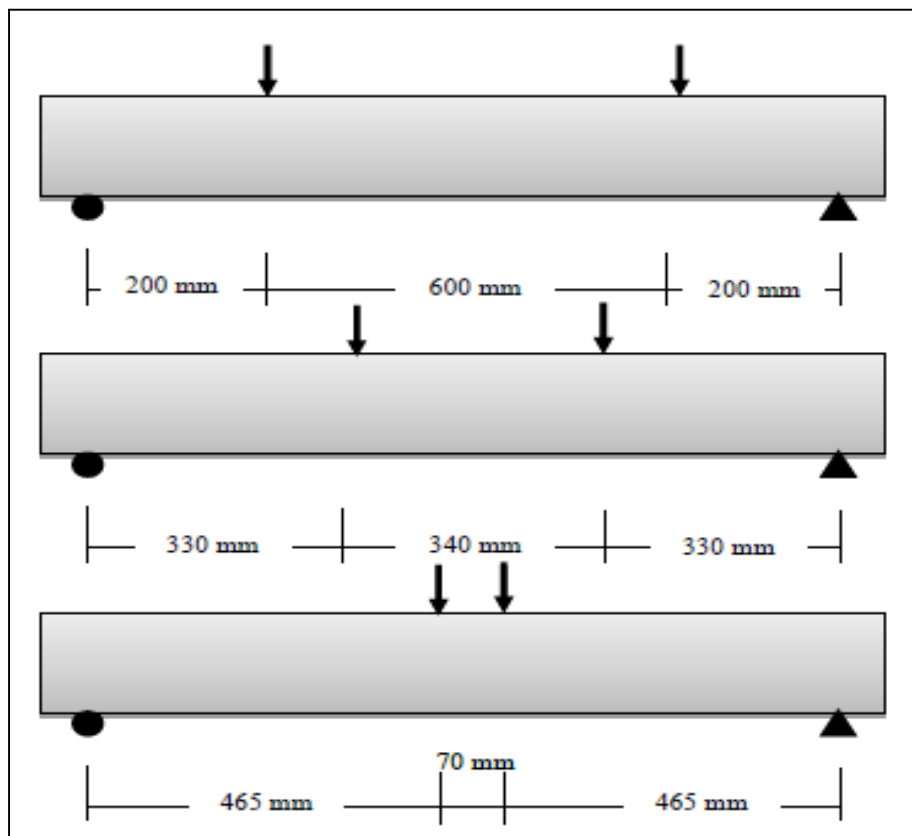


Figure 2.3. Different (a/d) ratio using in the study of [24].

The specimens were identical in size ($1250 \times 300 \times 150$ mm) and concrete grade (32 MPa). The findings indicated that:

- 1- The ductility of the tested specimens was little impacted by the shear span-to-depth ratio.
- 2- When (a/d) rose from $(0.75 - 1.75)$, the ultimate load capacity dropped by around 22%.
- 3- Stiffness and flexural toughness increased by around 122% and 18%, respectively, when a/d ratios were reduced from 1.75 to 0.75.

Zhang et al, in 2020 [25], carried out an experimental testing on eight deep beam specimens with various linear reinforcement ratios, vertical stirrup ratios, and shear span-to-depth ratios (0.3, 0.6, and 0.9) as shown in Fig 2.4. Each specimen has a compressive strength of 42.9 MPa. It was concluded that although the influence of vertical web reinforcement ratios on shear capacities was negligible, the shear capacities of deep beams rise when longitudinal reinforcement ratios increase and shear span-depth ratios lowers.

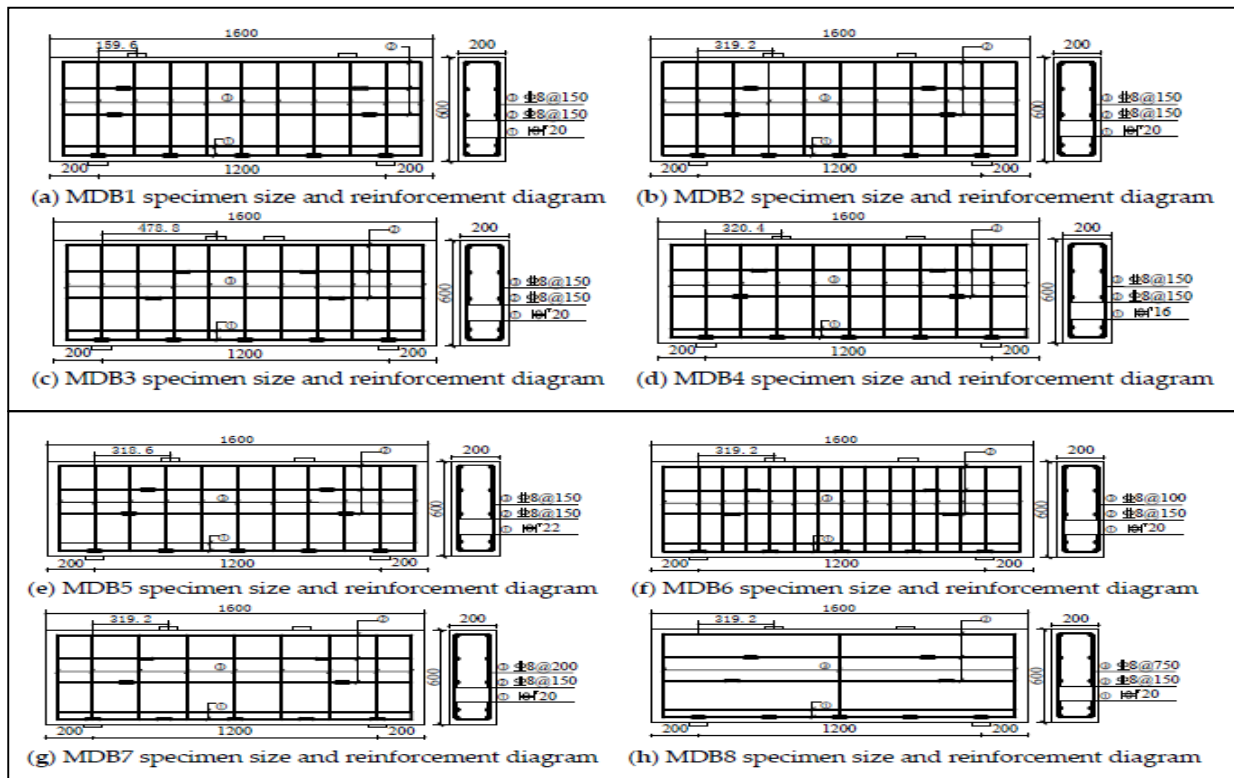


Figure 2.4 Reinforcement Details for the using samples in this study [25].

Chen et al, in 2022 [26] conducted a comprehensive study on the shear strength of reinforced concrete (RC) deep beams. The experimental findings were

based on a total of 110 specimens, including 81 simply supported and 29 continuous deep beams. The results demonstrated that diagonal tension cracking strength is significantly influenced by key design parameters, such as the shear span-to-effective depth ratio (a/d) and the main tensile reinforcement ratio, as illustrated in Fig 2.5. The study revealed that diagonal cracks tend to develop rapidly when service loads are applied. Notably, 35% of the tested deep beams failed under loads lower than the designated service load.

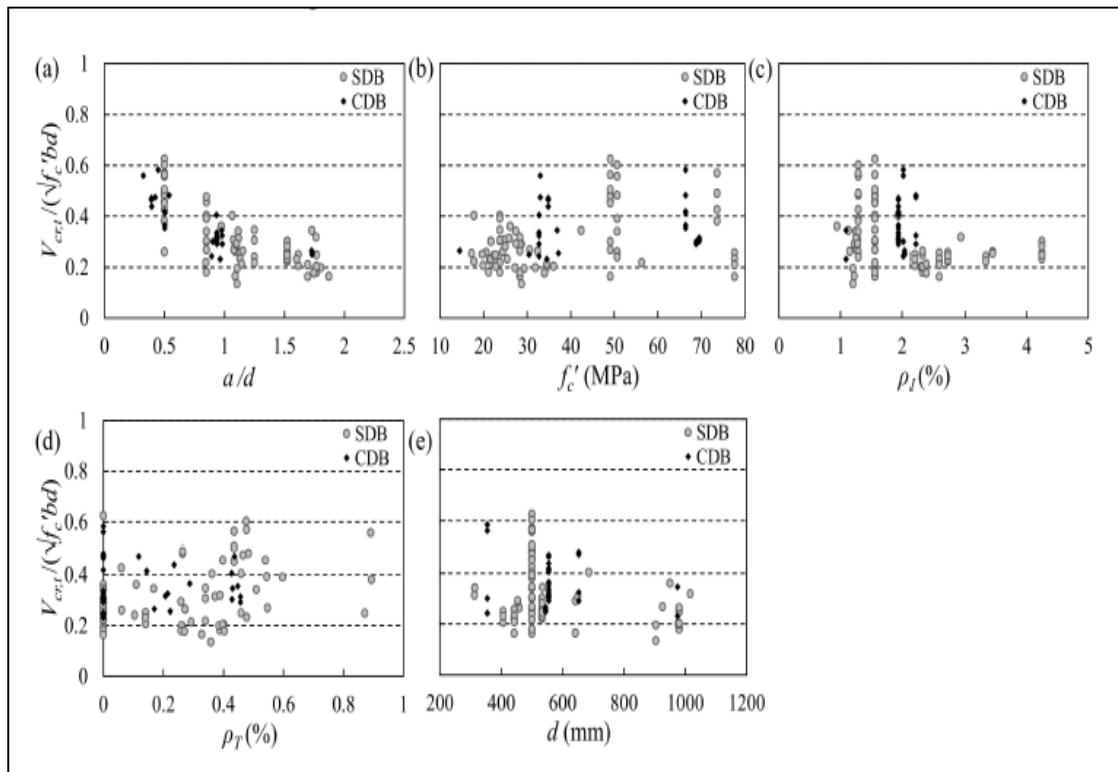


Figure 2.5 Relationship between design factors and dimensionless diagonal tension cracking strength $V_{cr,t}/(\sqrt{f'_c}bd)$ [26].

Abd El-Hakeem et al, in 2021 [27], examined the behavior of seven RC deep beam specimens with identical dimensions ($1170 \times 800 \times 120$) mm and 0.4 of employing a/d by experimental exploration. The variables were the percentages of web reinforcement 0, 0.25%, and 0.40% and the use of glass fiber-reinforced polymer (GFRP) for shear reinforcement rather than steel. The findings of the study show that when comparing the deep beams with steel and GFRP web reinforcement to the deep beams without web reinforcement, the ultimate load capacity increased by approximately 20–25% and 3–14%, respectively.

Furthermore, it found that when applying reinforcement ratios of 0.25% and 0.4%, the initial stiffness improved by 70 to 128% for deep beams reinforced by steel and by 6 to 60% for deep beams reinforced by GFRP, see Fig. 2.6. Finally, it found that the kind of web reinforcement had an impact on shear cracks but no effect on the quantity of bending fractures.

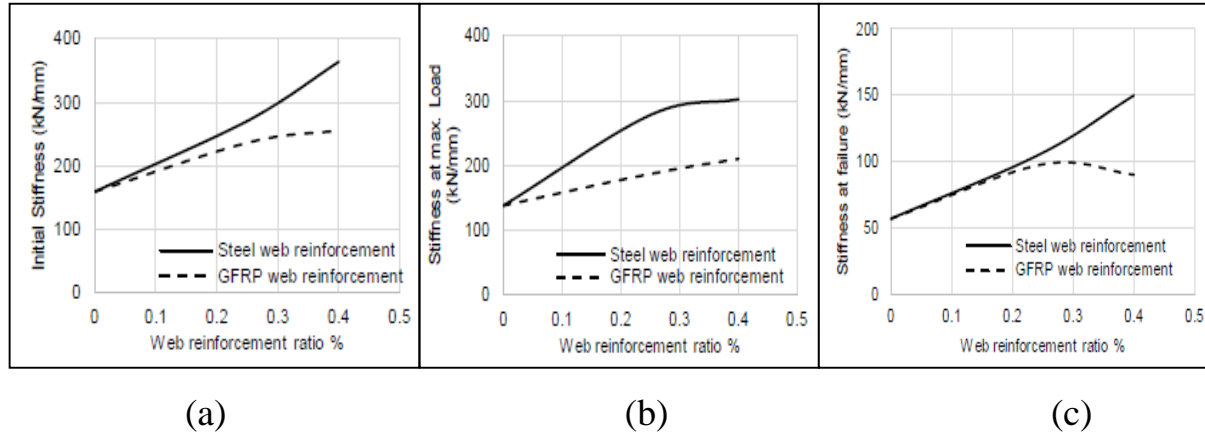


Figure 2.6 (a)The relationship between the web reinforcement ratio and initial stiffness. (b)Web Reinforcement Ratio and Stiffness at Maximum Load Relationship. (c)The relationship between the web reinforcement ratio and stiffness at failure [27].

Ammash and Al-Mousawi in 2021 [28], executed an experimental investigation to determine the optimal design by examining how the development of reinforcing struts affected the performance of discontinuity zones in four concrete deep beams. Fig 2.7 illustrates the testing of two distinct reinforcement designs and web reinforcements. The results proved the following:

- 1- All deep beams in compliance with ACI-318-14 failed with an ultimate load greater than the theoretical design, according to testing results. Crushing of the strut replaced diagonal splitting failure as the failure mode.
- 2- Increasing web reinforcement enhanced specimen's shear capacity. The beam's capacity increased by 17.7% and its deflection decreased when the struts were reinforced and the degree of shear reinforcement was decreased

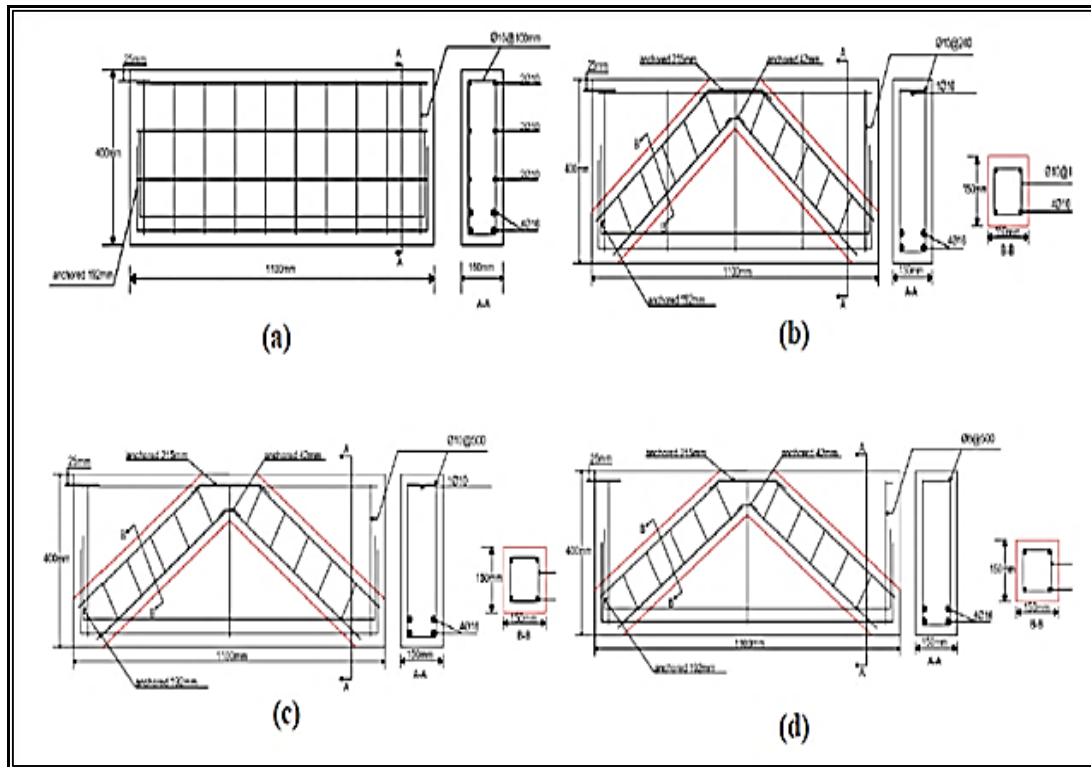


Figure 2.7 Reinforcement Details and dimensions for the using deep beams in study of reference[28].

The influence of uniformly distribution load applying on high strength RC deep beam behavior was investigated by SI et al, in 2022 [29]. The dimensions and loading conditions are presented in Fig 2.8. some of factors were taken into account, such as the vertical stirrup ratio (0.25, 0.33, and 0.5%) and the longitudinal reinforcement ratio (0.67, 1.05, and 1.27%).

Three failure types were identified for deep beams subjected to uniform loads: local compression failure, diagonal-compression failure, and splitting failure, as shown in Fig 2.9. Beside that, numerous findings were also published. These were:

- 1- The cracking load was not significantly impacted by the longitudinal and stirrup reinforcement ratios. The final load was significantly impacted.
- 2- By raising the stirrup reinforcement ratio, the crack width may be reduced

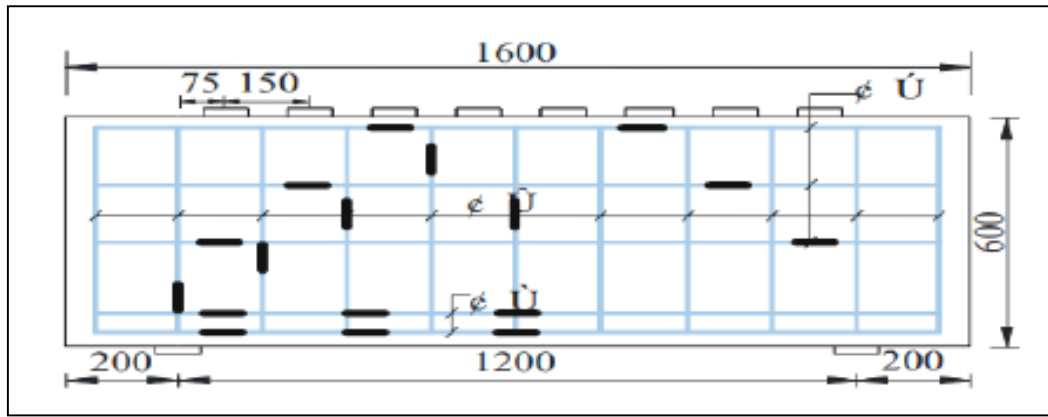


Figure 2.8. Specimen dimensions and the distribution of load technique [29]

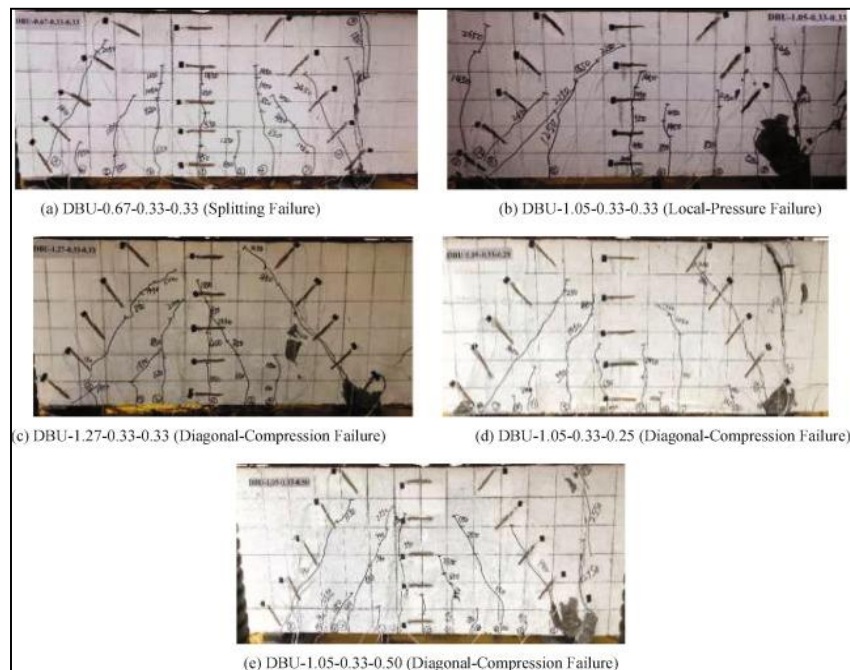


Figure 2.9. Failure modes for the deep beams [29]

2.3 Behavior of (HSC) and (UHPC) Deep Beams

Tan et al, in 1997 [30], showed results from an experimental study on the behavior and ultimate shear strength of eighteen high-strength concrete deep beams. The compressive strength of the concrete cylinder varied between 55 and 86 MPa. The evaluated specimens were categorized into three series according to the shear span-to-depth ratio. Each set had six beams including various configurations of horizontal and vertical web reinforcements. Measurements were conducted on mid-span deflections, crack widths, failure modes, and ultimate strengths. Test findings indicated that the members with a shear span-to-

depth ratio greater than 1, vertical web reinforcement was more efficacious than horizontal web reinforcement. Orthogonal web reinforcement, consisting of both vertical and horizontal elements, effectively enhances beam stiffness, limits the development of diagonal crack width, and improves ultimate shear strength. The deep-beam specifications in the ACI Code exaggerate the role of the horizontal web steel in shear strength.

Foster and Gilbert, in 1998 [31], tested sixteen HSC deep beams up to failure. The variables examined in the study were the shear span-to-effective depth ratio, concrete strength, and the inclusion of secondary reinforcement. The investigation's findings indicated that accurate load forecasts may be achieved using the plastic truss model in conjunction with the efficiency factor proposed by Warwick and Foster. The plastic truss model simulates the internal force transfer within the beam by idealizing it as a system of struts and ties that behave plastically, capturing the nonlinear behavior after cracking. The efficiency factor proposed by Warwick and Foster adjusts the predicted strength by accounting for the actual performance of the concrete struts and ties, considering factors such as cracking, confinement, and material degradation, to provide more realistic estimates of load-carrying capacity.

Oh and Shin, in 2001 [32], presented an experimental study on fifty-three symmetrically loaded reinforced concrete deep beams with compressive strengths between 23 and 74 MPa were tested to evaluate their ultimate shear and diagonal cracking capacity. The range of the shear span-to-depth ratio was 3-5. The longitudinal reinforcement amount of specimens were varied between 0.0129 to 0.0156. On the other hand, the horizontal and vertical shear reinforcement ratios were 0-0.94% and 0-0.34%, respectively. Regardless of concrete strength, the shear span-to-depth ratio determines the final shear failure mechanism of deep beams. The rapid and unexpected failure of deep beams with HSC occurs at a lower shear span-to-depth ratio. The ultimate shear strength was significantly influenced by the strength of the concrete. According to test findings, the shear

span-to-depth ratio was used to calculate the ultimate shear strength of deep beams.

Yang et al, in 2003 [33], introduced a practical study involving twenty-one reinforced concrete beams was conducted to investigate their shear behavior. The concrete compressive strength of the specimens ranged from 31.4 to 78.5 MPa, the overall depth varied from 400 to 1000 mm, and the shear span-to-depth ratio ranged between 0.5 and 1.0. The study found that a reduction in the shear span-to-depth ratio, combined with an increase in member depth at the same ratio, resulted in more brittle failure modes characterized by wide diagonal cracking. The influence of size effects was found to be more significant in high-strength concrete (HSC) deep beams, particularly in terms of brittle behavior. Specimens with a shear span-to-depth ratio of 0.5 exhibited less pronounced size effects compared to those with a ratio of 1.0. Additionally, the study highlighted that due to these size effects, the ACI 318M-99 code does not provide a sufficiently conservative safety factor for the ultimate shear strength of HSC deep beams. However, it does offer comparable safety margins for shear strength at the onset of diagonal cracking.

Shengbing and Lihua, in 2012 [34] conducted an experimental study on eighteen simply supported hybrid fiber-reinforced high-performance concrete (HFRHPC) deep beams. All specimens had identical dimensions ($150 \times 500 \times 1040$ mm), a longitudinal reinforcement ratio of 1.356%, a span-to-depth ratio of 1.6, and a shear span-to-depth ratio (a/h) of 1. The beams were tested under a two-point concentrated load to examine their shear capacity and diagonal cracking behavior.

The primary objective of the study was to evaluate the effects of various parameters on the shear and diagonal cracking strengths of HFRHPC deep beams. These parameters included the volume fractions of steel and polypropylene fibers, the shape and aspect ratio of the steel fibers, and the inclusion of vertical and horizontal web reinforcement.

The results demonstrated that the incorporation of hybrid fibers significantly enhanced both the shear and diagonal cracking strengths of the beams. Specifically, a combination of 0.165% steel fibers and 1.0% polypropylene fibers led to an 83.3% increase in diagonal cracking strength. It was also found that increasing the volume of polypropylene fibers had a more pronounced effect on improving diagonal cracking strength, whereas steel fibers contributed more to enhancing overall shear strength. When 1.0% steel fiber and 0.165% polypropylene fiber were combined with web reinforcement, the shear strength improved by approximately 35.2%.

Omar and Msheer, in 2013 [35] investigated the structural behavior of ultra-high-performance fiber-reinforced concrete (UHPFRC) deep beams. A total of fifteen simply supported beams were tested under two-point loading. The study examined the influence of concrete compressive strength, shear span-to-depth ratio (a/d), and total beam depth (180, 240, and 300 mm), with all beams having a constant width of 120 mm. The experimental results indicated that increasing the concrete compressive strength from 42 MPa to 63.75 MPa and then to 134.5 MPa led to significant improvements in performance. Specifically, diagonal cracking loads increased by 31% and 150%, respectively, while the ultimate failure loads increased by approximately 44% and 150%. Additionally, the failure load was found to be highly sensitive to variations in the shear span-to-depth ratio (a/d), further emphasizing its critical role in deep beam behavior.

Seven simply supported reactive powder concrete deep beams were evaluated under two-point focused loads by Hani et al. in 2013 [36]. Each test sample measured 110 x 300 x 1400 mm and had the same amount of longitudinal reinforcement (2.44%). According to the experimental findings of this study on the behavior of reactive powder concrete deep beams, the mode of failure was identified and the (a/h) had a significant impact on the behavior of the structural element. As the (a/d) decreased, the shear strength and cracking load rose. As

the deflection reduced, the model became more rigid as the (a/d) dropped. Shear strength and cracking load both rise with increasing silica fume levels.

Bashandy et. al, in 2014 [37], used steel fiber and two forms of reinforcing to examine how the cement content affected the load deflection relationship of the deep beams made from reactive powder concrete. The results of the experiment showed that the cement and steel fiber contents of these kinds of beams had a substantial impact on the ultimate load and the cracking load. The behavior of these beams was more affected by the shear reinforcement when steel fiber was not used. For these kinds of beams, it was also discovered that using a non-linear finite element computer software worked well.

Shuraim and El-Sayed in 2016 [38], conducted a research study on the suitability of Strut and Tie model (STM) for determining the shear strength of 18 deep beams, of HSC. The depth of the beam, span to effective depth ratio (a/d), and the longitudinal reinforcement were in different ratios, as shown in Fig 2.10, were the factors under investigation. The findings indicated that the shear strength was reduced by reducing the longitudinal reinforcement ratio and increasing the shear span-to-depth ratio. Furthermore, it was stated that effective estimations were obtained while designing the HSC deep beam specimens utilising STM calculations.

Yaseen in 2016 [39], examined the behavior and shear strength of sixteen deep beams made of reinforced concrete under a two-point load. The factors taken into consideration were the concrete's compressive strength (40–120) MPa and the shear span to depth ratio (1, 1.5, and 2). The findings demonstrated that although beam's ultimate shear capacity improved with increasing compressive strength, it declined with increasing shear span to depth ratio. By raising the concrete's compressive strength from NSC to HSC and subsequently from HSC to UHPC, the central deflection of beams reduced when flexural cracks developed. As concrete's compressive strength increased from 43 MPa to 61 MPa and later to

119 MPa, the diagonal cracking load increased by 69% and 8%, respectively, while the failure load increased by 55% and 72%, respectively.

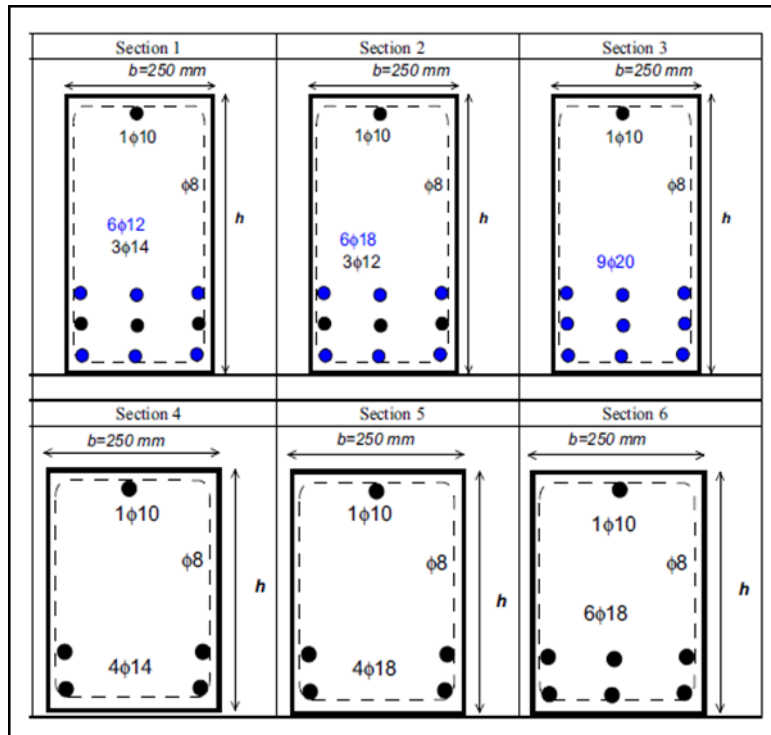


Figure 2.10. Specimen cross sections and its details [38].

Kaize et al, in 2018 [40], conducted an experimental study on the behavior of hybrid deep beams, including two kinds of steel fibers at varying ratios of 0%, 1%, and 2%, with the compressive strength of the models ranging from 66 to 72 MPa. The variable examined was the impact of steel fiber of both kinds. The ultimate load increased by 67% and 114% with the addition of 1% and 2% fibers, respectively, in comparison to the standard deep beam.

Chen et al., in 2022 [41], evaluated sixteen samples of deep beams measuring $(1200 \times 600 \times 150)$ mm. The volume of steel fibers (V_f) of 0, 0.5, 1, 2, and 3, the type of concrete (NSC, HSC, and Ultra-High Performance Concrete (UHPC)), and the shear span to depth ratio were among the factors that were examined. The specimens' shear capacity was increased as the concrete's compression strength increased. In UHPC deep beams, increasing the steel fiber volume fraction resulted in a considerable increase in the compression and tension strengths. When (a/d) climbed from 0.554 to 0.739, the UHPC deep

beam's capacity remained almost constant; however, when (a/d) increased to 0.923, the capacity dropped by 16.9%.

1.9 Deep Beams Incorporating Steel Sections

As shown in the linked papers, some research has examined the impact of employing steel sections as reinforcement in addition to the traditional reinforcing bar or as a substitute for fully reinforcing the struts in deep beams.

Abdul-Razzaq et al, in 2017 [42], investigated the possibility of using steel plates as shown in Fig 2.11, to reinforce the opening present in the web of RC deep beams.

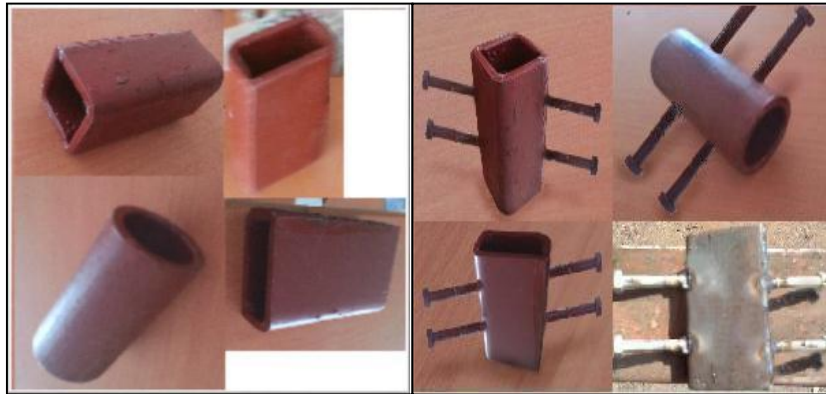


Figure 2.11 The holes are strengthened with steel palates and studs [42].

Thirteen deep beams with square, circular, horizontal, and vertical rectangular holes were tested under two point loads. Each tested beam was 1000 mm in length and had a cross section of 100 mm and 400 mm. Two holes were symmetrically positioned around the midway of the inclined compressive strut, one in each shear span. The opening form, the use of reinforcing steel plates, and the use of strengthening stud connections were among the test criteria. It was determined that the degree of interruption of the inclined compressive strut was the primary determinant of the structural behavior of deep beams with apertures. When compared to the reference solid beam, the final capacity decreased by about 20.5%, 18.3%, 24.7%, and 31.7%, respectively, when square, circular, horizontal, and vertical rectangular apertures were constructed. However, it was discovered that using steel plates to reinforce those gaps greatly improved the RC deep

beam's shear strength. When compared to the unstrengthened apertures, the strong increase in beams with reinforced square, circular, horizontal, and vertical rectangular holes was around 9.3%, 13.2%, 8.8%, and 11.88%, respectively. Additionally, in compared to the unstrengthened apertures, the strengthening increase in square, circular, horizontal, and vertical rectangular holes was about 16.9%, 17.8%, 14.3%, and 26.9%, respectively, when studs were added to the strengthening plates. Furthermore, a numerical parametric investigation was carried out using the finite element method using ANSYS 11 software. It was discovered good agreement between the experimental and numerical results.

Jasim et al, in 2020 [43] investigated the effectiveness of using closed steel plates as a replacement for traditional shear reinforcement in deep beams. The experimental program included three basic deep beam specimens, as illustrated in Fig. 2.12. All beams were cast using concrete with a compressive strength of 32 MPa. The reference specimen exhibited shear failure, which was identified as the primary failure mode across all beams. The inclusion of steel plates significantly influenced the structural performance. Compared to the reference beam, the cracking load and the ultimate load increased by approximately 16–60% and 15–19%, respectively. This improvement was attributed to the combined effects of diagonal splitting resistance and enhanced shear-compression reinforcement provided by the steel plates. Furthermore, the presence of steel plates contributed to controlling crack initiation and propagation, thereby improving the overall shear behavior of the deep beams.

Chiriki and Harsha in 2020 [44] investigated shear failure mechanisms in reinforced concrete (RC) deep beams, emphasizing their critical importance in structural design. While numerous studies have previously addressed this failure mode, only a few have yielded successful mitigation strategies. This study specifically focused on the influence of shear reinforcement alignment on the development and behavior of critical shear cracks. Four deep beam specimens

were analyzed, each with varying configurations of vertical and horizontal shear reinforcement. Two beams employed traditional reinforcement layouts, while the Third one incorporated shear reinforcement arranged in a truss-like configuration an approach aligned with the strut-and-tie model known for its effectiveness in deep beam applications. The fourth specimen included a Rolled I-section to explore the composite behavior of RC deep beams, as illustrated in Fig 2.13. The study utilized ABAQUS finite element software to evaluate several parameters, including shear reinforcement percentage, load–deflection behavior, and shear stress distribution. The findings highlighted the importance of reinforcement configuration in enhancing shear performance and delaying failure in deep beams.

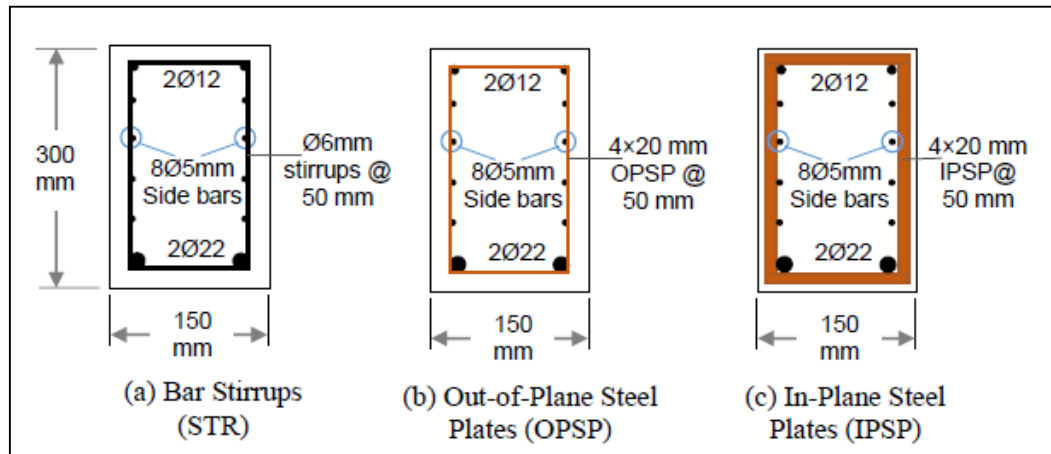


Figure 2.12. Cross sectional details of the tested beams [43].

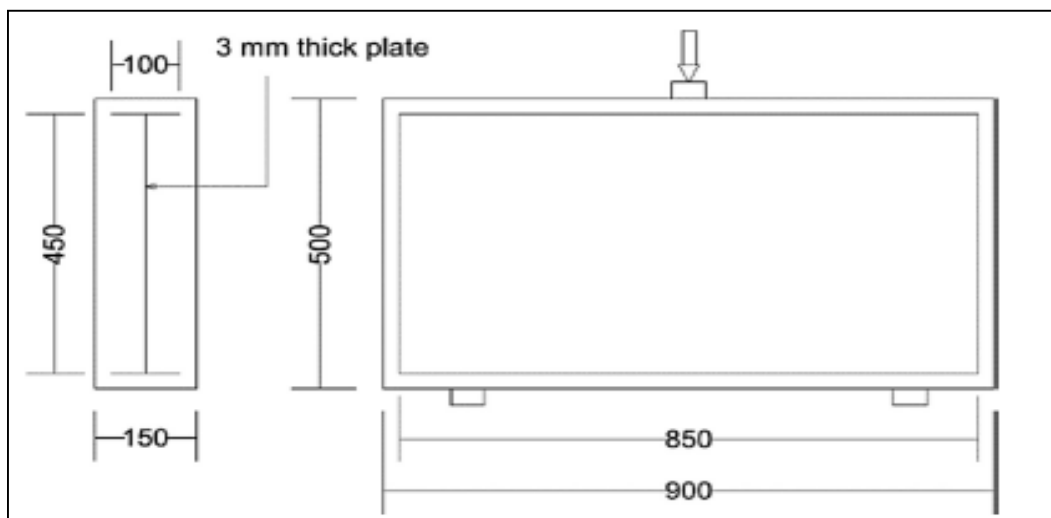


Figure 2.13 Cross section and the embedded I-section steel plate [44]

Abadel and Albidahthey (2021) [45], conduct an experimental investigation to examine the impact of several shear reinforcing systems on shear performance of deep beam. Different shear reinforcement schemes were used to cast seven deep beams. Three reference deep beam samples were cast using (1) plain concrete, (2) plain concrete with stirrups, and (3) concrete with steel fiber without stirrups. Also, two other reinforcement configurations using steel bar and steel section reinforcement were used as shown in Fig 2.14. For the steel section, inverted U-shaped steel angles measuring 50 mm by 50 mm by 4 mm, while for steel bar, inverted U-shaped steel rebars measuring 2 of 16 mm. Both plain concrete and steel fiber reinforced concrete deep beam samples were examined for each shear reinforcing method. In comparison to the reference beam without shear reinforcement, the findings demonstrated that the suggested schemes (an inverted U-shaped structure composed of angles and steel bars) enhanced the shear capacity of deep beams by 40.9–75.2%.

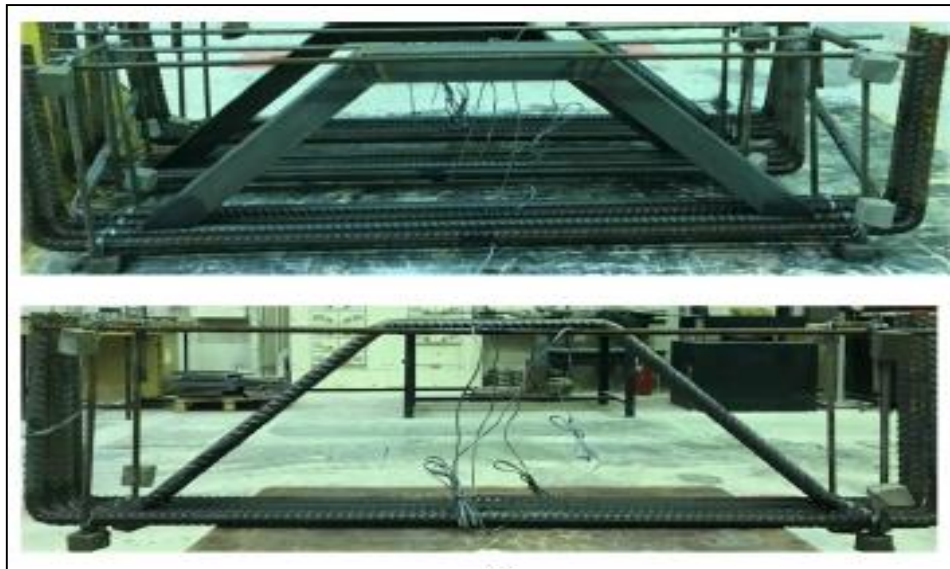


Figure 2.14 Type of the strut's reinforcement [45].

The suggested methods demonstrated equal ultimate shear resistance to the reference deep beam constructed with closely spaced stirrups, in addition to enhancing the post-peak behavior and ductility. When combined with steel bars and inverted U-shaped angles, steel fiber reinforced concrete increased the deep beams' ultimate shear resistance and created a longer period of stable inelastic

behavior than the reference beam with stirrups. To forecast the shear strength of the deep beams, a strut-and-tie model was employed.

The study conducted by Chai et al. in (2023) [46], to examine a unique shear reinforcement technique that employs thin mild steel (TMS) plates as a substitute for traditional reinforcement in deep beams as shown in Fig 2.15. Thirteen reinforced concrete deep beam specimens, with three distinct plate thicknesses and four different perforated hole configurations on the TMS plates, were subjected to experimental testing to assess their load-carrying ability and fracture patterns. The testing findings demonstrate that the 2 mm thick of TMS plate has the greatest load-bearing capability. Of the four distinct hole configurations on the TMS plates, the perforated plates with a three-column hole design exhibit superior performance regarding load-carrying capacity, demonstrating a 2.9% increase compared to the control beam specimen. The specimens exhibited elastic stiffness comparable to the control beam using conventional shear connections. This indicates that TMS plates may substitute traditional shear connections in deep beams. This suggested strategy altered the failure mechanism from traditional diagonal shear tension failure to a hybrid of flexural and shear deformation. A numerical model was created and shown a strong connection with the experimental data, indicating its potential for future parametric studies on deep beams and cost savings in further experimental efforts.

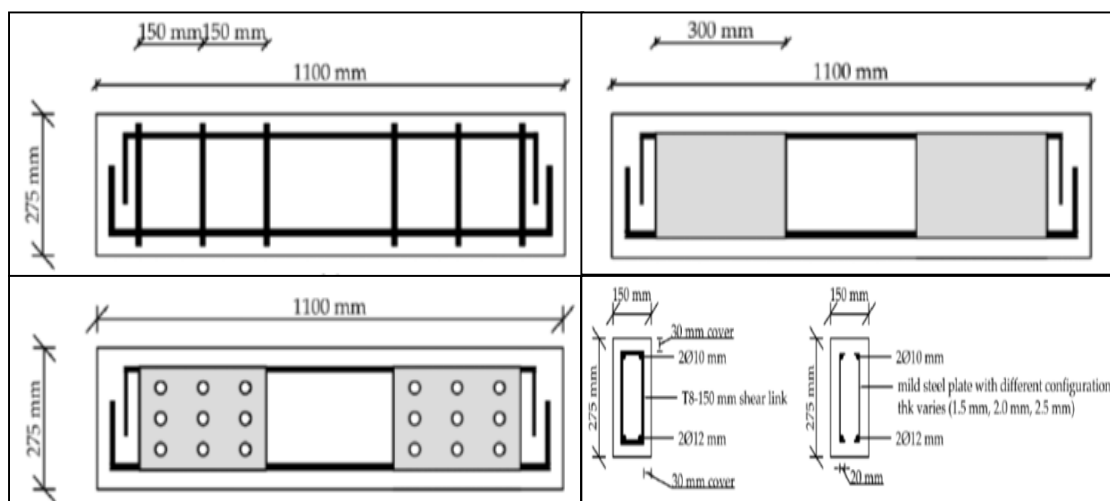


Figure 2.15 Specimen reinforcement details using steel plates [46].

2.5 Hybrid Concrete Deep Beams:

Hassan in 2015 [47], tested twelve specimens of simply supported deep beams. These beams included three with regular concrete, three with Ultra-high performance concrete, and six with hybrid models of normal and Ultra-high performance composite concrete in the compression zone, as seen in Fig 2.16. Different quantities of steel fiber ratios (0, 0.5 and 1) % in both regular and Ultra-high performance concrete were used. The effect of these parameters on the behavior of the test beams included deflection, failure mode, and ultimate loads is investigated. Experimental results generally show that stiffer load-deflection behavior is obtained with the increase of UHPC layer thickness (h_R/h) and steel fibers volumetric ratio (V_f) for hybrid beams with UHPC in compression.

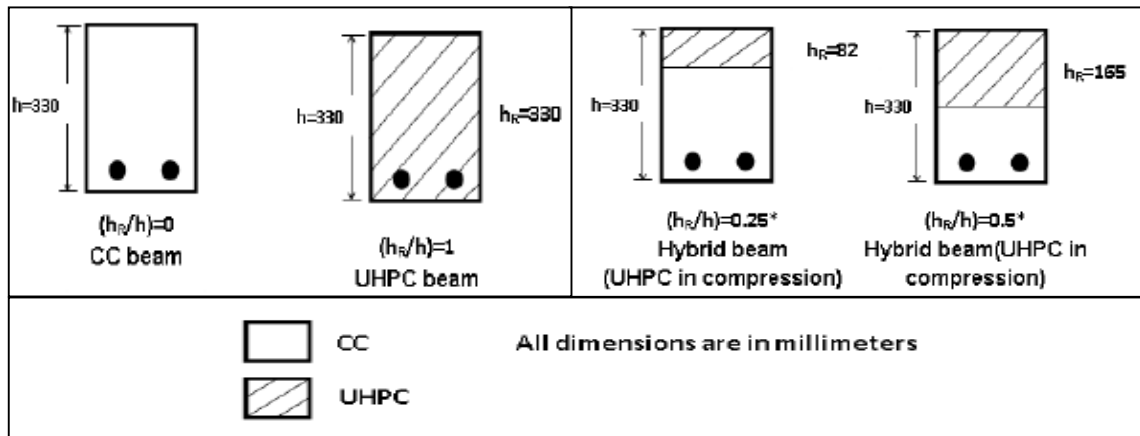


Figure 2.16 Types of the tested deep beams[47].

Experimental tests were conducted by Ammar and Maha, in 2015 [48], on nine simply supported deep beams under the influence of intense two-point load. The measurements of each deep beam were $(100 \times 450 \times 1400)$ mm. Fig.2.17 displays information on the loading and the hybrid section. Examining the overall shear behavior of hybrid RC deep beams composed of two distinct concrete strengths normal strength concrete (NSC) and high strength concrete (HSC) was the goal of the study. The manner of casting concrete layers (at the same time or at various periods), the thickness of the high strength concrete layer, and the impact of web reinforcement were among the test factors. The ultimate shear strength of beams made of HSC (approximately 45MPa) with a layer in the

compression zone of thickness (25–50%) of the total beam depth increased by approximately 11.2% to 19.5% for beams without web reinforcement and 16.75% to 22.25% for beams with minimum web reinforcement, according to experimental test results derived from the adopted hybridization technique of HSC and NSC. Additionally, it has been shown that the first cracking load was raised by around 32.8% to 48.8% and 43.4% to 57.9% for beams without and with web reinforcement, respectively. For specimens without and with web reinforcement, the ductility of hybrid concrete beams that cast monolithically has increased by around 13.3% to 22.6% and 17.3% to 26.3%, respectively. For specimens without and with web reinforcement, the hybrid concrete beams with construction joints and an epoxy resin coating that is around 1 mm thick have shown a greater increase in ductility of 28.7% and 30.2%, respectively.

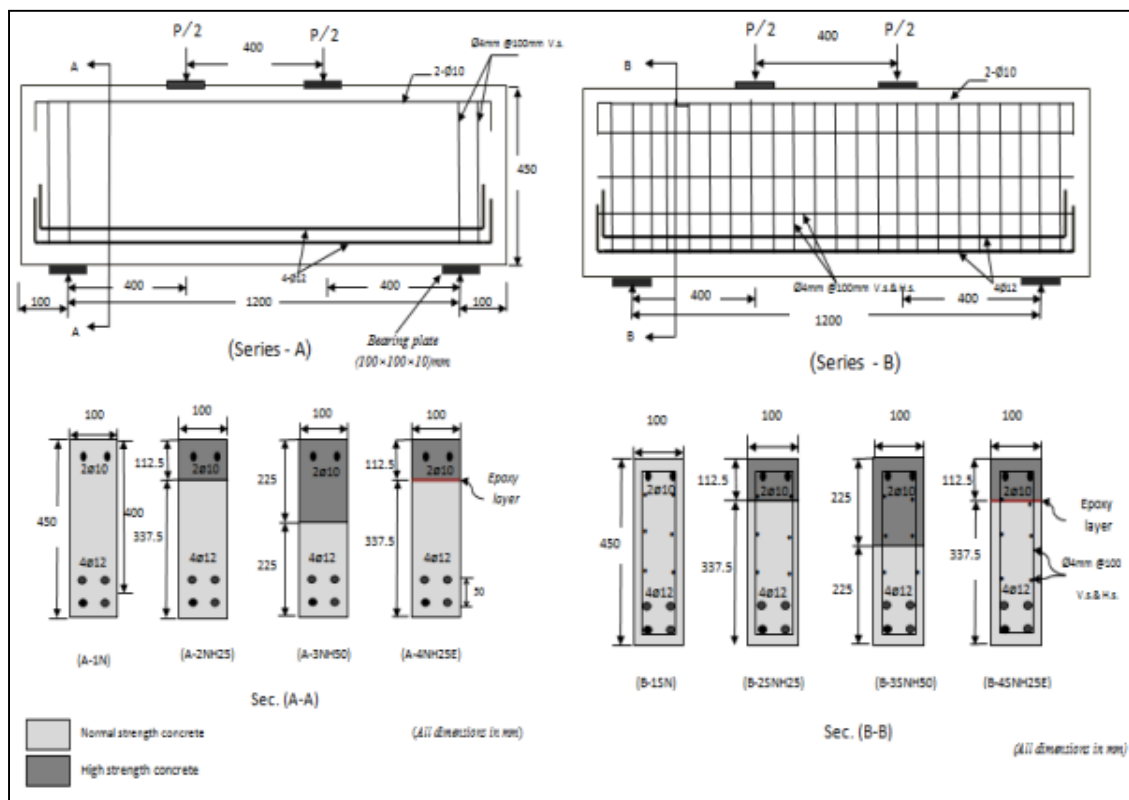


Figure 2.17 Details of the specimens and loading [48].

Hassan and Faroun, in 2016 [49], evaluated twelve specimens with flexural reinforcement and constant dimensions to ascertain how RC deep beams behaved both theoretically and experimentally under repetitive and monotonic loads. The

load type, hybrid concrete (fibrous concrete (FC) and conventional concrete (CC), ratios of web reinforcement (0.0, 0.003, and 0.004), as shown in Fig.2.18, and steel fiber content (0, 1, and 2) % were among the variables to be examined. The following is a summary of the theoretical and experimental test results:

- 1- It was found that adding steel fiber (SF) to the shear spans of the tested deep beams under monotonic system loading in ratios ranging from 0% to 2% raised the ultimate load from 29.73% to 50.81%. For hybrid deep beams with SF ratios of 2% and 1%, the capacity rose by around 42.66% and 19.45%, respectively, in comparison to deep beams without SF.
- 2- In beams with and without web reinforcing bars, the first cracking load increased by around 32.8–48 percent and 43.4–57.9 percent, respectively. Conversely, specimens without and with web reinforcement showed a 13.3-22.6% and 17.3-26.3% improvement in ductility, respectively, in hybrid concrete beams cast monolithically.
- 3- The strut and tie procedure was shown to yield conservative outcomes when contrasted with results that have been demonstrated experimentally.

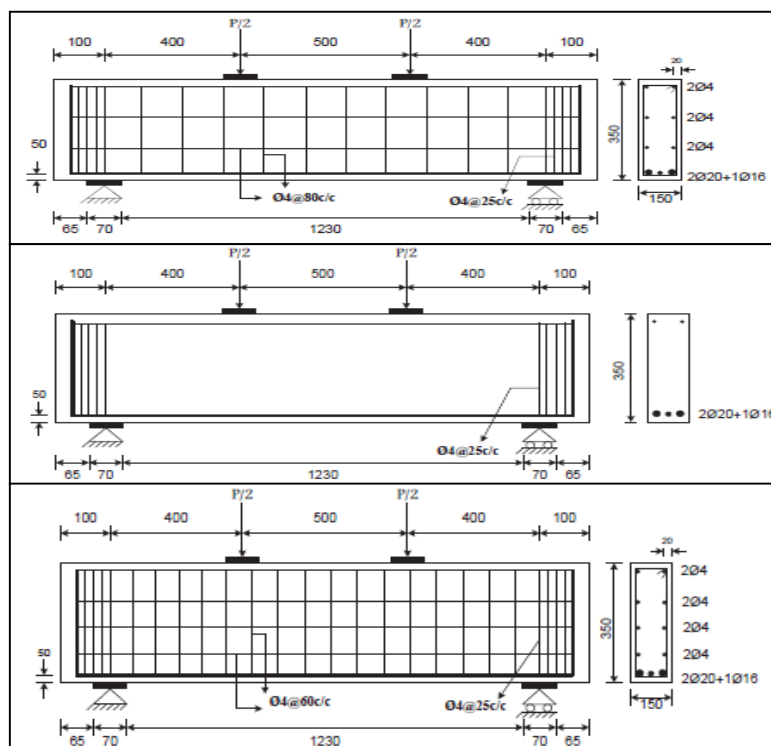


Figure 2.18 Details and dimensions of the tested specimen and loading [49].

Nabeel and Noor, in 2018 [50], examined twelve deep beams of concrete with hybrid steel and polypropylene fibers. The concrete strength was between 28 and 38 MPa, and it had circular apertures with a diameter of 110 mm and a value of $a/d=1$, as shown in Fig.2.19. The presence of apertures was found to reduce the ultimate load capacity by 50% in normal beams and by 36% in fibrous concrete. Additionally, the shear strength increased by 28%, when the a/d decreased from 1.2 to 0.8, and the mechanism of failure for all specimens was shear failure.

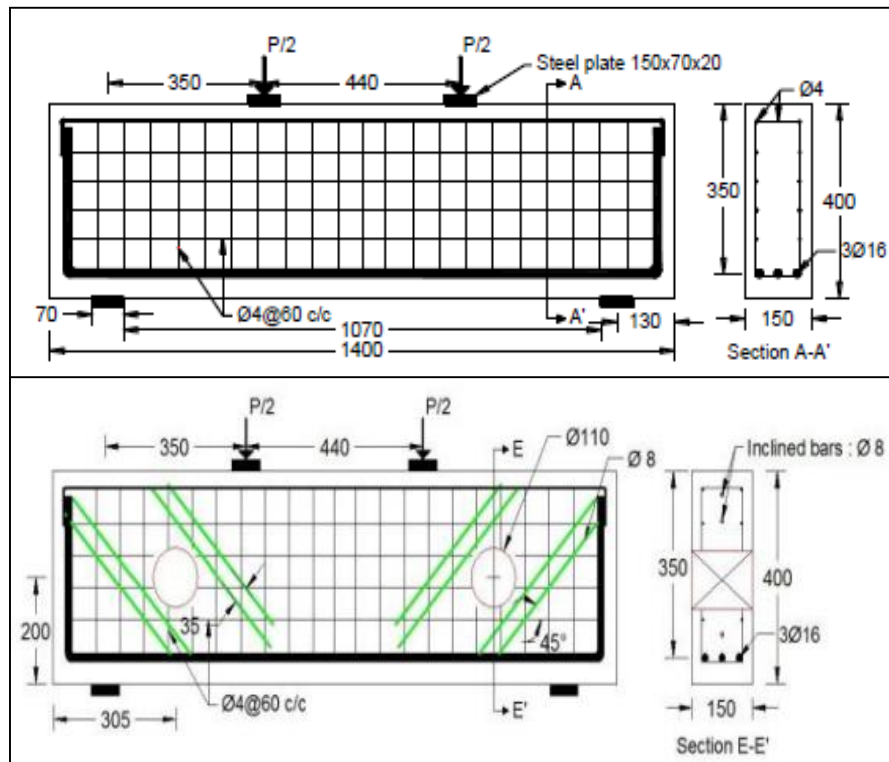


Figure 2.19 The loading and specimen's dimensions of the deep beams [50].

Saad and Rasheed in 2018 [51], conducted an experimental study on the behavior of hybrid deep beams constructed with normal strength concrete (NSC) in the compression layer and reactive powder concrete (RPC) in the tension layer, as shown in Fig.2.20. Three series of simply supported reinforced concrete deep beams were evaluated: the first comprised specimens constructed from normal-strength concrete (NSC), while the second and third groups consisted of specimens featuring hybrid cross-sections composed of two distinct concrete types: reactive powder concrete (RPC) with thicknesses of 75 mm and 125 mm in the tension zone, and NSC with thicknesses of 225 mm and 175 mm in the

compression zone for the second and third series, respectively. All beams were tested under two-point loading conditions. The shear span to total depth ratio for specimens was 0.667 and 0.4167. Experimental data indicated that the initial cracking load and load capacity were significantly enhanced by the partial incorporation of RPC. As the thickness of the RPC layer rose, it was seen that the ultimate load climbed even more. Furthermore, a reduction in the ratio of shear span to total depth (a/h) resulted in enhanced stiffness and load capacity.

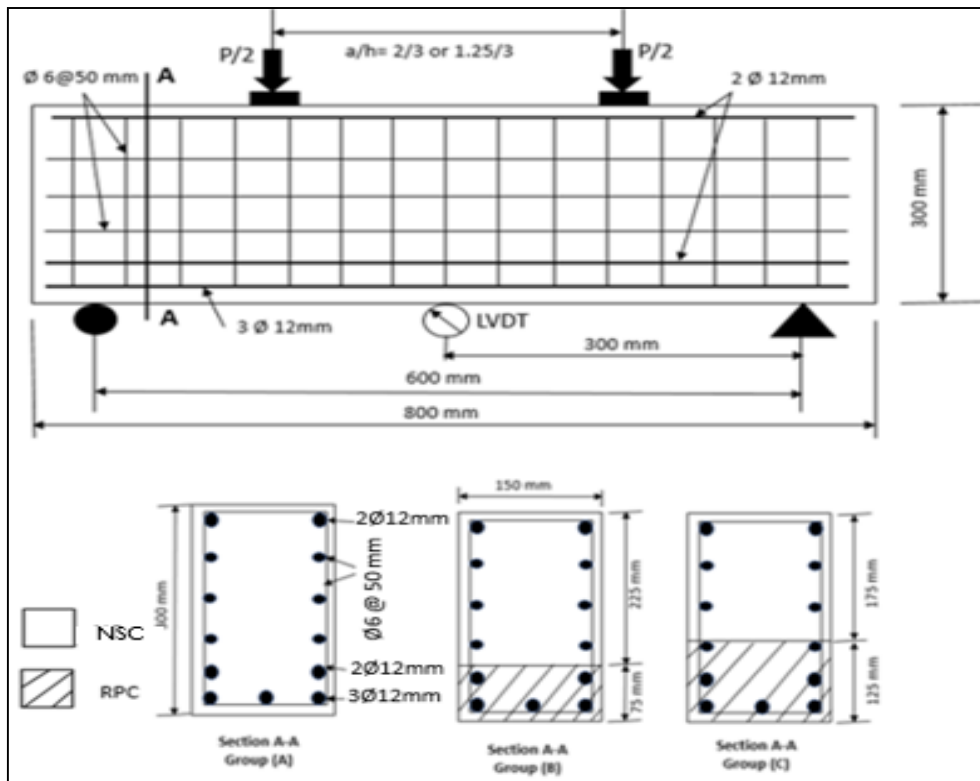


Figure 2.20 Dimensions and cross section details of the beams [51].

Sada and Resan in 2021 [52] investigated the influence of various structural parameters on the behavior of reinforced concrete deep beams, as illustrated in Fig.2.21. The study considered several factors in comparison to control specimens with rectangular cross-sections. These included changes in section shape, specifically trapezoidal configurations with varying alignment sides, and the use of hybrid compressive strengths in the compression zone.

The trapezoidal angles examined were 75° , 80° , and 85° , while the compressive strengths applied were 70, 50, and 25 MPa. The results revealed that increasing the area of high-strength concrete (HSC) within the compression zone enhanced

the shear capacity of the deep beams. Specifically, the shear strength increased by approximately 3.66% to 8.63%, depending on the HSC configuration. This improvement underscores the beneficial effect of both geometry and material strength in optimizing deep beam performance.

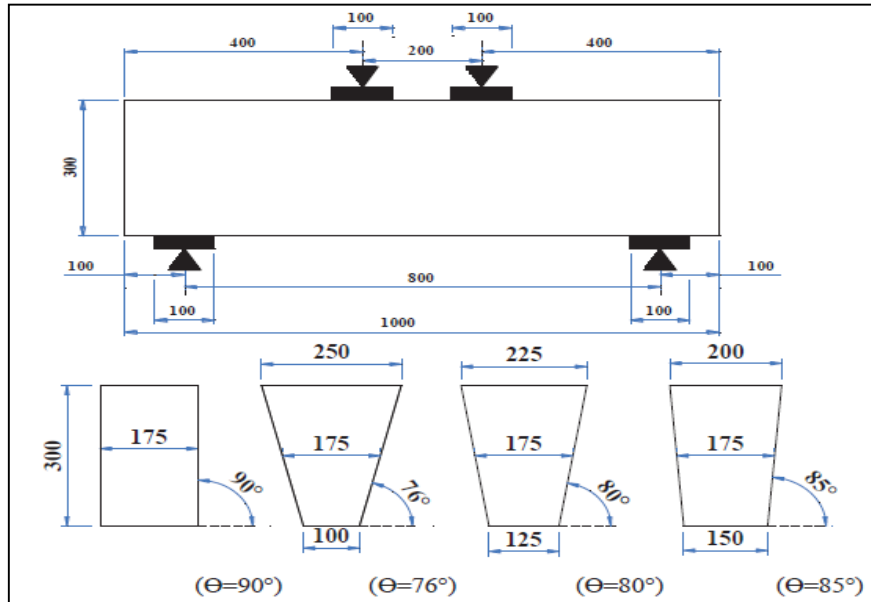


Figure 2.21 Cross sections details and dimensions of the tested beams [52].

Ahmed et al. (2021) [53], investigated the behavior of deep beams that were simply supported and had concrete layers of varying grades (25 and 50) MPa as shown in Fig 2.22.

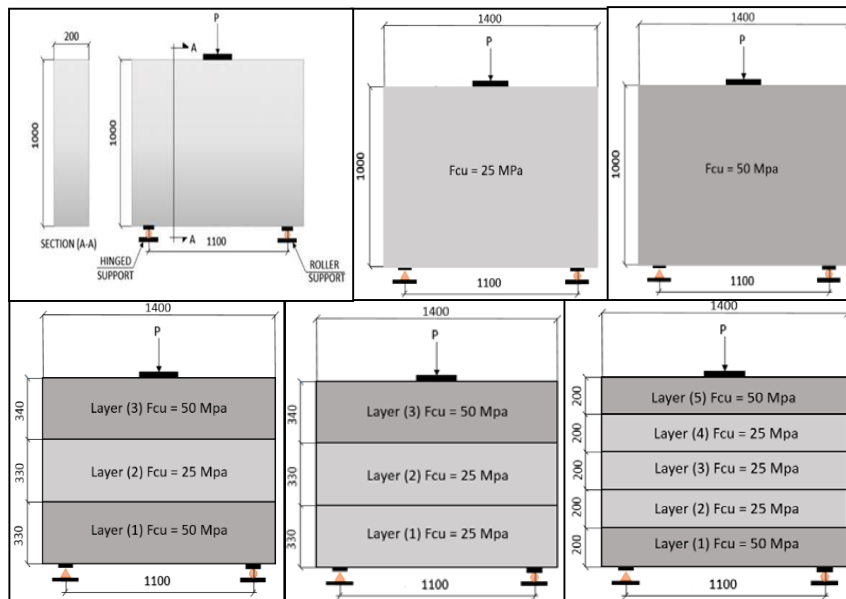


Figure 2.22 Dimensions and layered method of the graded concrete [53]

Up to failure, the tested beams were subjected to a single vertical load at mid-span. Five simply supported deep beams with identical dimensions were cast in the experiment; the specimens had the same top, bottom, vertical, and horizontal reinforcement and an effective span of 1100 mm, width of 200 mm, and height of 1000 mm. Adjacent fractures were the primary cause of investigated deep beam failure, according to experimental investigations. The first fractures emerge at an early load when concrete is cast in layers rather than in beams made of a single concrete grade.

The optimum behavior of deep beams was also discovered when the bottom layer was cast with high strength concrete. The findings related to deflection and failure load were comparable to those of deep beams formed with high compressive strength.

Yager et al. (2022) [54], proposed new functionally graded concrete deep beams for transfer girder applications without transverse reinforcement. It was built using low-cement concrete around a variety of shaped embedded high-strength struts, as shown in Fig.2.23. With a maximum total beam cement decrease of 47% in comparison to the control, the cement content in the low-cement content concrete also varied. Further exposing problems with fresh-on-hardened concrete casting was the variation in the placing technique.

Three-point bending tests were performed on the beams, and digital image correlation and distributed fiber-optic sensors (DFOS) were used for monitoring. The study showed that the biggest load capacity improvement, up to 26%, was found in diagonal-shaped embedded struts intended for three-point bending. However, load capacity was reduced when geometries incompatible with three-point bending were used.

By making it possible to see the distribution of strain in struts and measure strut and tie formations, DFOS also improved our knowledge of strut-and-tie mechanics.

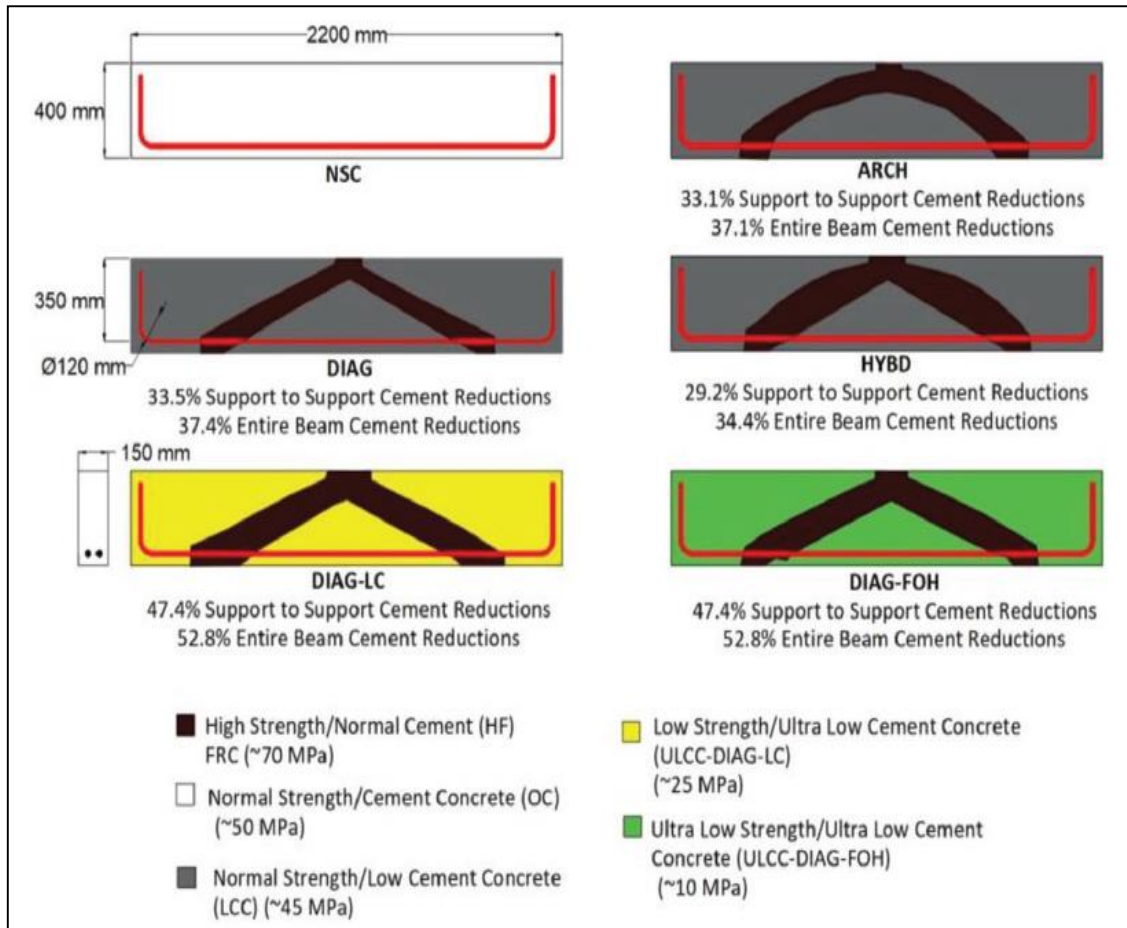


Figure 2.23 Dimensions and hybridization method of the tested beams [54].

Shakir and Hanoon, in 2023 [55], introduced a novel hybridization model termed the curved model as shown in Fig 2.24. Steel fiber concrete (SFC) was used at the upper part of the deep beams, while lightweight concrete (LWC) was utilized below it.

The capacities increased by 23% and 27% for the traditional hybrid model under the one-point and two-point loading systems, respectively. Furthermore, toughness improved by 44.7% and 143.7% for the traditional hybrid model, while the toughness of the arched hybrid model rose by 65.5% and 144.3% for the two-point loading systems respectively. The horizontal hybridization resulted in a ductility enhancement of 11.5% and 32.5%, whilst the arched hybridization achieved improvements of 12% and 37.4% for the one-point and two-point loading systems respectively.

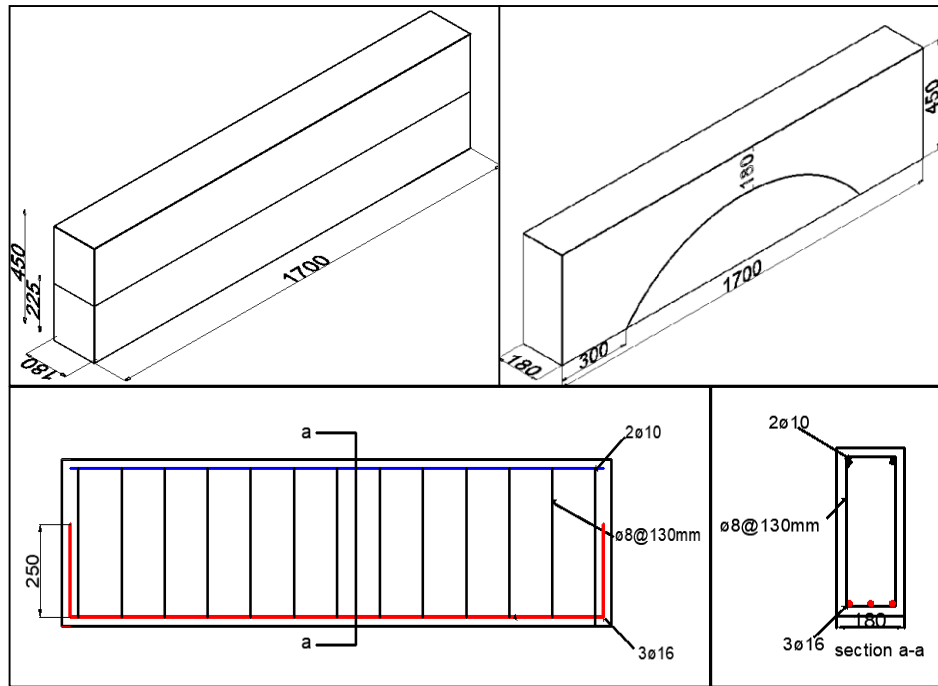


Figure 2.24 Dimensions and hybridization arrangement of the deep beams [55].

In their extension of this investigation, Shakir and Hanoon in 2023 [56] employed reactive powder concrete (RPC) in the top layer to examine the extent of performance enhancement, as illustrated in Fig 2.25. Under two-point loading tests, the load-carrying capacity increased by 34% and 36.9%, respectively. In the horizontal and arched hybrid models tested using a one-point loading system, the capacity increased by 27.6% and 39%, respectively.

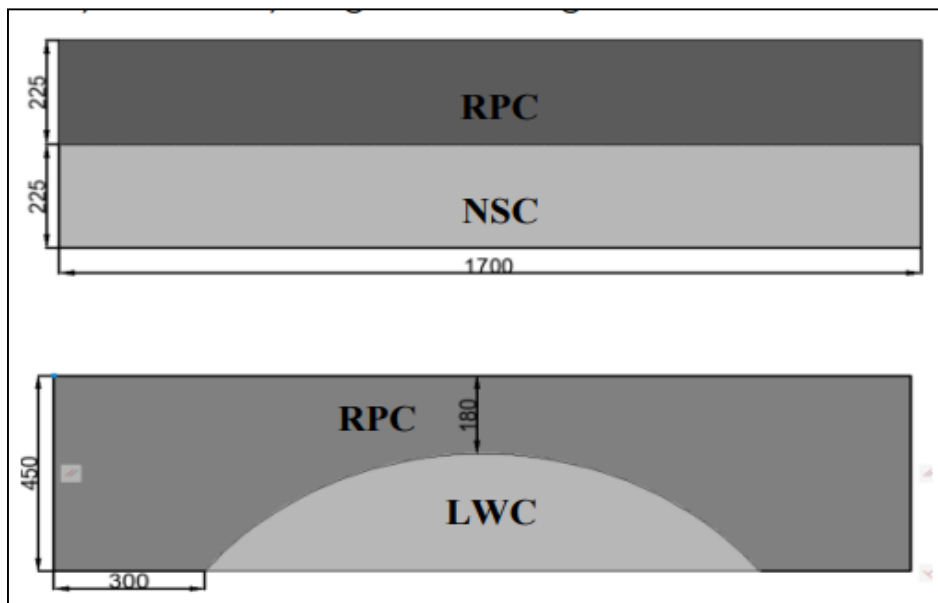


Figure 2.25 hybridization method of tested deep beams[56].

Shakir and Hanoon in 2023 [57] investigated eleven hybrid deep beams with various hybridization types and proposed two novel precast hybrid deep beam models to promote arching action: the tied-arch model and the strut-and-tie model (STM), as illustrated in Fig 2.26. Several factors were considered, including the type of hybridization, the concrete strength at the tension face, and the amount of shear reinforcement. The results showed that the first and second variants of the proposed hybrid models increased the ultimate load capacity by 27% and 39%, respectively, compared to the conventional hybrid specimen. Improvements in ductility and stiffness ranged from 33% to 108% and 140% to 375%, respectively.

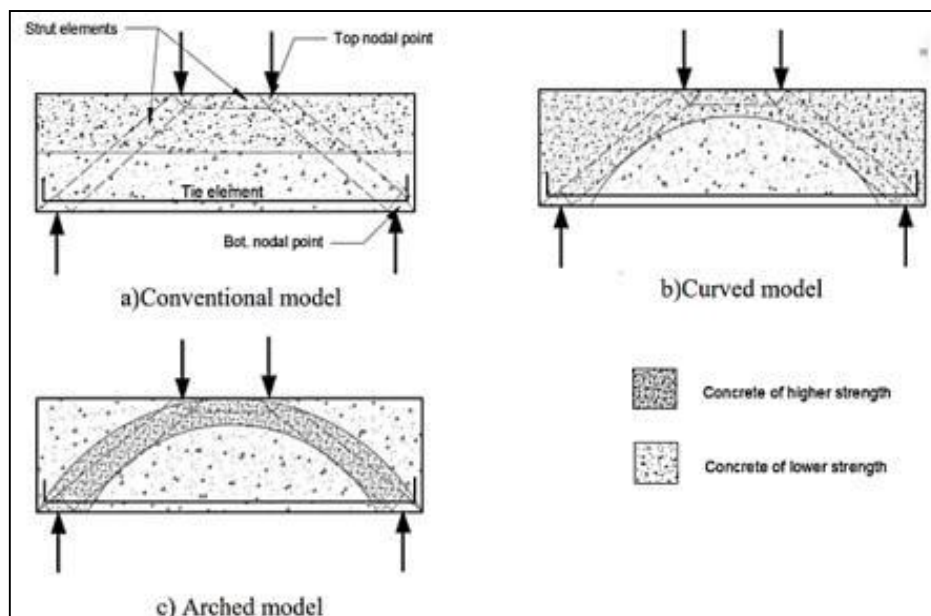


Figure 2.26 Hybrid deep beam models for this study [57].

Mohammed and Farooq in 2023 [58], introduced a novel hybrid sustainable deep beam model that substitutes crushed recycled coarse aggregates (RCA) for natural aggregates. There were three replacement ratios for RCA: 0%, 50%, and 100%. Six experimentally tested deep beam specimens under static loads were split into two groups. The first group consists of three specimens constructed using standard hybrid deep beam models, which have a top layer of normal strength concrete with steel fibers (SFC) and a bottom layer of RCA as shown in Fig 2.27 with the three replacement ratios. Three specimens with the suggested arched hybrid model, SFRC in the arch area and RCA in other beam

locations, are also included in the second group. The capacity increased by 13.5%, 19.7%, and 19.1% for the three replacement ratios, respectively, when the suggested model was used instead of the traditional hybrid model. In contrast, there were a 25.2%, 51.1%, and 62.1% improvement in flexural toughness, respectively. Additionally, the findings demonstrated that when the RCA content increased, the mode of failure for the traditional model shifted from flexure to diagonal. In contrast, the suggested model maintained the mode at a flexural trend irrespective of the RCA presence in the bottom layer. The hybridization configuration that had been proposed might be used to create environmentally friendly precast deep beams that reduce construction material waste.

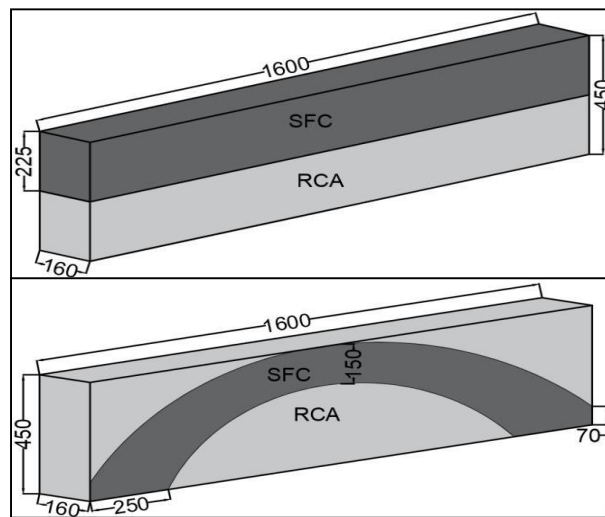


Figure 2.27 Hybrid deep beam models for this study [58].

Shakir and Alghazali in 2023 [59], reported the findings of an experimental examination of using broken concrete as recycled coarse aggregates (RCA) of hybrid deep beams. Six deep beam specimens were subjected to static load testing. Two served as controls one was non-hybrid with 100% replacement RCA, the other was non-hybrid with steel fiber concrete (SFC) and three were hybrid specimens with varying characteristics. Models of hybridization for concrete sections (horizontal, curved, and two arched beams) the upper half of compression, upper portion of curved RCA, and arch strut were cast by SFC, see Fig 2.28. This research seeks to identify the optimal distribution of concrete types for hybrid deep beams to achieve the lowest cost, including 100% recycled

concrete aggregate from building demolition debris into the concrete mixes. The behavior has been monitored by cracking and failure loads, loading history, crack breadth, and toughness. The capacities were seen to rise by 7.7%, 18.7%, 17.2%, and 28.2% in the horizontal, curved, arched, and arched with inclined stirrups hybrid models, respectively, as compared to the control specimen using RCA. Furthermore, toughness was increased for the identical specimens by 50.9%, 71.1%, 100.5%, and 144.6%, respectively, in comparison to the control specimen containing RCA.

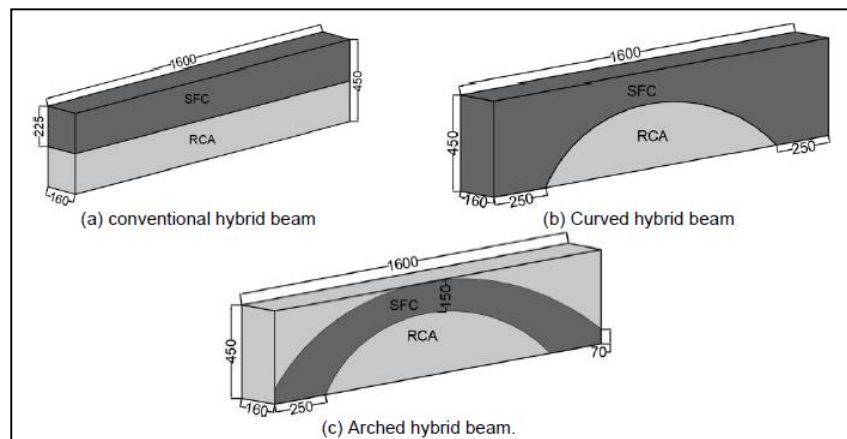


Figure 2.28 Details of the geometry of the Hybrid deep beams [59].

Shakir and Alghazali in 2024 [60], The use of discarded building materials to create economical and environmentally friendly structural elements, including deep beams, has gained attention in recent years. The current study compares the horizontally hybrid model with a new sustainable concept of a hybrid deep beam. Experimental testing has been done on nine specimens under mid-span static loading till failure. Steel fiber concrete (SFC) makes up the arch region of the suggested model, while concrete with recycled coarse aggregate (RCA) in three different replacement ratios (0%, 50%, and 100%) makes up the other areas. Three sets of specimens each are used to represent the modified model (ARC2), the suggested model (ARC1), and the traditional model, ARC1 was reinforced with vertical stirrups, ARC2 was reinforced with inclined stirrups, and conventional model without arch reinforcement as shown in Fig 2.29. Cracking load, failure load, crack breadth, fracture pattern, and toughness have all been

examined in relation to the reaction. According to the results, for the three RCA values, the suggested model ARC1 increased capacity by 6.7%, 6.8%, and 9.4% when compared to the traditional hybrid model. In contrast, the ARC2 model's capacity increased by 13.5%, 19.6%, and 19.1%. Comparing the ARC1 model to the conventional hybrid model, improvements of 12.5%, 18.7%, and 32.9% were found in terms of toughness. In contrast, it is improved by 25.2%, 51.1%, and 62.1% for model ARC2, respectively. The suggested hybrid models could help lower building costs and lessen the negative environmental consequences of construction material waste.

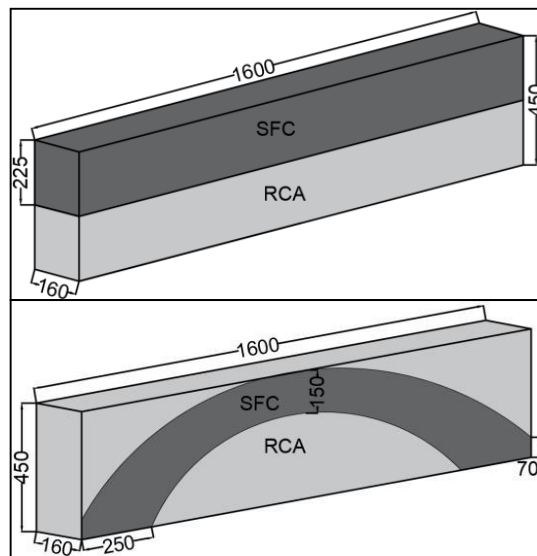


Figure 2.29 Details of the Hybrid deep beams [60].

Shakir and Alghazali in 2024 [61], This paper proposes three new sustainable hybrid deep beam specimens as shown in Fig 2.30. The curved (CRV), the arched (ARC1), and the modified arched (ARC2), alongside the standard hybrid model (HRL) that utilizes recycled coarse aggregates (RCA) in place of natural aggregates. The examples demonstrate that steel fiber concrete (SFC) is used in regions of significant stress concentration, whereas sustainable concrete is utilized in other locations. The impacts of hybridization kinds and inclined stirrups have been thoroughly examined concerning the parameters. The results indicated that the failure capacity rose by 8%, 22%, 21%, and 22% for the corresponding hybrid models. Conversely, the specimen with SFC exhibited a

19% increase. The flexural toughness improved by 13%, 39%, 34%, and 71% for the hybrid models, respectively, in comparison to the non-hybrid model (CTRL-R50). The augmentation for the control specimen with SFC was 52%. The findings indicated a modest range of improvement in effective stiffness, between 1.5% and 9%. The internal reinforcing detailing of the specimens is sufficient to prevent the semi-diagonal mode of failure, which is very brittle. Moreover, a replacement rate of up to 50% does not substantially impact the total response. Furthermore, the test findings demonstrated that the inclined arrangement of the stirrups was more effective in preventing diagonal cracking than their vertical configuration. The suggested curved and arched models can accommodate several focused loads, prestressed beams, and precast walls. The suggested models intend to generate lightweight, sustainable, low-cost, high-performance precast deep beams in comparison to the horizontal hybrid model.

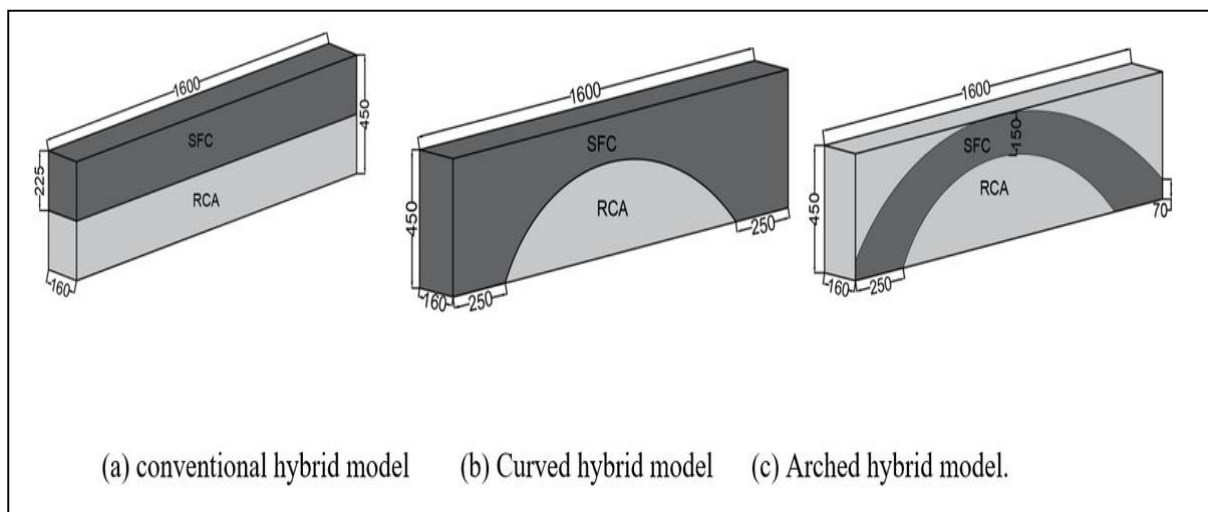


Figure 2.30 Details of the Hybrid deep beams [61].

2.6 Concluded Remarks:

1. One of the primary factors influencing the failure mode of deep beams whether shear or flexural is the shear span-to-effective depth ratio (a/d). This ratio significantly affects the ultimate strength and the formation of diagonal cracks. As the shear span-to-effective depth ratio increases, the shear capacity of the deep beam decreases accordingly.

2. When the shear span-to-depth ratio is high, the shear capacity of deep beams is notably influenced by vertical shear reinforcement, whereas horizontal reinforcement has a lesser effect.
3. Shear capacity is enhanced by increasing the main tension steel reinforcement, especially when the shear span-to-depth ratio is moderate. However, this improvement diminishes as the shear span-to-depth ratio becomes large. Moreover, excessively increasing the reinforcement does not lead to further gains in shear capacity.
4. The behavior of reinforced concrete deep beams is influenced by various factors, including the shear span-to-depth ratio (a/h), concrete compressive strength (f'_c), longitudinal reinforcement ratio, vertical and horizontal shear reinforcement ratios, and the clear span-to-depth ratio.
5. Fibers improve the shear resistance and diagonal cracking capacity of deep beams, thereby enhancing their overall behavior and structural performance. Steel fiber-reinforced concrete has been demonstrated to increase the load-carrying capacity and performance of solid deep beams, and in some cases, steel fibers can partially substitute conventional shear reinforcement.
6. Increasing the shear span-to-effective depth ratio (a/d) leads to greater maximum deflection while reducing both the first cracking load and the ultimate load capacity.
7. Using lightweight concrete instead of normal-weight concrete results in reduced initial cracking and ultimate loads. Generally, lightweight concrete deep beams exhibit behavior similar to that of normal concrete, with differences in ultimate shear strength and cracking load primarily attributed to variations in the tensile capacity of the concrete types.
8. The introduction of steel cages at the supports significantly increased the deep beam's load-bearing capacity and altered its failure mode.
9. In recent years, there has been growing interest in using recycled construction materials to produce cost-effective and environmentally

friendly structural components, such as deep beams. The proposed hybrid models have the potential to lower construction costs while reducing the negative environmental effects associated with material waste.

10. The hybridization of concrete in deep beams has shown significant improvements in load-carrying capacity and overall structural performance, especially when implemented in the strut region.
11. The arched shape of the struts provides a higher load-bearing capacity compared to traditional straight strut configurations.
12. First cracks tend to develop at lower loads in beams cast with layered concrete compared to those made from a single type of concrete.
13. Optimal flexural performance in deep beams was observed when the bottom layer was made of high-strength concrete. The resulting deflection and failure load were comparable to those of deep beams constructed entirely with high-strength concrete.

2.7 Research Gap

By reviewing the scope of previous studies on the main cases and identifying gaps in the existing research, the aim of this study was to address the unexplored areas and contribute new insights to the field.

1. Previous studies have not adequately explored the impact of replacing conventional reinforcing bars with steel sections for strut strengthening.
2. The incorporation of internal ribs within arches, serving as supports for the main arch, has not been explored in studies addressing the geometry of arched hybrid systems.
3. Furthermore, the configuration of arched hybrid systems with connected or continuous ends has not been examined in the existing literature.
4. The use of built-up steel sections similar to those used in steel columns for reinforcing struts was also not considered in previous research.

CHAPTER THREE: EXPERIMENTAL PROGRAM

3.1 Introduction

This chapter outlines the testing program, including specimen identification, dimensions, internal configurations, and the experimental procedures followed in this study. The results of the trial mixes confirmed that the materials used met the consistency requirements specified by relevant standards. The specimens were designed and analyzed using the Strut-and-Tie Model (STM) in accordance with ACI 318M-19 [9]. Two types of concrete were employed in casting the hybrid deep beams to evaluate their performance under the proposed testing conditions. The experimental work was carried out in the Construction Laboratory of the College of Engineering at the University of Misan. A summary of the key parameters considered in the research is presented in Table 3.1.

Table 3.1 Used parameters.

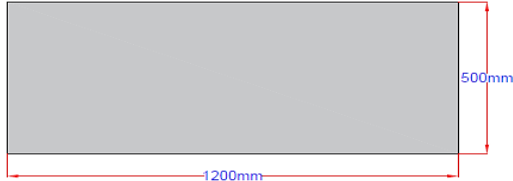
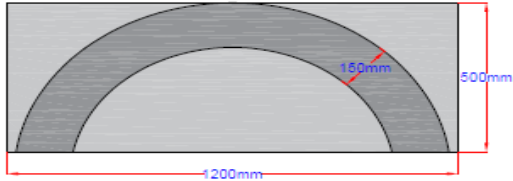
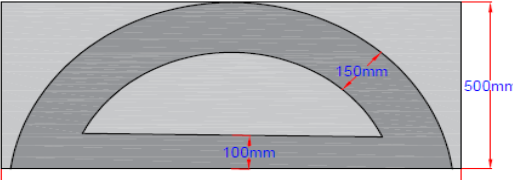
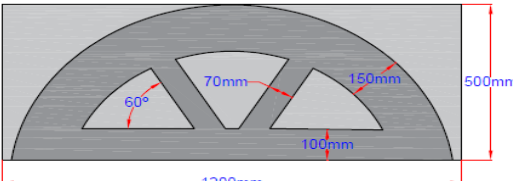
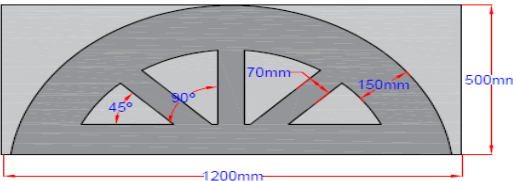
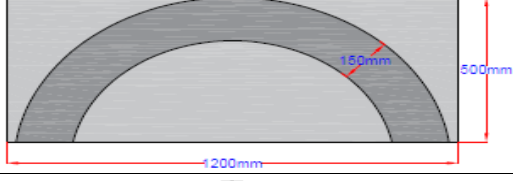
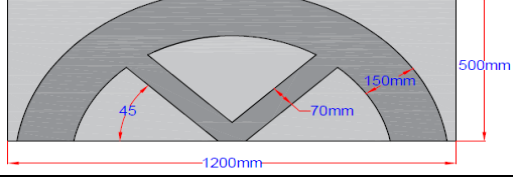
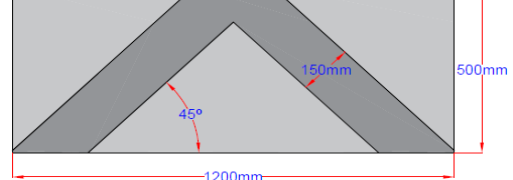
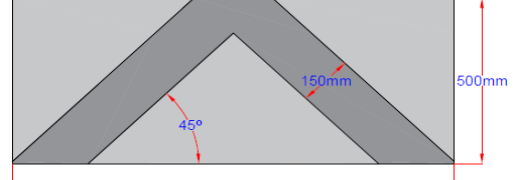
No.	Beams Variables	Details
1	Concrete type	Normal strength concrete (NSC) and High strength concrete (HSC)
2	Hybridization Shape	Arch and Triangle shape
3	Reinforcement Type	Steel Bar and Angle Steel Section

3.2 Specimens Description and Coding

In this study, the structural behavior of fifteen reinforced concrete deep beams was investigated. Each beam had identical dimensions: 1200 mm in length, 500 mm in depth, and 150 mm in thickness. All specimens were subjected to a single-point load applied at the mid-span. The specimens were categorized into four groups (G1 to G4) based on variations in reinforcement configuration, type of strut reinforcement, hybridization shape, and the location of hybrid zones within the beam.

Table 3.2 provides a comprehensive overview of the specimens used in this study, including their identification codes, structural configurations, and key distinguishing parameters.

Table 3.2 details of deep beams

Groups No.	No.	Coding	Beam description	Beams geometry
G1	1	G1-CO-1	Controls beam	
	2	G1-CO-2		
	3	G1-CO-3		
	4	G1-CO-4		
G2	1	G2-HA-B-1	Arched hybrid struts reinforced with steel rebars	
	2	G2-HA-B-2		
	3	G2-HA-B-3		
	4	G2-HA-B-4		
G3	1	G3-HA-S-1	Arched hybrid struts reinforced with steel angle sections	
	2	G3-HA-S-2		
	3	G3-HA-S-3		
G4	1	G4-HT-S-1	Triangle hybrid struts reinforced with steel angle sections	
	2	G4-HT-S-2		
	3	G4-HT-S-3		
	4	G4-HT-S-4		

G: Group Number
T: Triangle Shape

Co: Control
B: Steel Bar Reinforcement

H: Hybridization

A: Arch Shape

S: Steel Angle Section

The first group, **G1**, consisted of four reinforced concrete deep beams and served as the control group, as no concrete hybridization was applied. All specimens in this group were reinforced with the same rebar configuration in tie region: 2Ø16 mm and 2Ø12 mm bars.

The first two beams, (**G1-CO-1**) and (**G1-CO-2**), were cast using normal-strength concrete (NSC). The third and fourth beams, (**G1-CO-3**) and (**G1-CO-4**), were cast using high-strength concrete (HSC). Beams (**G1-CO-1**) and (**G1-CO-3**) featured a triangular strut configuration, while (**G1-CO-2**) and (**G1-CO-4**) had an arched strut, as shown in Fig.3.1. All beams in this group shared the same strut reinforcement, consisting of 4Ø8 mm longitudinal bars and Ø4 mm stirrups spaced at 75 mm center-to-center.

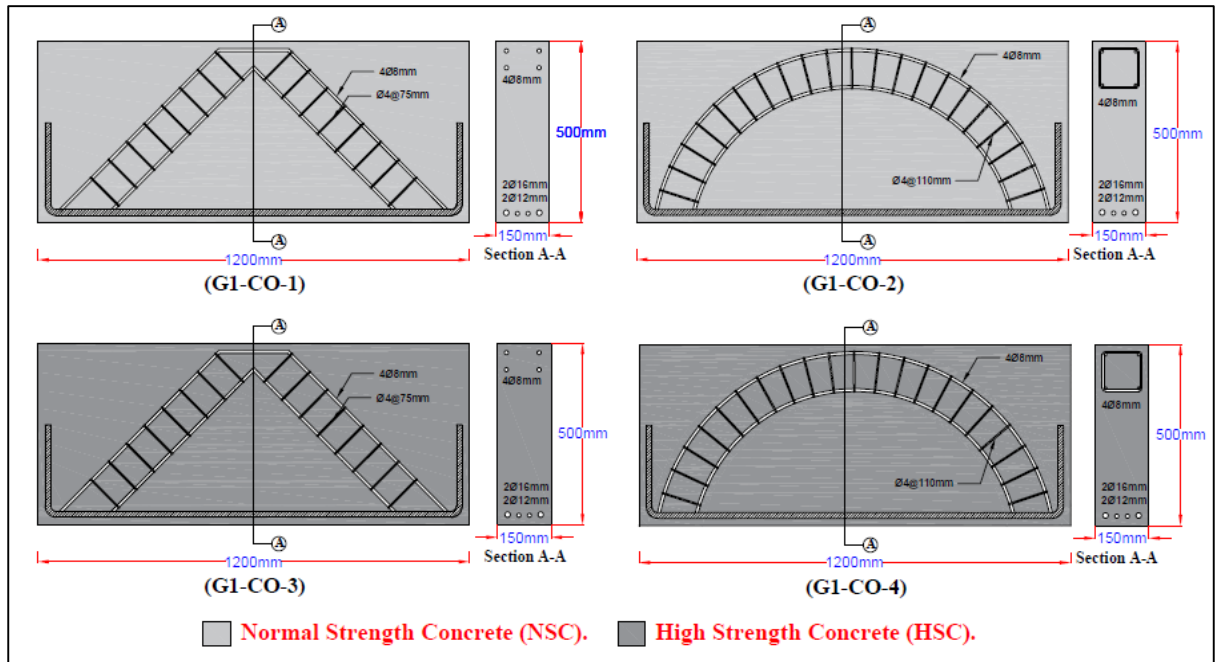


Figure 3.1 Group one (G1) deep beams details.

The second group, **G2** consisted of four hybrid deep beams in which high-strength concrete (HSC) was used in the arched strut region, while normal-strength concrete (NSC) was applied to the remaining areas of the beam, as shown in Fig.3.2. All beams featured an arched strut configuration. The strut

reinforcement for all specimens included four 4Ø8 mm longitudinal bars and Ø4 mm stirrups spaced at 75 mm center-to-center.

The first beam (**G2-HA-B-1**) was reinforced at the tie region with 2Ø16 mm and 2Ø12 mm bars. In beams (**G2-HA-B-2**), (**G2-HA-B-3**), and (**G2-HA-B-4**), high-strength concrete was also used in the tie zone, which was reinforced with 2Ø16 mm and 2Ø12 mm bars, along with Ø4 mm stirrups spaced at 75 mm center-to-center. Beam (**G2-HA-B-3**) has two additional ribs oriented at 60°, while beam (**G2-HA-B-4**) featured three ribs: two inclined at 45° and one vertical at 90°. All ribs were made of high-strength concrete and reinforced with 4Ø8 mm longitudinal bars and Ø4 mm stirrups at 75 mm spacing.

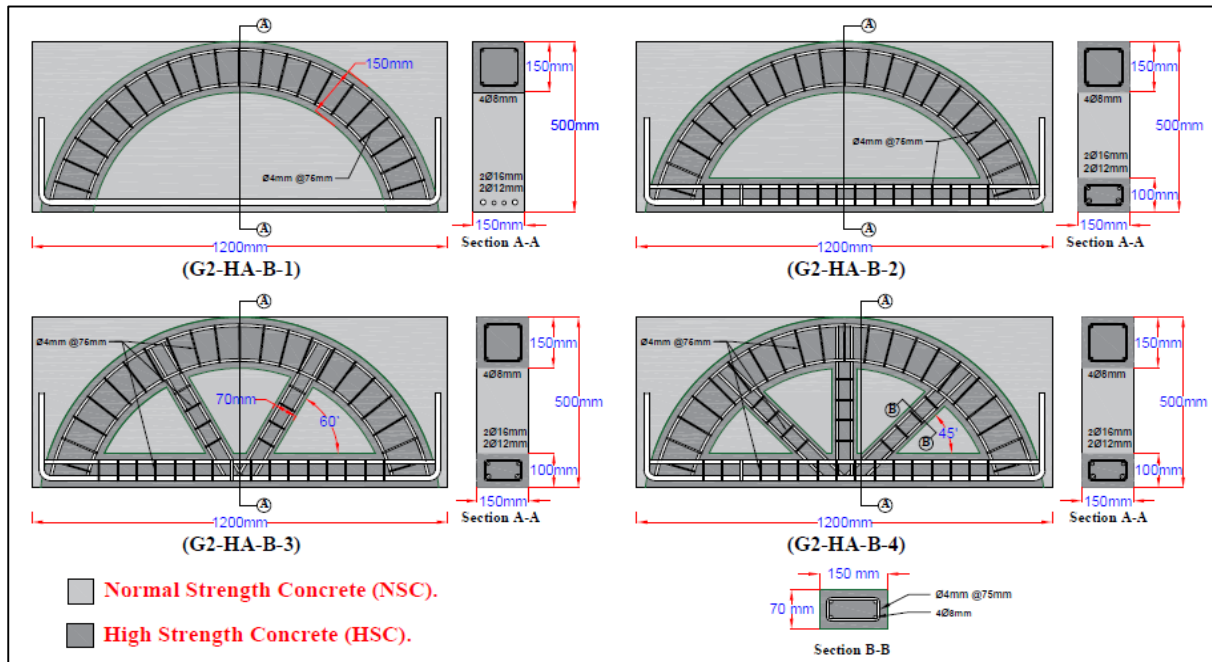


Figure 3.2 Group two (G2) deep beams details.

The third group **G3**, consisted of three hybrid arch-shaped reinforced deep beams, with (HSC) in the strut region and (NSC) for the remaining regions. All beams had identical tie reinforcement, comprising 2Ø16 mm and 2Ø12 mm bars. The strut areas of all specimens were reinforced using steel angle sections with measuring of 40×40×4 mm, connected together using steel plates measuring 30×4 mm spaced 110 mm, apart by welding.

The first specimen (**G3-HA-S-1**) featured a strut reinforced with four steel angle sections tied together. The second specimen (**G3-HA-S-2**) utilized two angle steel sections for strut reinforcement. The final specimen in this group (**G3-HA-S-3**) had its strut reinforced with two steel angle sections and additionally supported by two angle steel ribs embedded in high-strength concrete at an inclination of 45° . Fig.3.3 illustrates the details of the specimens in this group.

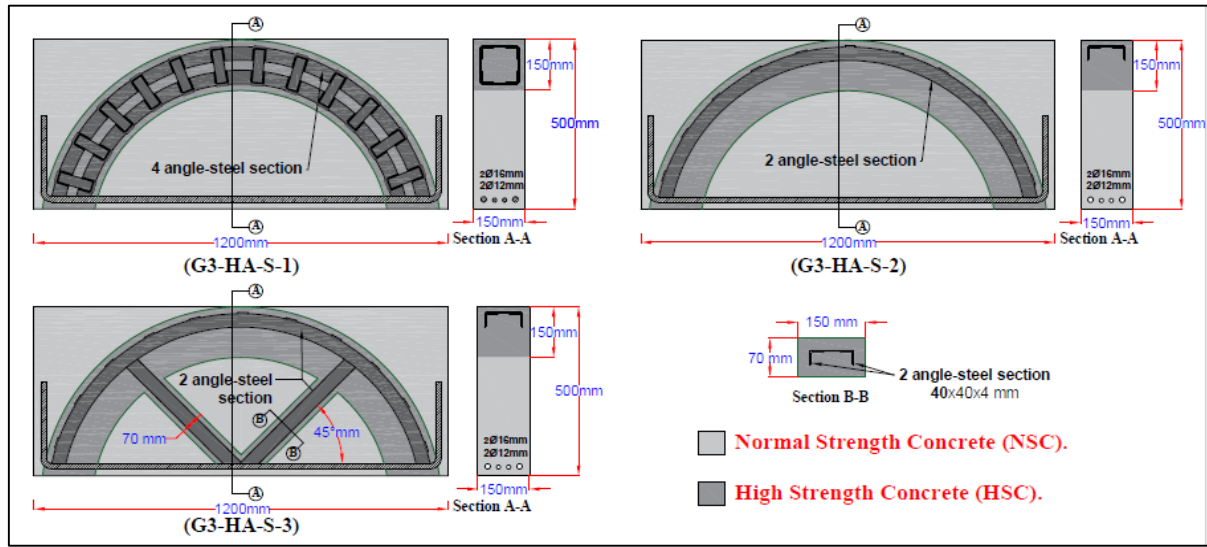


Figure 3.3 Group three (G3) deep beams details.

The fourth and final group **G4**, consisted of four hybrid deep beams. In this group, the strut regions were cast with high-strength concrete in a triangular configuration, while the remaining portions of the beams were made with normal-strength concrete.

All struts were reinforced using steel angle sections measuring $40 \times 40 \times 4$ mm, connected together using 30×4 mm steel plates by welding. All beams in this group had the same tie reinforcement $2\text{Ø}16$ mm and $2\text{Ø}12$ mm bars except for beam (**G4-HT-S-2**), in which the $2\text{Ø}16$ mm bars were replaced with angle steel. In beams (**G4-HT-S-1**) and (**G4-HT-S-2**), the struts were reinforced with four opposing steel angle sections tied together. In beams (**G4-HT-S-3**) and (**G4-HT-S-4**), the strut area was reinforced with two steel angle sections.

Additionally, beam (G4-HT-S-3) included a steel angle sections to connect the struts at the middle. Fig.3.4 presents the detailed configurations of the specimens in this group.

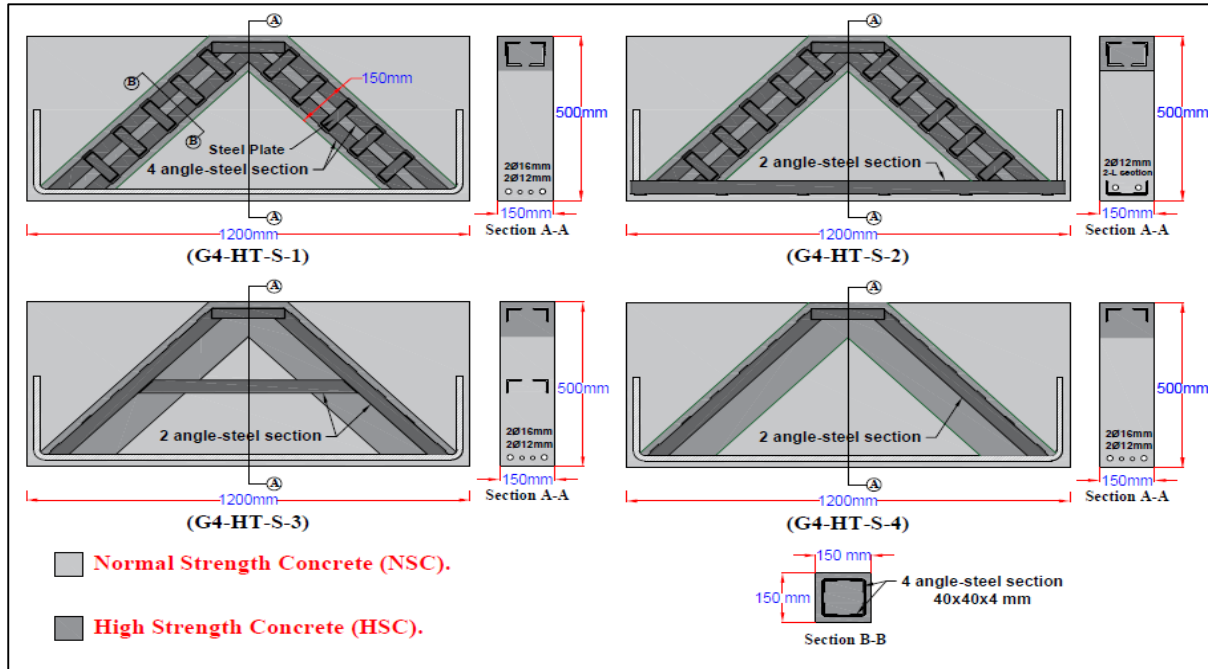


Figure 3.4 Group four (G4) deep beams details.

3.3 Materials Properties

All materials used in this study were available in local markets and stored away from moisture and weather which might affect their properties. The properties of materials used in this study were tested as described in the subsection below.

3.3.1 Cement

In this study, ordinary Portland cement type (I) of Crista company was used and stored in a place away from weather conditions that affect its properties. Physical, mechanical and chemical tests were conducted to determine its properties according to Iraqi specifications (IQS No.5/2019)[62]. These tests were conducted inside the laboratory of the College of Engineering at the University of Misan. Tables 3.3 and 3.4 show these properties.

Table 3.3 Chemical composition of cement.

Compound Composite	Content (%)	Limits of IQS No. 5/2019[62]
MgO	2.73	$\leq 5 \%$
Limes (Cao)	62.3	-
Silicas (Sio ₂)	23.5	-
SO ₃	2.17	$\leq 2.8\%$
Alumina's (Al ₂ O ₃)	3.15	-
Iron oxidizes (Fe ₂ O ₃)	4.56	-
Loss of Ignition	3.21	$\leq 4\%$
Insoluble Materials	1.15	$\leq 1.5\%$
Lime Saturation Factor	0.90	0.66 – 1.02

Table 3.4 Properties of cement.

Physical properties	Test result	Limits of IQS No. 5/2019[62]
Fineness Using Blaine Air Permeability Apparatus (m ² /kg)	257	≥ 250
Setting time Using Vicat's Instruments Initial (hrs: min.) Final (hrs: min)	1:22 8:17	$\geq 45\text{min}$ $\leq 10\text{hr}$
Compressive Strength 2 days (MPa) 28 days (MPa)	19.03 34.33	≥ 10 ≥ 32.5

3.3.2 Fine Aggregate (Sand)

Two grades of sand were used in this study. Natural sand of maximum size of 4.75 mm was used for casting normal strength concrete, while for high strength concrete, fine natural sand with a maximum size of 1.18 mm was utilized. Both types are provided from natural sources in Basra Governorate, which meet the Iraqi Specification IQ.S45/1984[63], as shown in Table 3.5 and Fig 3.5.

Table 3.5 Grading of the fine aggregates.

No.	Sieve Size(mm)	Percent of Passing%	Iraqi Specification IQ.S45/1984[63] for Zone (2)
1	10	100	100
2	4.75	97.8	90 - 100
3	2.36	88.8	75 - 100
4	1.18	75.4	55 - 90
5	0.6	57	35 - 59
6	0.3	26.6	8 - 30
7	0.15	3.4	0 - 10
Materials Passing through a sieve 75 micron %		4.2	$\leq 5\%$

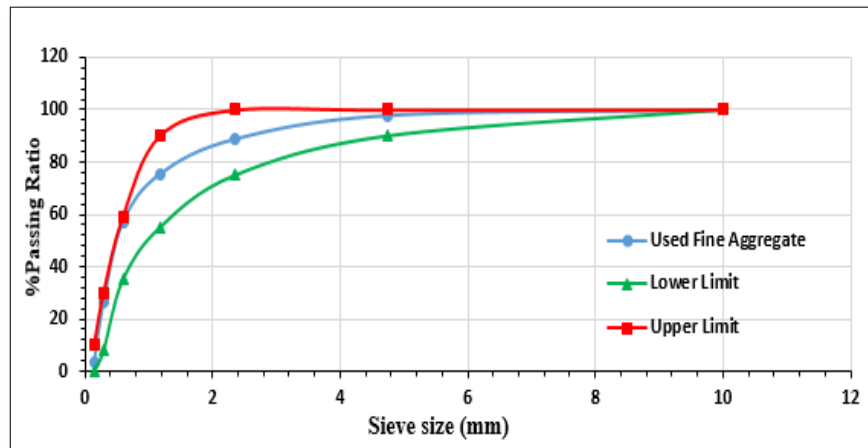


Figure 3.5 Sieve analysis of fine aggregate compared to standard limits.

3.3.3 Coarse Aggregate (Gravel)

Two different grades of coarse aggregate were used. The first consisted of crushed gravel with a maximum size of 19 mm, used in normal-strength concrete. The second was natural crushed gravel with a maximum size of 12 mm, used for producing high-strength concrete. It was hand-sieved and thoroughly washed, as shown in Figure 3.6. Both types of aggregate conform to the Iraqi Specification IQ.S45/1984 [63], as presented in Table 3.6 and Fig 3.7.

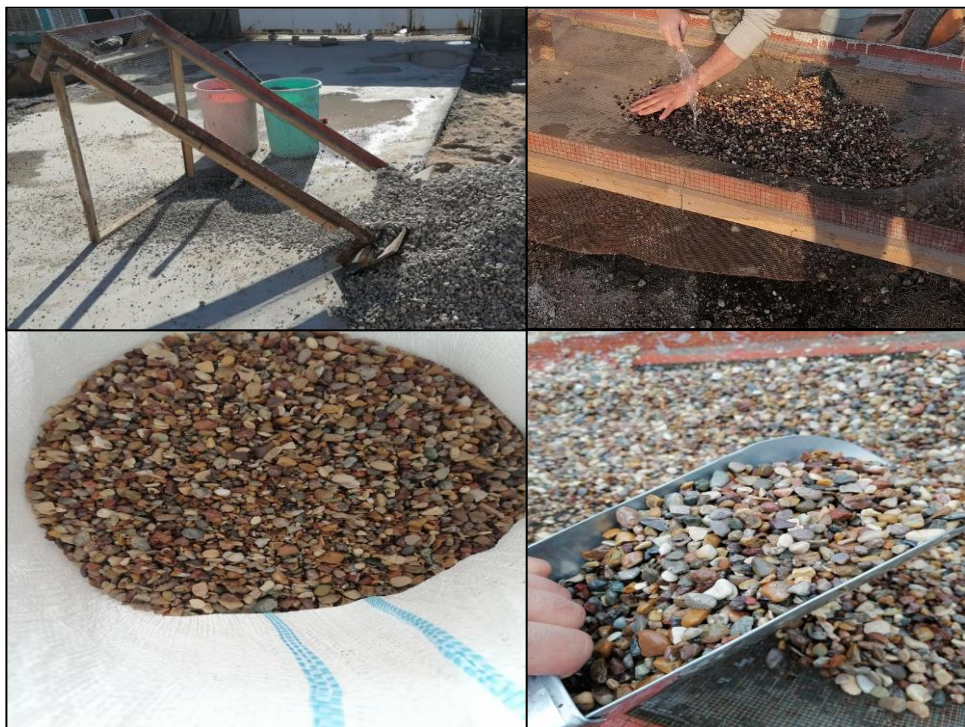


Figure 3.6 Stages of hand-sieving, washing and packing gravel.

Table 3.6 Grading of the fine aggregates.

No.	Sieve Size(mm)	Percent of Passing%	Iraqi Specification IQ.S45/1984[63] for Zone (2)
1	37.5	100	100
2	20	96.6	95 – 100
3	10	39.2	30 – 60
4	5	1.8	0 - 10
Materials Passing through a sieve 75 micron %		0.2	$\leq 3\%$

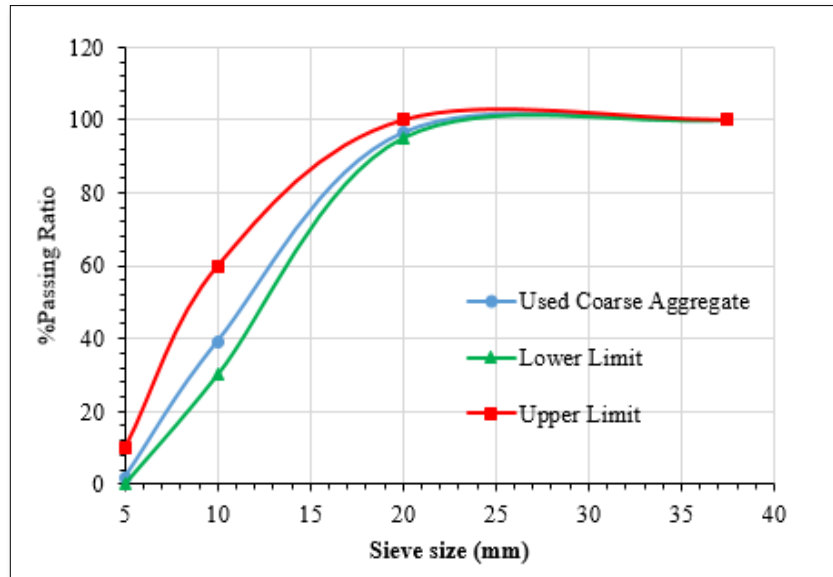


Figure 3.7 Sieve analysis of coarse aggregate compared to standard limits.

3.3.4 Water

In this study, Reverse osmosis (RO) water was used in the mixing and curing process for both types of concrete (normal strength and high strength) and the water content was in accordance with the Iraqi standard (IQS 1703/2018) [64].

3.3.5 Silica Fume

Silica fume, composed of ultrafine spherical particles typically less than 1 μm in diameter, is a highly efficient pozzolanic material. It is a byproduct generated during the production of ferrosilicon alloy and silicon metal, and it significantly enhances the properties of concrete. The test results for the silica fume used in this study are presented in Tables 3.7 and 3.8. This type of silica fume is commonly available in the local market in 20 kg sacks. According to the data

sheet provided in Appendix A, it complies with ASTM C1240-03 [65] and was used in the present experimental program.

Table 3.7 Typical properties for Silica fume [65].

Table Property	Value
State	Sub-micron powder
Color	Gray powder
Specific gravity	2.10 to 2.4
Bulk density	500 to 700 kg/m ³

Table 3.8 Chemical and physical properties of Silica fume.

Chemical properties.		
Oxides composition	Oxides content %	limit of ASTM C1240-15[65]
SiO ₂	92.5	Min. 85
Al ₂ O ₃	0.75	< 1
Fe ₂ O ₃	0.49	< 2.5
CaO	CaO 0.87 < 1	CaO 0.87 < 1
SO ₃	SO ₃ 0.88 < 1	SO ₃ 0.88 < 1
L.O.I	5.3	Max. 6
Cl	0.1	Cl 0.1 < 0.2
K ₂ O+Na ₂ O	1.76	< 3
Physical properties		
Property ASTM	Result	C1240-15
Pozzolanic activity index	108%	≥ 105%
Moisture content	0	≤ 3%
Specific surface area m ² /gm	16.5	> 15

3.3.6 Super Plasticizer

Sika ViscoCrete-180 GS, based on third-generation polycarboxylate polymer technology, is a high-range water-reducing and superplasticizing admixture for concrete. In the present study, it was used to improve workability while maintaining high concrete strength by reducing the water-to-cement ratio. The product data sheet is provided in Appendix B. The properties of the superplasticizer are presented in Table 3.9.

Table 3.9 Properties of Super Plasticizer[66] .

	Paragraph	Description
1	Chemical base	viscocrete polycarboxylate polymer
2	Appearance /colors	Light brownish
3	Specific gravity @25°C	$1.070 \pm (0.02) \text{ g/cm}^3$
4	pH- Value	4 - 6
5	Dosage	(0.5 % - 2 %) by weight of total cementitious materials.
6	Shelf life	12 months from date of production if stored properly in undamaged unopened,
7	Storage condition	In dry conditions at temperatures between +5°C and +35°C. Protect from direct sunlight. It requires recirculation when held in storage for extended periods.

3.3.7 Steel Bars

In this study, four types of deformed steel rebar sizes of Ø16, Ø12, Ø8 and Ø4 mm, were used. They are available in local markets. The tests of the steel reinforcement conformed to the ASTM A615/A615M-20 standards [67], as seen in Table.3.10 and Fig 3.9.

Table 3.10 Properties of reinforcing bars (average) [67] .

$D_{nominal}$ (mm)	Area (mm ²)	Test results	
		Yield strength (N/mm ²)	Ultimate strength (N/mm ²)
16 mm	200.96	480	641
12 mm	113.04	508	660
8 mm	50.24	338	563
4 mm	12.56	280	440



Figure 3.8 Reinforcement bar testing machine.

3.3.8 Steel Sections

In this study, angle steel sections of 40×40×4mm were used as an alternative to reinforcement of the struts. Steel plates of 30×4 mm were used to connect the angles as shown in Fig.3.10. The samples were examined according to (ASTM E8/E8M-22) [68]. Table 3.11 shows the properties of the steel used.



Figure 3.9 Steel section used in this study.

Table 3.11 Properties of steel sections (average) [68] .

Steel Section Type	Dimension (mm)	Test results	
		Yield strength (N/mm ²)	Ultimate strength (N/mm ²)
L-section	40 × 40 × 4	435	544
Steel plate	30 × 4	381	488

3.3.9 Welding Wires

In this study, Chinese-manufactured welding wire readily available in local markets and regarded as a good-quality type was used in the welding of angle steel sections (see Fig 3.11). Table 3.12 presents selected properties of this welding wire in accordance with the American National Standard AWS D1.1/D1.1 M:2020 [69].



Figure 3.10 welding wire type.

Table 3.12 Properties of welding wires [69].

	Paragraph	Description
1	Type	J38.12 E6013
2	Dimension	2.5 × 300mm
3	Polarity	AC. DC
4	Current	50 – 90 (A)
5	Net weight	2.5g

3.4 Proportions of Concrete Mix

The first stage of the experimental work in this study was to make several experimental mixtures of high-strength concrete to reach a compressive strength of C80, by using silica fume to ensure high strength. Superplasticizer was also used to compensate for the low water content in the experimental mixtures. A 12 mm aggregate size was also used. Reverse osmosis (RO) water was also used in mixing and processing, where several mixtures were made in different proportions, and Table 3.13 shows these mixtures, where mixture (C) was adopted in our study to achieve the highest compressive strength.

As for normal-strength concrete, one mixture was adopted to achieve a compressive strength of C25, as shown in Table 3.14.

Table 3.13 Proportions of High Strength Concrete (Trail Mix).

	Materials	Amount(kg/m ³)				Note
		Trail A	Trail B	Trail C	Trail D	
1	Cement	500	550	550	600	Portland
2	Water(%)	150 (27%)	130 (21%)	127 (20%)	132 (20%)	RO
3	Gravel	1100	1000	1000	1000	Size (12)mm
4	Sand	600	750	800	800	sieved
5	Silica Fume	60	60	80	60	-
6	(Superplasticizer) %(C+S)	7.5 (1.35%)	11 (1.8%)	12.6 (2%)	13.2 (2%)	-
7	F_{cu} (MPa)	66	74.6	83.7	77.1	(28 days)

Table 3.14 Proportions of Normal Strength Concrete.

Target concrete strength (MPa) in 28 days	Amount(kg/m ³)			
	Cement	Sand	Gravel	W/C(%)
C25	400	656	1064	212(53%)

3.5 Mixing Methods

3.5.1 Normal Strength Concrete (NSC)

An electric mixer (mixer 1) available in the laboratory of the civil engineering department was used for producing normal strength concrete, as shown in Fig.3.12. The mixing process started by adding coarse aggregate, then sand was added to mix them well for three minutes. After that, cement was added and mixed for an additional three minutes. The mixing water was added gradually to obtain a homogeneous mixture.



Figure 3.11 Mixer (1) for normal strength concrete.

3.5.2 High Strength Concrete (HSC)

For casting high strength concrete, a horizontal mixer (mixer 2) shown in Fig.3.13 was used. Coarse aggregate of maximum size (10) mm was firstly put in the mixer. Then the fine aggregate of (1.18) mm was added and mixed with the coarse aggregate for three minutes.

After that, silica fume and cement were mixed with the aggregate for other three minutes, after which the ingredients became homogenous. Then the superplasticizer was mixed with water and added gradually to the homogeneous materials. Then, it was waited for more than twenty minutes to obtain a homogeneous mixture with suitable operation.



Figure 3.12 Mixer (2) for high strength concrete.

3.6 Concrete Testing

To ensure the quality of the concrete mixture and to know its fresh and hardened properties, many samples were taken during the casting of the main specimens to conduct necessary tests, such as workability, compression, tension, and flexural tests.

3.6.1 Workability test

The workability of the concrete mixes used in this study was tested utilizing slump test for both (NSC) and (HSC) as shown in the Fig 3.14. The test was confirmed to ASTM C-143 [70]. Table 3.15, shows the results of slump test for each mixture.

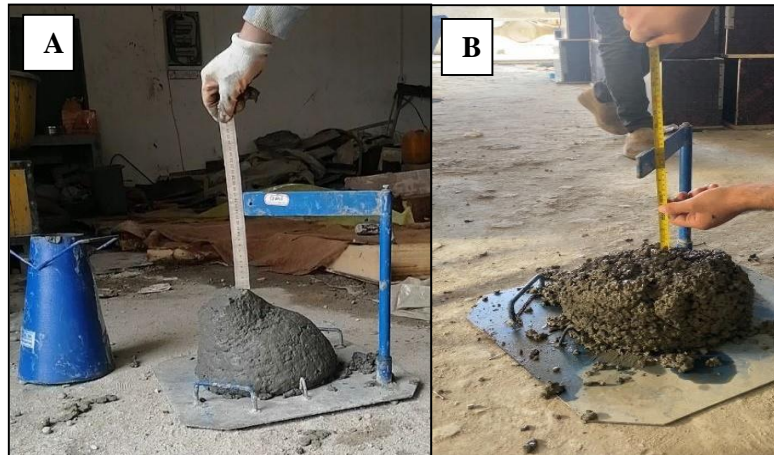


Figure 3.13 Slump test for (A)HSC, (B)NSC.

Table 3.15 Slump test results [70].

	Type of concrete	Slump value (mm)	ASTM C-143 Limitations (mm)	Workability description
1	HSC	135	100 - 150	High
2	NSC	205	≥ 200	Without vibration

3.6.2 Compressive strength

Six cubes were taken for each concrete mix used in this study, with dimensions of (150×150×150) mm, during the process of casting the main specimens as shown in Fig.3.15. After twenty-four hours, the cubes were opened and placed inside the basin filled with reverse osmosis water for curing in preparation for testing them. According to the ASTM C31/C31M-21a standards [71], three cubes for each type of concrete mix were tested at the age of 7 days, and the remaining cubes were tested at the age of 28 days. A compression testing machine of capacity of 2000 kN was used, as shown in Fig.3.16. The results of the test are shown in Table 3.16.



Figure 3.14 Sampling and curing of concrete specimens.



Figure 3.15 Compressive strength test.

Table 3.16 Compressive strength test results.

No.	Concrete type	cube symbol	Density (kg/m ³)	Compressive Strength (MPa)			
				7 days	Average at 7 Days	28 days	Average at 28 Days
1	HSC	A	2467.26	65.1	66.40	85.3	87.83
		B		67.7		94.7	
		C		66.4		83.5	
2	NSC	A	2333.33	17.3	17.23	23.7	25.10
		B		16.6		25.7	
		C		17.8		25.9	

3.6.3 Tensile Strength

The tensile strength of the types of concrete mixtures used was calculated by testing the splitting on cylinders with dimensions of (150×300) mm for normal strength concrete and cylinder with dimension of (100×200) mm for high strength concrete and at ages of 7 and 28 days according to the ASTM C496-17

specification [72] as shown in Table 3.17. The cylinders were placed horizontally inside the testing machine, where the same compression machine was used, and then the load was applied gradually until the cylinder split into two parts, see Fig.3.17. The tensile strength was calculated using Eq. 3.1.

$$f_t = \frac{2P}{\pi LD} \quad 3.1$$

where:

f_t = tensile strength (MPa)

P = the maximum force (N) applied to the specimen

L = the specimen's length (mm)

D = the specimen's diameter (mm)

Table 3.17 Splitting test results.

No.	Concrete type	cylinder symbol	Splitting tensile strength (MPa)			
			7 days	Average at 7 Days	28 days	Average at 28 Days
1	HSC	A	3.12	2.76	7.25	8.02
		B	2.40		8.50	
		C	2.75		8.30	
2	NSC	A	1.20	1.21	2.20	2.15
		B	1.28		2.22	
		C	1.16		2.02	



Figure 3.16 Splitting tensile strength test for (A)HSC, (B)NSC.

3.6.4 Flexural Strength

Prisms of (100×100×500) mm were tested for both types of concrete. The specifications ASTM C78-02 [73], was used to predict the flexural strength of concrete as shown in Fig 3.18. Three prisms were tested at 7 and 28 days for each type. The results were as shown in Table 3.18.

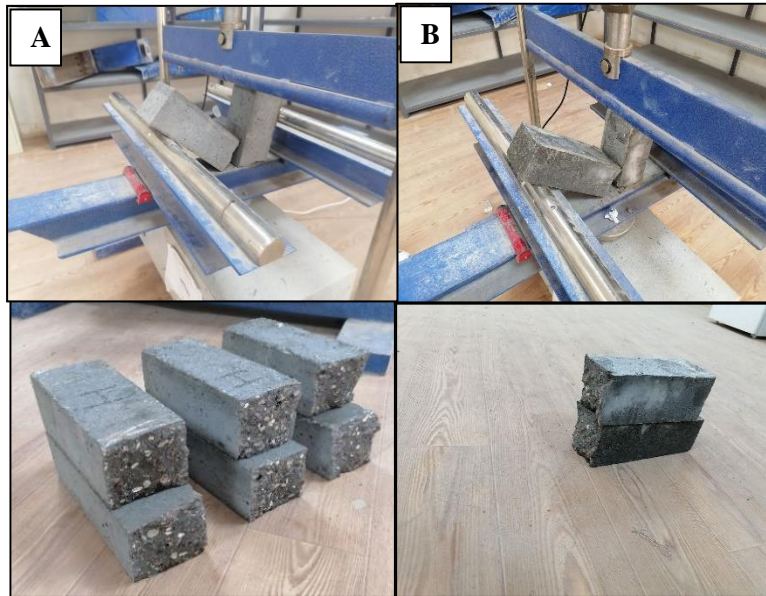


Figure 3.17 Flexural strength test for (A)HSC, (B)NSC.

Table 3.18 Rupture test results.

No.	Concrete type	Prism symbol	Rupture strength (MPa)			
			7 days	Average at 7 Days	28 days	Average at 28 Days
1	HSC	A	3.12	2.76	13.9	14.03
		B	2.4		14.5	
		C	2.75		13.7	
2	NSC	A	1.2	1.21	3.2	3.43
		B	1.28		3.7	
		C	1.16		3.4	

3.6.5 Modulus of Elasticity (E_c):

A cylinder with dimensions of (150×300) mm was tested for each type of concrete with the same compression device used in the compression test, as shown in Fig.3.19. ASTM C469-14[74] test is used to measure the modulus of elasticity of concrete by gradually loading a cylindrical specimen and measuring the

longitudinal strain to determine the stress-strain relationship. The attached Table 3.19 shows the test results.



Figure 3.18 Modulus of Elasticity test.

Table 3.19 Modulus of Elasticity test results.

No.	Concrete type	Density (kg/m ³)	Modulus of Elasticity results (MPa)
1	HSC	2425.1	43076.21
2	NSC	2382.2	23025.2

3.7 Preparation of Test Specimens

In this study, all the work was done in the laboratories of the College of Engineering at Misan University.

Three types of wood were used to make the formwork, see Fig 3.20. Plywood was used in the formwork base, while 20 mm-thick wood was used for the sides. The formwork parts were connected using screws for woodwork. The formwork had dimensions of (1200×500×150) mm for all formwork. The third type was a wooden plate used during the casting process to temporarily separate the two types of concrete. It was removed immediately after casting the two types of concrete. It was also coated with oil to prevent concrete from sticking to it and to prevent the absorption of water from the concrete mixtures.



Figure 3.19 Formwork Details.

In the reinforcement of the deep beams, four different diameters of reinforcing steel bars were employed: $\varnothing 16$ mm, $\varnothing 12$ mm, $\varnothing 8$ mm, and $\varnothing 4$ mm. The strut was reinforced in two configurations, arched and triangular, using $4\varnothing 8$ mm bars for longitudinal reinforcement and $\varnothing 4$ mm stirrups spaced at 75 mm.

As for the tie, it was reinforced with a combination of $2\varnothing 16$ mm and $2\varnothing 12$ mm bars, as illustrated in the corresponding Fig.3.21.



Figure 3.20 Reinforcement Details.

For the specimens reinforced with angle steel sections measuring $40 \times 40 \times 4$ mm, the sections were connected together using a steel plate of 30×4 mm to function as a single integrated unit. The connection was achieved through fillet welding, which was performed with precision to avoid overheating and prevent melting or

distortion of the steel components. This welding technique was chosen to ensure the mechanical strength and structural integrity of the joint. The configuration and welding details are illustrated in Figure 3.22.



Figure 3.21 Welding process.

After the formworks were oiled and labeled, the reinforcement bars and steel sections were carefully positioned inside the formworks in preparation for the casting process, as shown in the attached Fig.3.23.



Figure 3.22 Preparing specimens for casting process.

The casting of the specimens was conducted using approved concrete mix proportions. Both high-strength concrete (HSC) and normal-strength concrete (NSC) were cast simultaneously to ensure proper integration and to prevent segregation between the two types, as illustrated in Figure 3.24.



Figure 3.23 Casting process procedure.

To facilitate the blending of the two concrete types, the separating plate initially placed between them inside the formwork was removed after placement and vibration, allowing for uniform consolidation. The setup and process are further shown in Figure 3.25. After the casting process was completed, the outer surfaces of the concrete were manually finished using a hand trowel to achieve a smooth and uniform surface, see Fig 3.26.

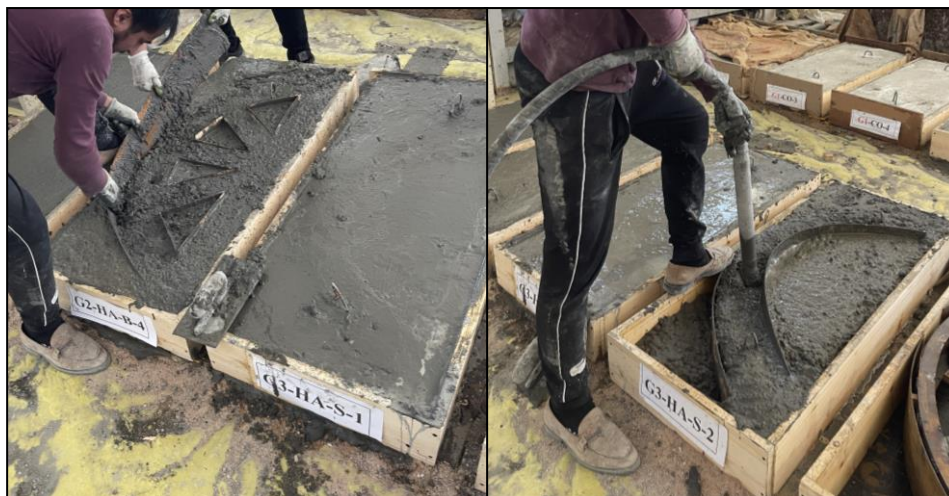


Figure 3.24 Separating plate lifting and vibrator use.



Figure 3.25 Finishing process.

3.7.1 Curing the Specimens.

After the casting process was completed and after twenty-four hours, the curing process began. Reverse osmosis (RO) water was used, and the specimens were covered with thick burlap bags to retain moisture for as long as possible to obtain the desired concrete strength, see Fig 3.27.



Figure 3.26 Curing process.

3.8 Instrumentation and Equipment of the Test

3.8.1 Flexural Test Machine

All specimens were tested using a flexural testing machine with a load capacity of 600 kN, as shown in Fig 3.28. The machine is automated to apply the load at a specified rate, with the ability to control and adjust the loading rate as required.



Figure 3.27 Flexural Test Machine.

3.8.2 Data Logger

A laptop computer and the GEODATALOG 30-WF6016 data logger, which gathers data from many strain gauges on the deep beam, make up the data collection system. Multiple sensors may be measured simultaneously due to its 16 channels. It runs on a single-phase power supply with a voltage range of 110-240 V and 50-60 Hz. As shown in Fig.3.29, the system comes with DATACOMM software for effective data gathering, monitoring, and analysis.

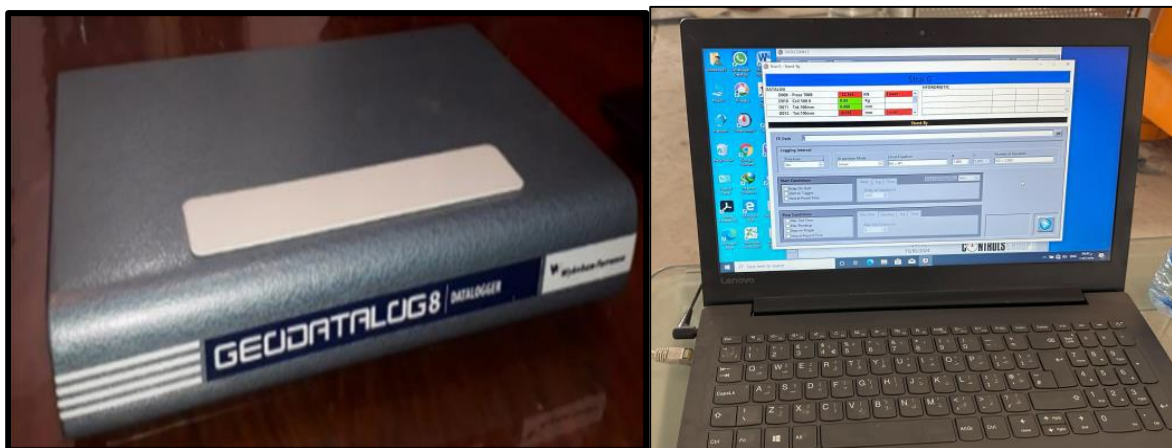


Figure 3.28 Data logger.

3.8.3 Strain Gauges

Several Types of PFL-30-11-3LJC-F Tokyo concrete strain gauges, measuring 30 mm in length, were attached to the face of the reinforced concrete deep beams. The strain gauges and the glue used to install them are shown in Fig.3.30.



Figure 3.29 Concrete strain gauges and their glue.

3.8.4 Deflection measurement (LVDT)

In testing all the specimens, a linear variable differential transformers (LVDT) was used to measure the deflection at the mid-span of the deep beams in order to draw the relationship between the load and deflection to know the stiffness and other properties of the different beams, see Fig 3.31.



Figure 3.30 Linear variable differential transformers (LVDT).

3.9 Testing Procedure

After 28 days of casting the specimens and the end of the curing period, the specimens were painted with two colors: white for the beams in general and gray for the struts and ties in order to facilitate the vision of the micro-cracks and to distinguish the type of failure that occurs to the struts and ties as shown in the Fig 3.32. After that, the places where the strain gauges were attached were smoothed and cleaned to ensure complete adhesion for accurate strain readings.



Figure 3.31 painting specimens.

After completing the painting and preparation of the specimens, the flexural testing machine was adjusted to accommodate the dimensions of the beams, maintaining a constant shear span-to-depth ratio (a/d) of 1. The distance between the centers of the supports was fixed at 1 meter, and the load was applied at the mid-span of the beam, exactly 0.5 m from each support. All specimens were subjected to a single-point load applied at the center of the span. To ensure uniform load distribution and to minimize stress concentrations during the testing process, rubber pads were placed both beneath and above the specimens, as shown in Figure 3.33.



Figure 3.32 rubber pads locations.

To ensure a streamlined test and to study the development of cracks within the concrete, the load was applied incrementally in steps of 5 kN. The cracks were marked, and their progression was tracked using a whiteboard pen, as shown in the attached Fig.3.34.

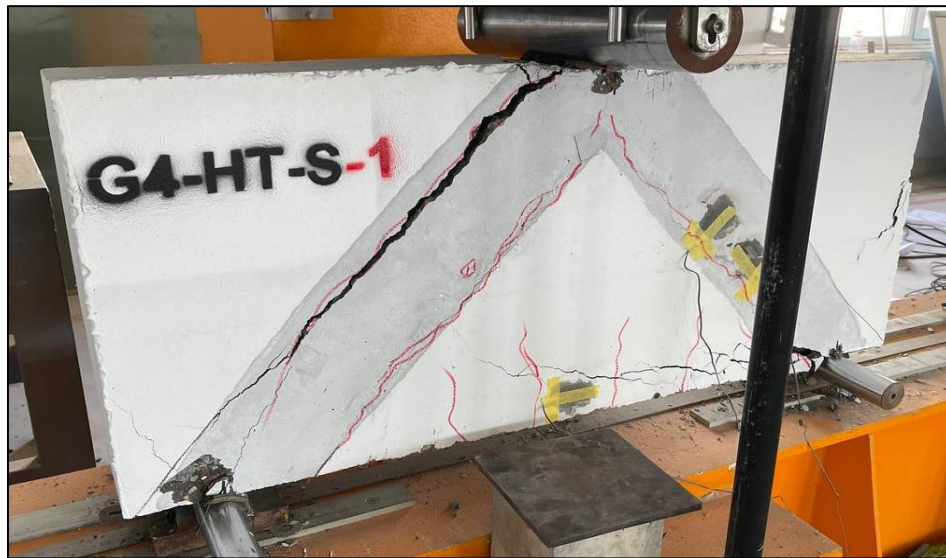


Figure 3.33 Marking cracks in the tested beams

A linear variable differential transformer (LVDT) was placed in the middle of the specimens to measure the deflection throughout the loading period, and the strain gauges were connected to the data logger to calculate the strains on the side concrete with each loading step to study the behavior of the concrete throughout the testing period until the failure of the specimens was reached.

The testing machine was set up as shown in Fig.3.34, and all specimens were tested under identical conditions, including the same shear span-to-depth ratio (a/d) and loading method, to ensure consistent and reliable results.

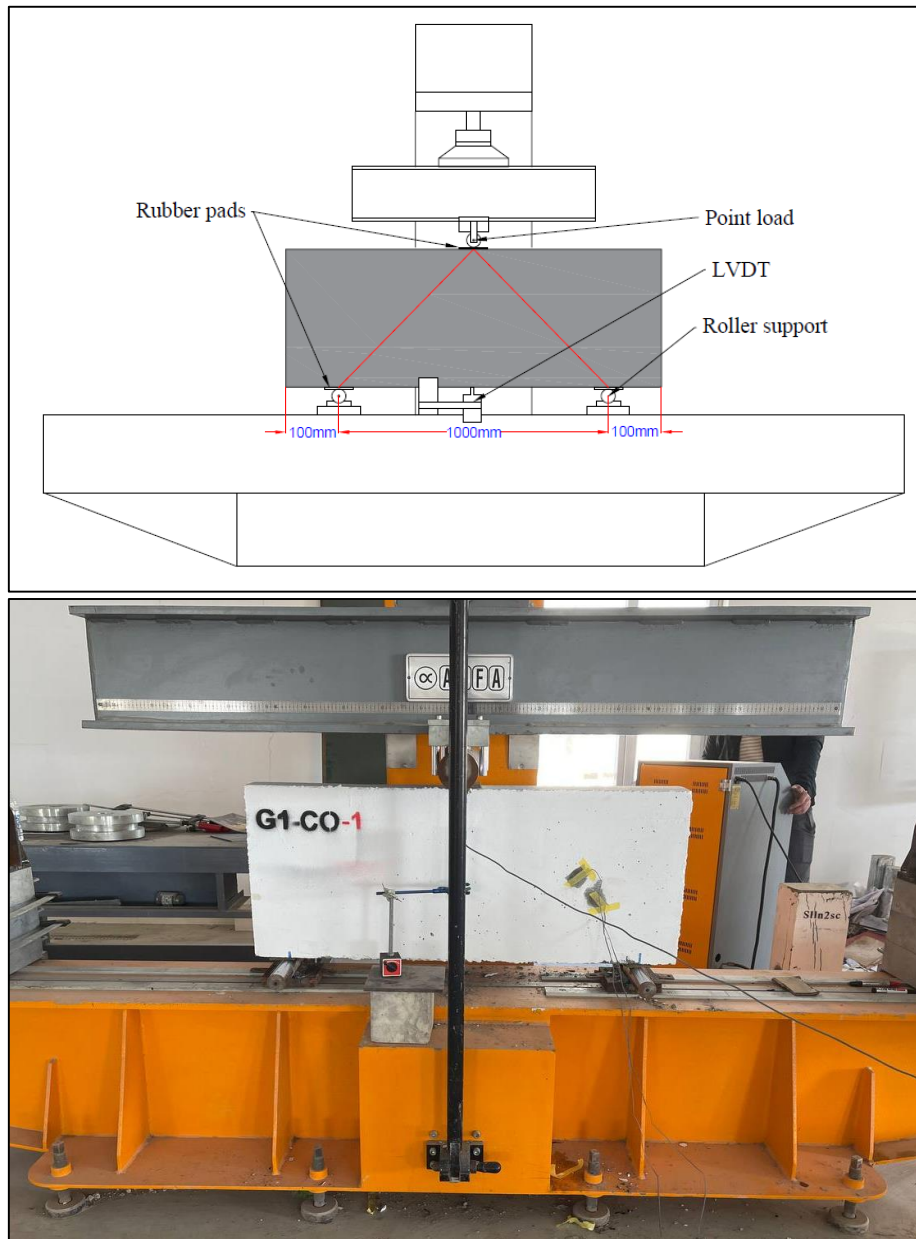


Figure 3.34 Test setting

CHAPTER FOUR: RESULTS AND DISCUSSION

4.1 General

This chapter provides a comprehensive presentation and analysis of the experimental results obtained from testing fifteen reinforced concrete deep beams, each subjected to a single-point load applied at the mid-span. The primary objective of this investigation is to examine the structural behavior of hybrid concrete beams and compare their performance with that of conventional beams made entirely of either normal-strength concrete (NSC) or high-strength concrete (HSC). The hybrid beams were constructed using strategic combinations of NSC and HSC arranged in specific configurations, namely arch and triangle hybridizations, to evaluate the influence of concrete distribution on beam behavior. Key structural parameters were recorded and analyzed, including the first cracking load, ultimate failure load, load-deflection response, stiffness, toughness, ductility, and modes of failure. These parameters offer critical insights into the mechanical performance and resilience of the tested specimens under concentrated loading. In addition to the concrete configuration, the type of reinforcement used, whether traditional steel bars or embedded steel sections was varied to assess its impact on the overall behavior and load-carrying capacity of the beams.

By systematically comparing the performance of hybrid beams with that of control specimens composed solely of NSC or HSC, this chapter aims to identify the advantages and potential limitations of hybridization techniques. Furthermore, the study explores how different variables, such as concrete type, hybrid configuration, and reinforcement method, influence structural efficiency and failure mechanisms. The findings contribute valuable knowledge to the design and optimization of deep beams in structural engineering applications, especially where enhanced strength, ductility, and material efficiency are desired.

4.2 Ultimate Load

4.2.1 First group

For the first group (**G1**), the specimens made of normal-strength concrete namely (**G1-CO-1**) and (**G1-CO-2**) exhibited maximum loads of 280 kN and 310 kN, respectively, see Table 4.1. The load capacity of specimen (**G1-CO-2**) was **10.71%** higher than that of (**G1-CO-1**). This increase is likely attributed to the difference in the reinforcement configuration of the strut. Specifically, specimen (**G1-CO-1**) was reinforced using a triangular pattern, while specimen (**G1-CO-2**) employed an arched reinforcement layout. The arch-shaped reinforcement likely contributed to the improved performance of specimen **G1-CO-2**, as arch configurations are structurally more efficient in resisting compressive forces.

Despite this variation in reinforcement, both specimens ultimately failed by the bearing failure. This failure mode can be linked to the limited compressive strength of the normal-strength concrete used in these specimens, which was measured at 25.1 MPa. as shown in Figs.4.1 and 4.2.

The final two specimens in this group (**G1-CO-3**) and (**G1-CO-4**) were cast using high-strength concrete while maintaining the same reinforcement configurations as the earlier specimens. Specimen (**G1-CO-3**), which featured a triangular strut reinforcement, sustained an ultimate load of 390 kN. This represents a 29.28% increase compared to (**G1-CO-1**), which was made with normal-strength concrete. The enhanced load capacity is primarily attributed to the superior compressive strength of the high-strength concrete, measured at 87.83 MPa. Specimen (**G1-CO-4**), reinforced with an arch-shaped strut, achieved an ultimate load of 410 kN, 5.13% higher than (**G1-CO-3**). This increase aligns with the previously observed arch-action benefit, where the curved reinforcement effectively channels compressive forces. When compared to (**G1-CO-2**), which shared the same reinforcement layout but was cast with normal-strength concrete,

the load capacity improved by 32.26%, further emphasizing the positive impact of high-strength concrete on structural performance.

The failure modes of specimens **(G1-CO-3)** and **(G1-CO-4)** were not influenced by the reinforcement geometry but rather by the concrete type. Both specimens experienced a combined diagonal shear and semi-flexural failure, reflecting the more brittle nature of high-strength concrete under load. See Fig 4.3 and 4.4.

Table 4.1 Ultimate Load and Failure Modes for (G1)

Groups No.	No.	Specimens	Cracking load P_{cr} (kN)	Ultimate load P_u (kN)	Failure Modes
G1	1	G1-CO-1	170	280	Bearing Failure
	2	G1-CO-2	180	310	Bearing Failure
	3	G1-CO-3	180	390	Shear-Flexural Failure
	4	G1-CO-4	200	410	Shear- Flexural Failure

4.2.2 Second group (G2)

This group demonstrated a clear and consistent improvement in the load-bearing capacity of the beam models compared to the control specimens from Group G1. The enhanced performance is primarily attributed to targeted strengthening techniques, such as the use of high-strength concrete in critical stress regions (particularly the strut), arch-shaped reinforcement layouts, and the introduction of inclined ribs. The influence of these parameters on the structural behavior is discussed below.

The first specimen in this group, **(G2-HA-B-1)**, achieved an ultimate load of 420 kN, marking a 35.48% increase compared to the control specimen **(G1-CO-2)**, and a 2.44% improvement relative to **(G1-CO-4)**. This significant increase in capacity is largely due to the strategic reinforcement of the strut region using high-strength concrete in an arch configuration. The arch shape contributes to more efficient force transfer by promoting compressive stress paths along the natural load flow, minimizing tensile-induced cracking. Despite its improved performance, the beam ultimately failed due to diagonal shear. The failure initiated along the weakest path in the beam, the interface between the strut edge

and the transition zone between the two types of concrete, highlighting the need for improved continuity or interface treatment in future designs, as in Fig.4.5.

The second specimen, **(G2-HA-B-2)**, further improved upon this behavior by reaching an ultimate load of 430 kN, representing a 38.7% and 4.88% increase compared to **(G1-CO-2)** and **(G1-CO-4)**, respectively. In addition to strut reinforcement, this beam featured enhanced reinforcement in the tie region, which contributed to the formation of a compact and efficient internal arch system. This reinforcement strategy significantly improved the internal force redistribution, resulting in better confinement and an increased capacity to resist applied loads. The failure mode was a combination of diagonal shear and bearing failure. Although the strengthened arch action delayed the progression of failure, the nodal zone ultimately failed before the beam could reach a more brittle collapse mechanism, see Fig.4.6.

The specimen **(G2-HA-B-3)** demonstrated the highest load capacity in this group, reaching an ultimate load of 450 kN. This corresponds to a 45.16% increase over **(G1-CO-2)** and a 9.76% improvement compared to **(G1-CO-4)**. The exceptional performance of this specimen is attributed to the addition of inclined ribs positioned at a 60° angle, which significantly enhanced the effectiveness of the arch action. These ribs improved force continuity and stress flow, reducing the likelihood of premature local failures. The design philosophy behind the rib addition is supported by the findings of Jaafer et al. [75], who demonstrated the importance of inclined reinforcement in enhancing strut-and-tie mechanisms. As observed in the previous specimens, failure occurred through a combined mechanism involving diagonal shear and bearing failure. See Fig.4.7.

The final specimen, **(G2-HA-B-4)**, reached an ultimate load of 440 kN, slightly lower than **(G2-HA-B-3)** by 2.2%, indicating that while the addition of ribs is beneficial, their number and angle must be carefully optimized. Excessive or improperly oriented ribs may interfere with the ideal stress trajectory or introduce

unintended stress concentrations. Nonetheless, this beam still showed a significant improvement 41.9% and 7.32% over (G1-CO-2) and (G1-CO-4), respectively. The failure pattern closely mirrored that of G2-HA-B-3, confirming the consistency of the observed behavior, see Fig.4.8.

Table 4.2 Ultimate Load and Failure Modes for (G2)

Groups No.	No.	Specimens	Cracking load P_{cr} (kN)	Ultimate load P_u (kN)	Failure Modes
G2	1	G2-HA-B-1	160	420	Diagonal-Shear Failure
	2	G2-HA-B-2	240	430	Bearing -Diagonal Shear Failure
	3	G2-HA-B-3	210	450	Bearing -Diagonal Shear Failure
	4	G2-HA-B-4	230	440	Bearing -Diagonal Shear Failure

A common failure pattern was observed across (G2-HA-B-2), (G2-HA-B-3), and (G2-HA-B-4), wherein failure occurred due to the collapse of the nodule zone, following a partial development of diagonal shear cracks. This failure behavior can be directly linked to the reinforcement strategy adopted in these models. By modifying the reinforcement details in the tie region and incorporating high-strength concrete, a robust arch base was established. This structural configuration restricted the full development of diagonal shear cracks, redirecting the failure mechanism to the nodule zone, which remained the weakest part of the system.

These findings underscore the effectiveness of combining strategic reinforcement detailing with high-performance materials. The results, summarized in Table 4.2, demonstrate that each design modification contributed to progressive improvements in structural capacity, with the highest gains observed when multiple strategies were employed simultaneously.

4.2.3 Third group (G3)

The third group of specimens displayed distinct structural behavior in terms of load-bearing capacity when compared to the control and other hybridized

groups. This variation highlights the influence of both the structural configuration and the type of reinforcement used.

For the first beam in this group (**G3-HA-S-1**), the ultimate load recorded was 420 kN. This represents a significant increase of 35.48% compared to the control specimen (**G1-CO-2**) and a modest improvement of 2.44% relative to another control specimen (**G1-CO-4**). Notably, this value matches the maximum load achieved by the specimen (**G2-HA-B-1**), despite the clear difference in reinforcement type between the two beams. This finding suggests that the enhancement in load-bearing capacity is primarily attributed to the arched structural action provided by the geometry of the beam and the strength of the concrete. However, the variation in reinforcement type notably influenced the failure mode. In the case of (**G3-HA-S-1**), the strength imparted by the arched action and the integration of angle steel sections prevented the development of diagonal shear cracks. Consequently, the beam failed through the collapse of the nodal zone, contrasting with (**G2-HA-B-1**), which experienced failure due to diagonal shear. See Fig 4.9.

The second specimen in this group (**G3-HA-S-2**) exhibited the lowest load-bearing capacity among the three, reaching a maximum load of 370 kN. Although this value still marks a 23.3% increase over the control specimen (**G1-CO-2**), it is 9.76% and 11.9% lower than the loads sustained by (**G1-CO-4**) and (**G3-HA-S-1**), respectively. This beam ultimately failed due to pronounced diagonal shear, a result attributed to inadequate reinforcement in the strut region. Specifically, reinforcement was provided and enhanced on only one side of the strut, leaving the opposite (inner) side significantly weaker. This asymmetry facilitated the development of a large crack through the unreinforced zone, which progressed into a diagonal shear failure. These results emphasize the critical importance of balanced and comprehensive reinforcement detailing. It becomes evident that

hybridization alone—without proper reinforcement design is insufficient to significantly improve load capacity or prevent premature failure. See Fig 4.10.

The third beam (**G3-HA-S-3**) demonstrated the most remarkable performance among all specimens tested. It achieved a maximum load of 540 kN, representing an improvement of 80% and 31.7% over the control specimens (**G1-CO-2**) and (**G1-CO-4**), respectively. Compared to its counterparts within the same group, it outperformed (**G3-HA-S-1**) by 28.57% and (**G3-HA-S-2**) by 45.96%. The substantial improvement in load-bearing capacity can be attributed to the incorporation of two 45-degree angle steel sections ribs, which effectively formed a robust arched structural frame. This configuration facilitated a more uniform redistribution of internal stresses, preventing localized failure zones and enhancing the overall stability of the structure. As a result, the beam exhibited diagonal shear cracks on both sides of the strut region. Additionally, yielding of the reinforcing steel in the tie region was observed, indicating a complex failure mode characterized by a combination of diagonal shear and semi-flexural behavior. See Fig 4.11.

Overall, the results from this group underscore the critical role of structural geometry, reinforcement configuration, and material interaction in defining the load-carrying behavior and failure modes of hybridized concrete beams. A carefully engineered combination of arched action and strategic reinforcement placement can lead to significant enhancements in structural performance. Table 4.3 shows the ultimate load results for this group.

Table 4.3 Ultimate Load and Failure Modes for (G3)

Groups No.	No.	Specimens	Cracking load P_{cr} (kN)	Ultimate load P_u (kN)	Failure Modes
G3	1	G3-HA-S-1	150	420	Bearing -Shear Failure
	2	G3-HA-S-2	180	370	Diagonal-shear failure
	3	G3-HA-S-3	200	540	Shear- Flexural Failure

4.2.4 Fourth group (G4)

The fourth and final group of specimens was designed with hybrid concrete cast in a triangular configuration as recommended by the ACI 318M-19 [9]. The struts in these specimens were reinforced using angled steel sections to enhance structural integrity. All specimens within this group demonstrated similar structural behavior and exhibited a consistent failure pattern, with diagonal shear being the predominant mode of failure across the board.

Specimen (**G4-HT-S-1**) achieved an ultimate load of 490 kN, indicating a substantial improvement in load-bearing capacity. This represents a 75% increase compared to control specimen (**G1-CO-1**) and a 19.5% increase relative to control specimen (**G1-CO-3**). This enhancement is attributed to the well-confined strut region, where four angled steel sections were used to reinforce the concrete. These sections were tightly secured, effectively restraining the compressive stresses within the strut and delaying the onset of failure. This confinement contributed significantly to the specimen's ability to carry higher loads prior to experiencing diagonal shear failure. See Fig.4.12.

Similarly, specimen (**G4-HT-S-2**) exhibited a strong performance, reaching an ultimate load of 460 kN. This value is 64.28% higher than (**G1-CO-1**) and 17.95% higher than (**G1-CO-3**). Although this specimen shared the same triangular concrete configuration and strut reinforcement design as (**G4-HT-S-1**), a notable variation was the replacement of part of the traditional steel bar reinforcement in the tie region with angled steel sections. While this substitution did not alter the mode of failure, which remained diagonal shear, it did influence other structural behaviors, such as stiffness and crack distribution, which will be discussed in detail later in this chapter. See Fig 4.13.

Specimen (**G4-HT-S-3**) recorded an ultimate load of 430 kN, reflecting a 53.57% and 10.25% improvement over control specimens (**G1-CO-1**) and (**G1-CO-3**), respectively. While the strut reinforcement details were similar to (**G4-**

HT-S-4) (discussed below), this specimen benefited from an additional reinforcement measure: the angled steel sections used in the strut region were connected at mid-span. This added continuity provided extra support and helped to distribute the compressive forces more effectively across the strut, thereby enhancing the beam's capacity before failure. See Fig.4.14.

Among all specimens in Group 4, **(G4-HT-S-4)** exhibited the lowest ultimate load capacity, reaching 340 kN. While this load still represents a 21.43% increase compared to the control specimen **(G1-CO-1)**, it is 12.82% lower than the capacity recorded for **(G1-CO-3)**. The reduced performance is primarily due to insufficient reinforcement in the strut region. Specifically, only one side of the strut was reinforced, while the inner side was left unreinforced. This asymmetry in reinforcement led to the formation of cracks within the strut, ultimately resulting in failure due to diagonal shear. The absence of reinforcement continuity severely compromised the structural integrity of the beam under increasing loads. See Fig.4.15.

The results from Group 4 underscore the effectiveness of triangular hybrid concrete configurations when combined with well-distributed angled steel reinforcement. The specimens that utilized complete or mid-span-connected strut reinforcements consistently outperformed those with incomplete or asymmetrical reinforcement.

Furthermore, the data indicate that while alternative reinforcement strategies such as substituting conventional tie reinforcement with angled steel can be viable, they must be applied with careful consideration of the global reinforcement layout to avoid compromising structural performance. Ultimately, achieving optimal load-bearing capacity requires not only innovative hybridization techniques but also meticulous attention to reinforcement detailing and placement. See Table 4.4.

Table 4.4 Ultimate Load and Failure Modes for (G4)

Groups No.	No.	Specimens	Cracking load P_{cr} (kN)	Ultimate load P_u (kN)	Failure Modes
G4	1	G4-HT-S-1	150	490	Diagonal-Shear Failure
	2	G4-HT-S-2	145	460	Diagonal-Shear Failure
	3	G4-HT-S-3	140	430	Diagonal-Shear Failure
	4	G4-HT-S-4	140	340	Diagonal-Shear Failure

4.3 Load - Deflection Curves

The behavior of each specimen can be distinctly categorized into three primary phases, as illustrated in Figures 4.16 to 4.19, which is characteristic of reinforced concrete beams subjected to a single-point load.

A. Elastic Region (Initial Linear Portion)

In the first segment of the curves, all specimens exhibit linear elastic behavior. This region is characterized by a direct proportionality between applied load and deflection, governed primarily by the material stiffness and section geometry. All beams demonstrated different slopes in this segment, indicating variations in stiffness due to their individual reinforcement schemes and configurations.

B. Yielding and Crack Propagation Phase

Following the elastic region, the second portion of the curves marks the initiation of first cracks and the onset of steel reinforcement yielding. In this phase, the slope of the curve decreases, and deflection increases at a faster rate for a given load. This nonlinear response is governed by the redistribution of stresses after concrete cracking and the progressive engagement of reinforcement. Variations in the curves in this phase are primarily influenced by reinforcement detailing, such as the presence or absence of stirrups, replacement of ties with steel angles, or additional strut-to-strut connections. The load-deformation increments in this region are less uniform and reflect the evolving internal damage and stress redistribution within each specimen. This stage is typically very short in deep beams, unlike in conventional beams.

C. Plastic Region

The third and final segment of the load-deflection curve corresponds to the plastic behavior of the specimens. At this stage, the beams approach their ultimate load-carrying capacity. Load transmission is increasingly governed by the strut-and-tie mechanism, which is characteristic of deep beam behavior. During this phase, a noticeable increase in deflection occurs with only a small increase in the applied load, and the stiffness continues to degrade progressively.

4.3.1 Control Beam Specimens (G1)

The load–deflection curves for the **G1** control specimens, as shown in Fig 4.16, illustrate the influence of both concrete strength and strut reinforcement geometry on structural performance. Beam **G1-CO-1**, which incorporated a triangular strut and normal-strength concrete, exhibited the lowest stiffness and the greatest deflection reaching to 9.2 mm. This behavior is attributed to early cracking and limited load-carrying capacity, which results in a rapid transition from elastic to plastic behavior. In contrast, Beam **G1-CO-2**, also constructed with normal-strength concrete but utilizing an arched strut, demonstrated significantly improved stiffness and reduced deflection of 6.552 mm. The enhanced performance is primarily due to the arch action, which more effectively resists compressive stresses.

Specimens (**G1-CO-3**) and (**G1-CO-4**), both constructed with high-strength concrete, exhibited increased stiffness and load capacity. Beam (**G1-CO-3**), reinforced with a triangular strut, had a deflection of 7.45 mm, while Beam (**G1-CO-4**), with an arched strut, showed a slightly lower deflection of 7.23 mm. The superior performance of (**G1-CO-4**) marked by higher stiffness, delayed cracking, and reduced deflection highlights the advantage of combining high-strength concrete with arched reinforcement geometry.

Overall, the findings confirm that both strut design and concrete strength significantly enhance the load–deflection behavior of deep beams.

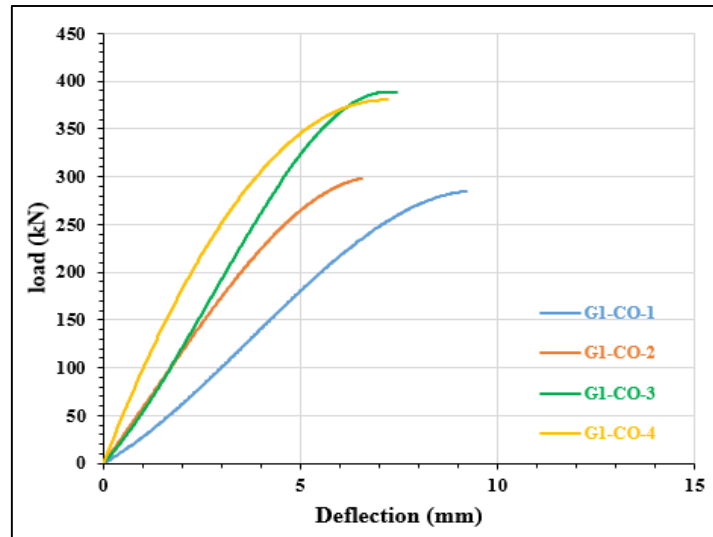


Figure 4.1. Load - Deflection Curves for specimens of control beams.

4.3.2 Hybrid Beams – Arch Strut Specimens

4.3.2.1 Reinforced Specimens with Steel Bars

Based on the load-deflection curve presented in Fig 4.17, it is observed that the beams in this group exhibit similar behavior during the initial (linear elastic) stage. However, with the onset of the second stage, noticeable differences emerge in terms of load-bearing capacity, deflection, and stiffness among the beams. The greatest deflection in this group was recorded for beam **G2-HA-B-4**, reaching 7.11 mm, while the smallest deflection 5.88 mm was observed in beam **G2-HA-B-2**. This reduced deflection can be attributed to the use of high-strength concrete in the tie region, as well as the different reinforcement configuration compared to beam **G2-HA-B-1**. Although beams **G2-HA-B-3** and **G2-HA-B-4** share similar hybridization and reinforcement in the tie zone, they exhibited higher deflection values 6.22 mm and 7.11 mm, respectively than beam **G2-HA-B-2**. This behavior may be due to the addition of ribs, which likely transferred part of the compressive force toward the center of the tie, resulting in increased deflection. When compared to the control specimens (**G1-CO-2**) and (**G1-CO-4**) from the first group, all of these specimens share a common characteristic: arched reinforcement in the strut region of the control samples.

The first beam (**G2-HA-B-1**) demonstrated a higher load-carrying capacity. With a deflection of 6.836 mm, it exhibited less deflection than control beams **G1-CO-2** and **G1-CO-4**. The load-deflection curve shows greater stiffness than that of control beam **G1-CO-2**. However, its stiffness was lower than that of **G1-CO-4** during the initial linear stage, possibly due to differences in the types of concrete used, as each material behaves differently based on its mechanical properties. Additionally, the early appearance of the first crack may have contributed to internal stress redistribution within the beam. Despite this early reduction in stiffness, the load increased significantly, particularly during the middle of the yielding stage. Beam **G2-HA-B-1** exhibited a notable increase in stiffness up to failure, underscoring the effectiveness of the strut-arch hybridization in sustaining load until the failure stage.

Initially, the second beam (**G2-HA-B-2**) displayed stiffness comparable to that of control beam **G1-CO-4**. However, in subsequent stages, it demonstrated greater stiffness than both the control specimens and beam **G2-HA-B-1**, continuing up to failure. This improvement is attributed to modifications in the reinforcement technique of the tie region, including the addition of stirrups and the use of high-strength concrete. With a deflection of only 5.88 mm, this beam recorded the lowest deflection in this group and among all tested specimens. Furthermore, the first visible crack was delayed until a load of 240 kN, providing further evidence of the effectiveness of the hybrid reinforcement approach.

Among the group, beam (**G2-HA-B-3**) showed the greatest initial stiffness, probably because two high-strength concrete ribs reinforced the strut arch, therefore improving the load-carrying capacity of the arch. Its stiffness dropped after the first crack to lower than (**G2-HA-B-1**) but still higher than the other specimens, and it stayed at that level until failure. At 450 kN, this beam had the greatest load capacity in the group, probably due to the extra ribs, which improved stress distribution and structural integrity until failure. Reaching 6.22 mm, its deflection was also lower than that of the control specimens.

At about 70% of the failure load, the fourth beam, (**G2-HA-B-4**), eventually exhibited stiffness performance comparable to (**G2-HA-B-1**). Beyond this point, it exceeded (**G2-HA-B-1**) in stiffness until the failure stage. The strengthening method more precisely, the rib addition to the strut arch accounts for this advancement.

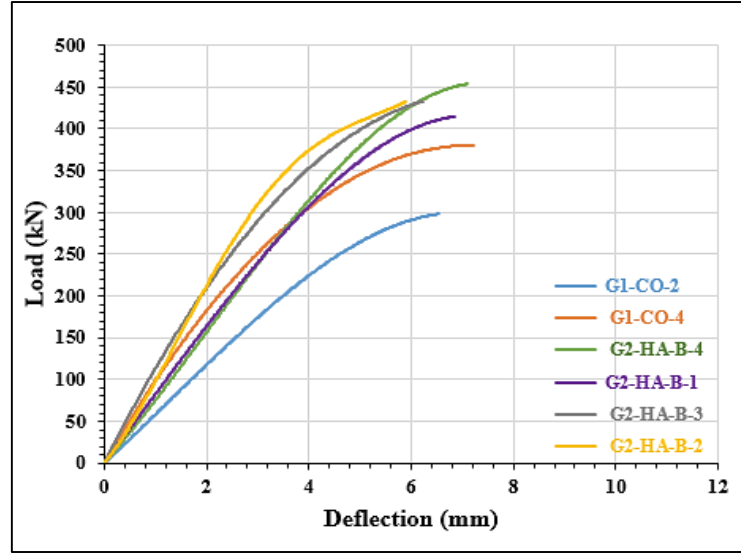


Figure 4.2 Load - Deflection Curves for the second group specimens (G2).

4.3.2.2 Reinforced Specimens with Steel Section

The load-deflection behavior for this group is shown in Fig.4.18, highlighting the performance of beams strengthened using an innovative method with angled steel sections in the strut region or the arch form.

In this group, the third beam **G3-HA-S-3** exhibited the best overall performance in terms of first crack load, deflection, and load-carrying capacity, with a recorded deflection of 6.868 mm. In comparison, the first beam **G3-HA-S-1** showed a slightly lower deflection of 6.73 mm but exhibited reduced stiffness, load capacity, and first crack load relative to **G3-HA-S-3**. The second beam **G3-HA-S-2** recorded the highest deflection in the group at 8.283 mm and demonstrated significantly lower load capacity and stiffness than the other two beams. This reduction in performance may be attributed to the decreased steel reinforcement in the strut region.

The first beam (**G3-HA-S-1**), showed better stiffness than the control specimens (**G1-CO-2**) and (**G1-CO-4**). Its response in the first loading stage closely mirrored that of (**G1-CO-4**), but it always stayed higher all the way to the failure stage, suggesting the efficacy of the applied reinforcement method. Though lower than (**G1-CO-4**), this beam showed a deflection of 6.73 mm, more than that of (**G1-CO-2**).

Consistent with the lower strut region reinforcement, the second beam (**G3-HA-S-2**), showed less total stiffness than the control specimens. Effective stress redistribution inside the beam allowed it to maintain a fairly high stiffness and load capacity up to the pre-failure stage, but Notwithstanding this, it showed the most group deflection at 8.283 mm, suggesting more deformation under load application. Among all specimens, the last beam in this group (**G3-HA-S-3**), showed a unique performance with the greatest load capacity and significant stiffness. The first crack's appearance was also postponed, indicating better crack resistance. The addition of two ribs made of angled steel sections accounts for this improved behavior; when combined with high-strength concrete, these ribs probably offered more compressive resistance in the strut area during loading. Deflection-wise, it measured a fair value compared to the control specimens at 6.868 mm, indicating a balanced response between strength and ductility.

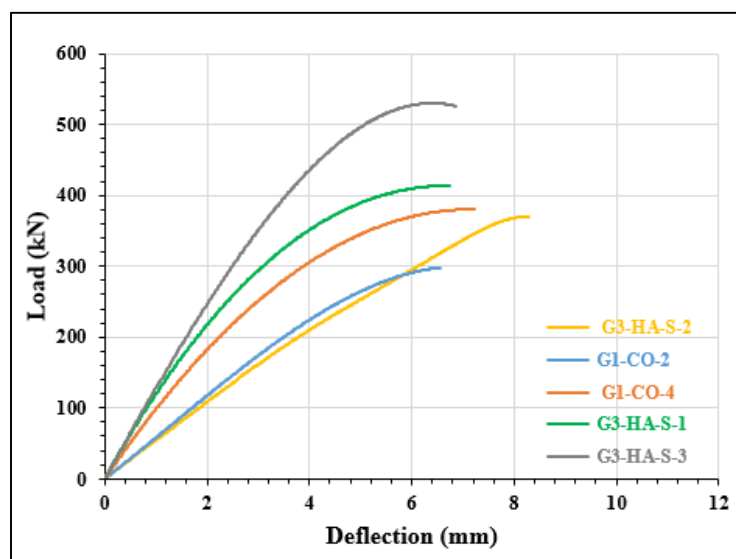


Figure 4.3 Load - Deflection Curves for third group specimens (G3).

4.3.3 Hybrid Beams – Triangle Strut Specimens

The load-deflection behavior for this group (**G4**), as shown in Fig. 4.19, indicates that the first three beams exhibited improvements in both stiffness and load-carrying capacity. However, none of the beams showed an enhancement in the first crack load.

Beams **G4-HT-S-1** and **G4-HT-S-3** displayed similar deflection values, while the highest deflection was recorded for beam **G4-HT-S-2** at 8.03 mm. In contrast, the lowest deflection was observed in beam **G4-HT-S-4**, which recorded a deflection of 5.48 mm, as it failed under loading earlier than the other three beams. Excluding the final beam (**G4-HT-S-4**), the fourth and final group (**G4**), characterized by triangular hybrid reinforcement in the strut region, demonstrated a significant increase in both stiffness and load-bearing capacity compared to the control specimens (**G1-CO-1**) and (**G1-CO-3**).

Outperforming both control specimens across the whole loading process up to failure, the first beam, (**G4-HT-S-1**), showed the most notable increase in stiffness and load capacity. It also noted the least deflection value among all beams in this group reaching 6.612 mm. The tightly confined and properly arranged angle steel sections inside the strut region most likely account for this better performance since they provided strong confinement and improved load transfer, therefore raising the resistance.

Although its performance remained lower than that of beam **G4-HT-S-1**, the second beam, **G4-HT-S-2**, showed a noticeable improvement compared to the control specimens. The load-deflection curve indicates a higher deflection of 8.03 mm, along with a reduction in stiffness and load-carrying capacity. This suggests increased yielding and deformation under load, likely due to the partial replacement of tie reinforcement with angle steel sections, which may have affected the overall confinement and load distribution within the beam.

Beam **G4-HT-S-3** showed comparable initial stiffness to (**G4-HT-S-2**), but following the beginning of cracking, it indicated a transient increase in stiffness. But this increase faded past about 85% of the final load, at which point the beam lost both stiffness and load-carrying capacity relative to **G4-HT-S-2**. It still had less deflection than the control specimens, however. The link between the struts at midspan using angle steel sections may explain the first improvement; this connection helped to momentarily redistribute stress and stabilize the structure. Compared to the control specimens, the last beam in the group (**G4-HT-S-4**), showed a slight increase in stiffness during the early loading stage. Stiffness decreased fast, though, once second stage cracking started. Experiencing abrupt diagonal shear failure, the beam finally failed at a lower load than (**G1-CO-3**). Insufficient strut region reinforcement, where reinforcement was given just on one side caused this early failure. A weak path along the unreinforced inner side was created by this, which let diagonal shear cracks grow and spread quickly, therefore causing early failure before the beam could attain greater load levels. All things considered, this group showed how much stiffer and more load resistant triangular hybrid reinforcement could be, particularly if the strut area is sufficiently and symmetrically strengthened. The difference in performance among the samples highlights the importance of reinforcement layout and confinement in controlling structural behavior under load.

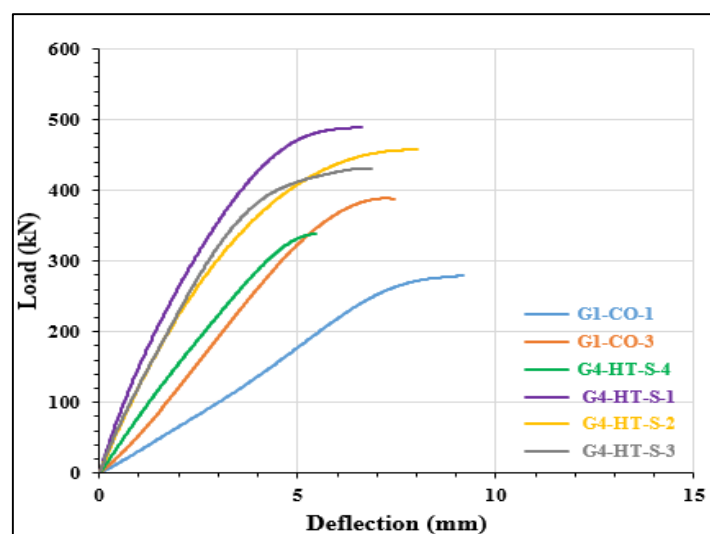


Figure 4.4 Load - Deflection Curves for fourth group specimens (G4).

4.4 Effective Stiffness

Stiffness (K_e) quantifies the resistance of an elastic body to deformation. In this study, the effective secant stiffness corresponding to 75% of the ultimate load ($0.75 \times P_u$) is used for evaluation, as defined by Eq. 4.1 [76].

$$K_e = 0.75P_u / \Delta_{0.75P_u} \quad 4.1$$

K_e : effective stiffness.

P_u : ultimate load.

$\Delta_{0.75P_u}$: deflection value corresponding to the $0.75 P_u$ load level.

Based on the results presented in Table 4.5 and Fig.4.20, there is a clear improvement in the stiffness of the proposed specimens compared to the control specimens.

Table 4.5 The effective stiffness test results for the tested beams

Groups No.	No.	Specimens	0.75 P_u (kN)	0.75 P_u Deflection (mm)	Stiffness K_e (kN/mm)
G1	1	G1-CO-1	210.0	5.880	35.71
	2	G1-CO-2	232.5	4.112	56.54
	3	G1-CO-3	292.5	4.321	67.70
	4	G1-CO-4	307.5	4.466	68.85
G2	1	G2-HA-B-1	315.0	4.030	78.16
	2	G2-HA-B-2	322.5	3.110	103.70
	3	G2-HA-B-3	337.5	4.050	83.33
	4	G2-HA-B-4	330.0	4.215	78.29
G3	1	G3-HA-S-1	315.0	3.304	95.34
	2	G3-HA-S-2	277.5	5.580	50.00
	3	G3-HA-S-3	405.0	3.604	112.40
G4	1	G4-HT-S-1	367.5	3.068	119.80
	2	G4-HT-S-2	345.0	3.743	92.20
	3	G4-HT-S-3	322.5	2.999	107.54
	4	G4-HT-S-4	255.0	3.562	71.60

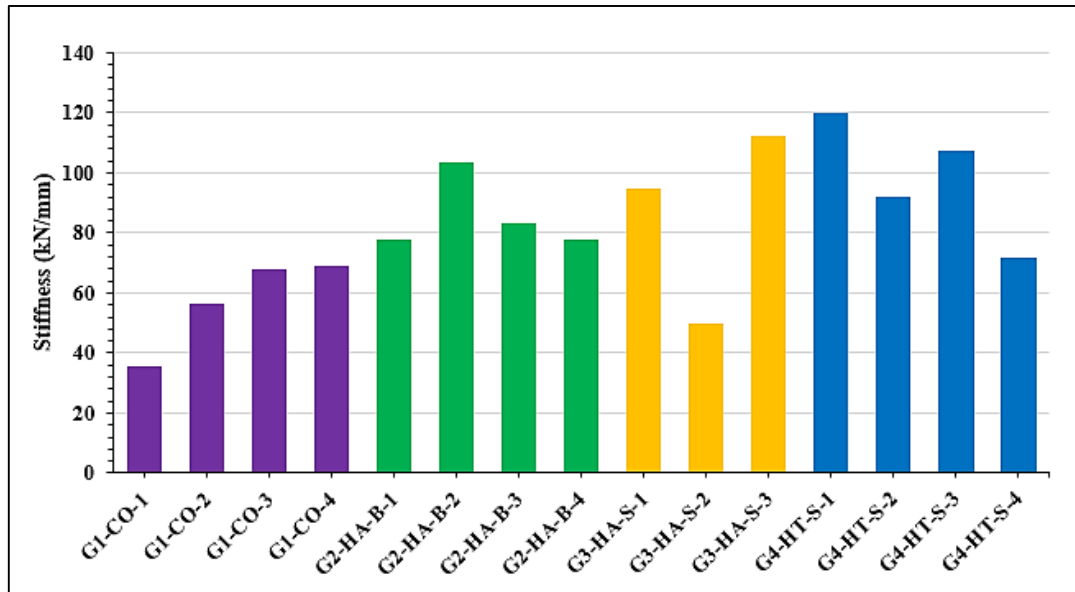


Figure 4.5 The effective stiffness results for all the tested beams

The second group demonstrated a significant increase in stiffness compared to the control specimens (**G1-CO-2**) and (**G1-CO-4**), the first beam in this group (**G2-HA-B-1**) showed improvements of 38.1% and 13.3% respectively compared to the control specimens, confirming the effectiveness of the arch action. The second beam **G2-HA-B-2** exhibited the highest stiffness improvement within the group, achieving 83.54% and 50.62% compared to the control specimens, and 33% compared to the previous beam **G2-HA-B-1**. This highlights the critical role of the tie reinforcement configuration and the use of high-strength concrete. The third beam (**G2-HA-B-3**) demonstrated stiffness improvements of 47.43% and 21% compared to the control specimens, although it did not outperform the preceding beam. Finally, the fourth beam **G2-HA-B-4** showed improvements of 38.6% and 13.7%, closely matching the performance of the first beam **G2-HA-B-1**.

As for the third group, despite replacing the strut reinforcement with angle steel sections, the specimens showed an overall increase in stiffness compared to the control specimens (**G1-CO-2**) and (**G1-CO-4**), confirming the effectiveness of this reinforcement technique. The first beam (**G3-HA-S-1**) exhibited stiffness improvements of 68.14% and 37.98%, respectively compared to the control specimens. In contrast, the second beam (**G3-HA-S-2**) showed a decrease in

stiffness of 11.5% and 27.38%, indicating that improper use or insufficient quantity of reinforcement can negatively affect performance. Meanwhile, the third beam (**G3-HA-S-3**) achieved the highest improvements in this group, with increases of 98.94% and 63.25%, respectively compared to the control specimens. These findings highlight that while the use of angle steel sections can enhance stiffness, their effectiveness heavily depends on the quantity and configuration of the reinforcement. Comparing beam (**G3-HA-S-1**) with beam (**G2-HA-B-1**), the former showed a 21.78% higher stiffness, further emphasizing the potential of angle steel sections in enhancing arch action and supporting the strut region.

"The fourth group exhibited the highest stiffness improvements compared to the triangular control specimens in both strut shape and reinforcement configuration (**G1-CO-1** and **G1-CO-3**). Beam **G4-HT-S-1** showed the greatest enhancement across all tested groups, with increases of 235.6% and 77%, respectively, relative to the control specimens. Beam **G4-HT-S-2** demonstrated improvements of 158.3% and 36.2%, though this represented a 23% reduction compared to beam **G4-HT-S-1**. Beam **G4-HT-S-3** recorded gains of 201.1% and 58.8%, while the final beam, **G4-HT-S-4**, achieved increases of 100.6% and 5.76%, respectively. These results clearly highlight the effectiveness of both reinforcement method and strut geometry in enhancing beam stiffness. These results demonstrate the significant influence of several factors on beam stiffness, including the type of concrete used, the reinforcement method, the type of reinforcement, the shape of the hybridization, and the geometry of the strut region.

4.5 Ductility index

The degree to which a component may deform beyond yielding prior to failure is known as ductility [78]. It serves as an indicator for the potential margin of safety that a member which offer. The displacement ratio, which can be defined as the ratio of maximum displacement to a specific displacement as indicated by the intersections of the two tangents to the initial and final points of

the load-deflection curve as illustrated in Fig. 4.21, is the basis for the method that has predicted the ductility ratio for the tested specimens. The ductility index can thus be written as in Eq. 4.2. Table 4.6 and Fig.4.22 present the ductility results for all tested specimens

$$\mu_{\Delta} = \Delta_u / \Delta_y \quad 4.2$$

where:

μ_{Δ} : ductility index

Δ_u : deflection value at ultimate load

Δ_y : deflection value at service load.

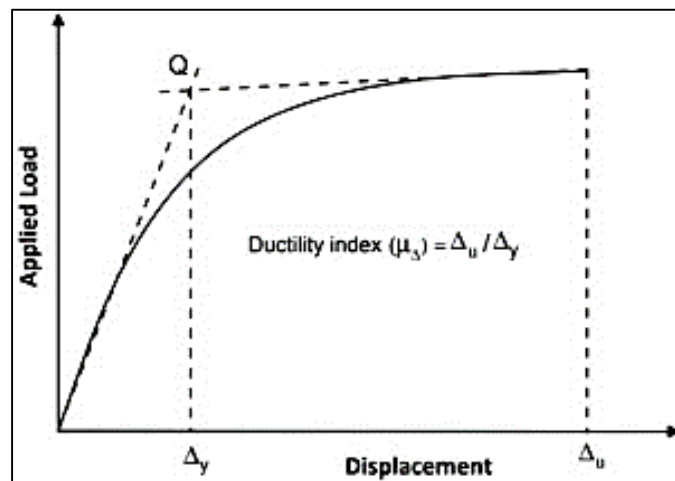


Figure 4.6 Calculating the ductility ratio using displacement ratio method [78]

Table 4.6 Ductility index results for all tested specimens.

Groups No.	No.	Specimens	Service Deflection Δ_y (mm)	Ultimate Deflection Δ_u (mm)	Ductility index (Δ_u/Δ_y)
G1	1	G1-CO-1	7.931	9.200	1.16
	2	G1-CO-2	4.368	6.552	1.50
	3	G1-CO-3	5.816	7.445	1.28
	4	G1-CO-4	3.994	7.230	1.81
G2	1	G2-HA-B-1	4.600	6.836	1.49
	2	G2-HA-B-2	3.793	5.880	1.55
	3	G2-HA-B-3	3.005	6.220	2.07
	4	G2-HA-B-4	4.700	7.110	1.51
G3	1	G3-HA-S-1	3.205	6.730	2.10
	2	G3-HA-S-2	5.916	8.283	1.40
	3	G3-HA-S-3	3.902	6.868	1.76
G4	1	G4-HT-S-1	3.005	6.612	2.20
	2	G4-HT-S-2	3.200	8.030	2.51
	3	G4-HT-S-3	3.404	6.877	2.02
	4	G4-HT-S-4	3.914	5.480	1.40

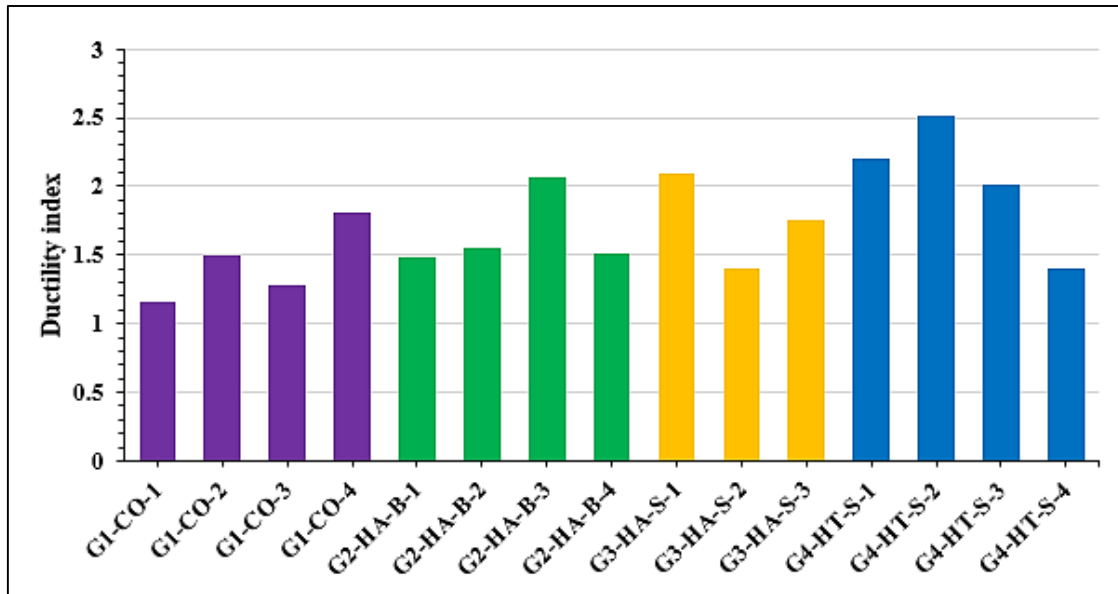


Figure 4.7 Ductility index results for all tested specimens.

It is evident from the attached results that the use of angle steel sections significantly enhanced ductility.

In the first group, when the reinforcement configuration was changed from triangular to arched, ductility improved by 29.31% and 41.41% for the comparisons between beams (G1-CO-1) and (G1-CO-2), and (G1-CO-3) and (G1-CO-4), respectively. Additionally, when the concrete type was changed to high-strength concrete, ductility increased by 10.34% and 20.67% in the comparisons between beams (G1-CO-1) and (G1-CO-3), and (G1-CO-2) and (G1-CO-4), respectively.

For the second group, when compared with the control beam (G1-CO-2), beams (G2-HA-B-2), (G2-HA-B-3), and (G2-HA-B-4) exhibited improvements in ductility of 3.3%, 38%, and 1.0%, respectively. However, when compared with the control beam (G1-CO-4), beam (G2-HA-B-3) showed a slight increase in ductility of 14.36%, whereas beams (G2-HA-B-1), (G2-HA-B-2), and (G2-HA-B-4) exhibited reductions in ductility of 18%, 14.36%, and 16.4%, respectively. These results suggest that although the strengthening methods applied in this group enhanced load-bearing capacity, they also reduced overall deflection. Also,

the use of high strength concrete in the strut and tie regions caused brittle failure which reduce the overall ductility of the deep beams. As a result, the ductility decreased, leading to a more brittle behavior compared to the control beam (G1-CO-4). Additionally, the lower (a/d) ratio may have contributed to a more brittle failure mode, further limiting the ductility performance [79].

In the third group, specimens (G3-HA-S-1), and (G3-HA-S-3) demonstrated ductility improvements of 40%, and 17.3%, respectively, when compared to the control beam (G1-CO-2). When compared with the control beam (G1-CO-4), specimens (G3-HA-S-1) showed ductility increases of 16 %, respectively, whereas specimens (G3-HA-S-2) and (G3-HA-S-3) exhibited a decrease in ductility of 22.65%. and 2.76%. This reduction is attributed to the decreased amount of steel reinforcement in the strut region, which likely contributed to the lower ductility observed.

The fourth and final group exhibited the highest improvements in ductility among all the tested specimens. Compared to the control beam (G1-CO-1), specimens (G4-HT-S-1), (G4-HT-S-2), (G4-HT-S-3), and (G4-HT-S-4) showed ductility increases of 89.66%, 116.38%, 74.14%, and 20.7%, respectively. When compared to the control beam (G1-CO-3), the improvements were 71.88%, 96.1%, 57.81%, and 9.38%, respectively. This significant enhancement in ductility can likely be attributed to the effective application of the Strut-and-Tie Model (STM), which performs optimally at a shear span-to-depth ratio (a/d) of 1. Furthermore, the use of angle steel sections for reinforcement contributed to the improved overall ductile behavior of the beams in this group, as in the third group.

4.6 Energy Absorption Capacity

Toughness quantifies a member's ability to withstand deformation before failure. It is represented by the area under the load-deflection curve, which

reflects the energy dissipated due to material degradation up to failure [80]. Table 4.7 and Fig. 4.23 present the toughness results for all tested specimens.

Table 4.7 Toughness results of all examined specimens

Groups No.	No.	Specimens	Energy Absorption (kN.mm)
G1	1	G1-CO-1	1447
	2	G1-CO-2	1150
	3	G1-CO-3	1689
	4	G1-CO-4	1838
G2	1	G2-HA-B-1	1700
	2	G2-HA-B-2	1572
	3	G2-HA-B-3	1682
	4	G2-HA-B-4	1872
G3	1	G3-HA-S-1	1888
	2	G3-HA-S-2	1696
	3	G3-HA-S-3	2396
G4	1	G4-HT-S-1	2225
	2	G4-HT-S-2	2564
	3	G4-HT-S-3	2070
	4	G4-HT-S-4	1078

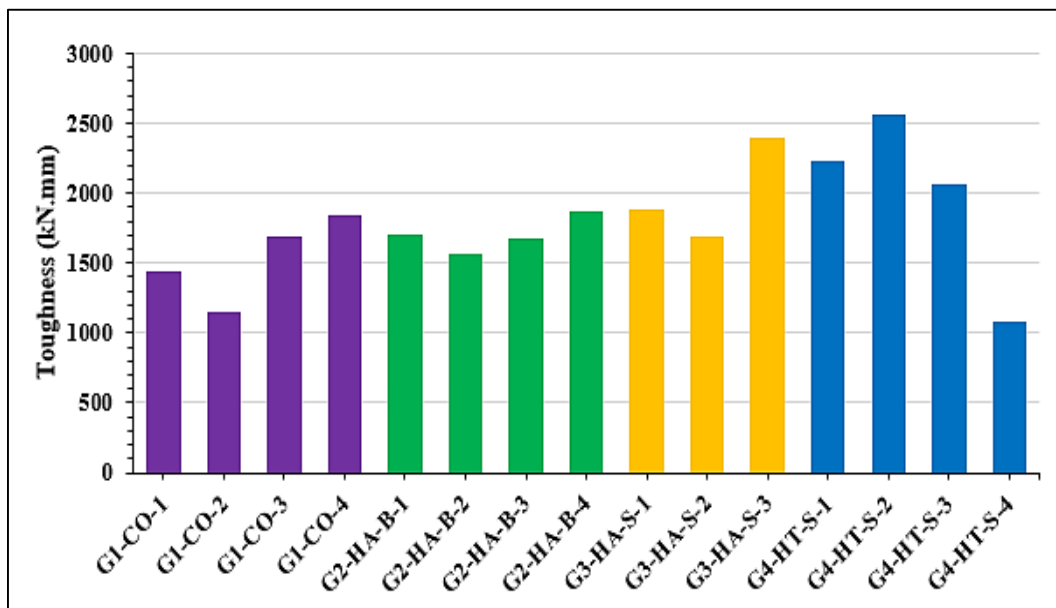


Figure 4.8 Toughness results of all examined specimens

For the control specimens, an improvement in toughness of 16.7% and 60% was observed when the concrete type was changed to high-strength concrete. This comparison was made between specimens (**G1-CO-1**) and (**G1-CO-3**), and (**G1-CO-2**) and (**G1-CO-4**), respectively.

In the second group, specimens **G2-HA-B-1**, **G2-HA-B-2**, **G2-HA-B-3**, and **G2-HA-B-4** demonstrated toughness increases of 47.8%, 36.7%, 46.3%, and 62.8%, respectively, compared to the control specimen **G1-CO-2**. Additionally, specimen **G2-HA-B-4** showed a modest toughness improvement of 1.85% relative to control beam **G1-CO-4**. In contrast, specimens **G2-HA-B-1**, **G2-HA-B-2**, and **G2-HA-B-3** exhibited decreases in toughness of 7.5%, 14.5%, and 8.5%, respectively, when compared to control beam **G1-CO-4**.

The third group, when compared to control beam **G1-CO-2**, demonstrated increases in toughness of 64.2%, 47.5%, and 108.3% for specimens **G3-HA-S-1**, **G3-HA-S-2**, and **G3-HA-S-3**, respectively. When compared to control beam **G1-CO-4**, specimens **G3-HA-S-1** and **G3-HA-S-3** showed improvements of 2.7% and 30.4%, respectively, whereas specimen **G3-HA-S-2** exhibited a decrease of 7.7%.

In the fourth group, specimens **G4-HT-S-1**, **G4-HT-S-2**, and **G4-HT-S-3** exhibited toughness increases of 53.8%, 77.2%, and 43%, respectively, relative to control beam **G1-CO-1**. In contrast, specimen **G4-HT-S-4** showed a 25.5% decrease in toughness. When compared to control beam **G1-CO-3**, the same specimens **G4-HT-S-1**, **G4-HT-S-2**, and **G4-HT-S-3** demonstrated improvements of 31.7%, 51.8%, and 22.6%, respectively, while **G4-HT-S-4** recorded a 36.2% reduction.

4.7 Cracks propagation characteristics

In general, all tested deep beam specimens demonstrated elastic behavior during the initial stages of loading, characterized by small, proportional mid-span deflections in response to the applied loads. At these low load levels, the induced stresses remained minimal, and the entire cross-sectional area of the beams effectively contributed to load resistance. This phase was marked by a linear load-deflection relationship, indicating the dominance of elastic behavior prior to the onset of cracking.

The first visible cracks typically emerged in the region subjected to the minimum bending moment, with initial flexural cracks forming along the bottom face of the deep beams. These early cracks propagated vertically upward as the applied load increased, signaling the transition from elastic behavior to the initiation of plastic behavior within the concrete tension zones. All the loads pertaining to the first crack have been thoroughly compiled and are clearly presented in Table 4.1, providing a comprehensive overview for reference. Following the completion of the elastic stage, during which all specimens behaved linearly and exhibited minimal deformation, each group began to develop a distinct cracking pattern as they transitioned into the plastic stage. This stage, marked by the formation and propagation of cracks beyond the initial cracking load, revealed significant differences in structural behavior among the various groups. The nature, orientation, and distribution of cracks notably varied, depending on the configuration, material composition, and reinforcement type used in each group. These variations highlight the influence of structural parameters on the post-cracking response of the beams, as detailed in the sub sections below.

4.7.1.1 First group specimens

For the first control beam (**G1-CO-1**), which was constructed using normal-strength concrete and reinforced with a triangular steel configuration, the initial

cracking behavior was observed under a gradually applied load. The first visible crack appeared at a load of 170 kN within the tension zone at mid-span. As the load continued to increase, flexural crack developed adjacent to the initial crack, indicating progressive flexural failure in the bottom region of the beam. With further loading, these cracks propagated toward the loading point, showing signs of stress redistribution and increased strain in the flexural region. Subsequently, the first crack in the strut zone emerged; however, this crack did not propagate significantly. The failure of the beam occurred shortly thereafter due to crushing in the nodal zone, suggesting that the ultimate failure mode was governed by localized compression failure at the node (bearing failure), rather than by the development of a continuous diagonal cracking pattern, see Fig 4.1.

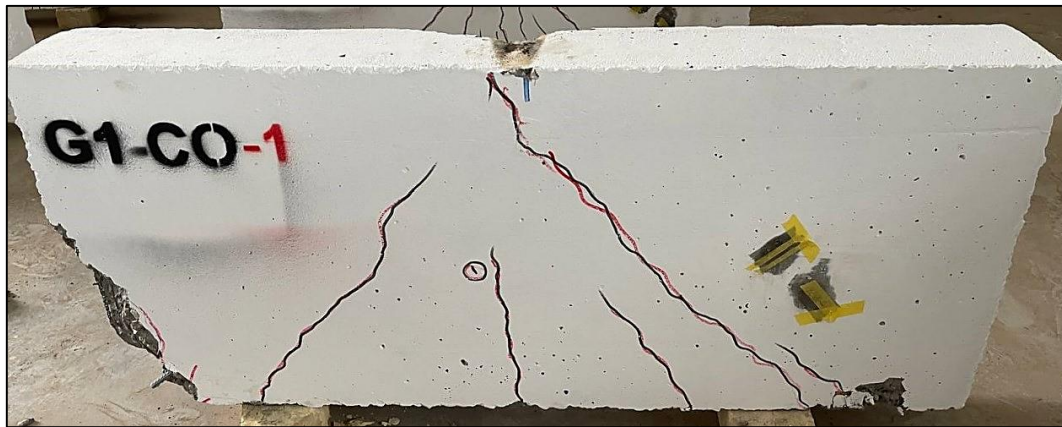


Figure 4.9 Cracks propagation for specimen G1-CO-1.

The second beam (**G1-CO-2**), constructed using normal strength concrete and reinforced with an arch-shaped steel configuration, exhibited slightly different behavior compared to the first control beam. The first visible crack appeared at a load of approximately 180 kN, indicating a slight delay in crack initiation. This delay can likely be attributed to the contribution of the arch-shaped reinforcement, which may have enhanced the internal load redistribution and contributed to improved initial stiffness through arch action.

As the applied load increased, multiple cracks began to form primarily within the tension zone and extended upward. These cracks propagated in a direction more inclined toward the loading point when compared to those observed in the first beam (**G1-CO-1**), suggesting a more efficient load path due to the arch-shaped reinforcement. The improved performance in terms of delayed cracking and directional crack propagation reinforces the idea that arch action provides better structural resistance, particularly in the early stages of loading, see Fig 4.2.

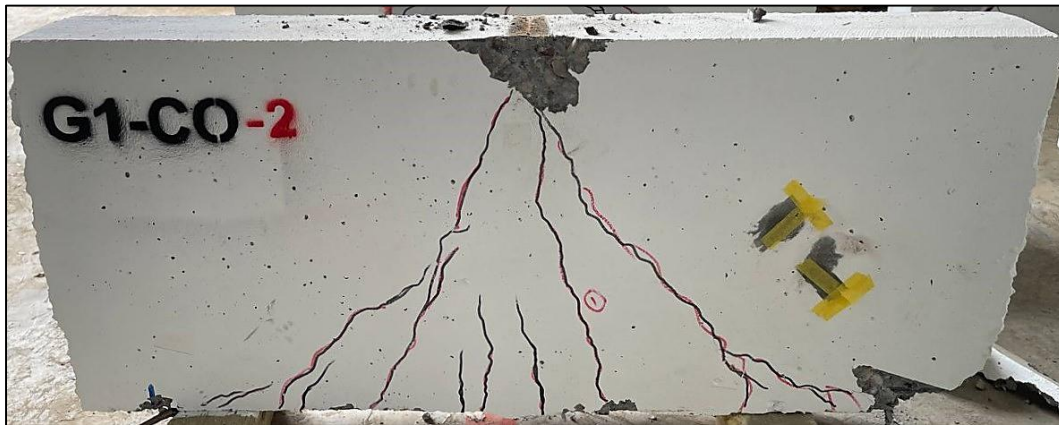


Figure 4.10 Cracks propagation for specimen G1-CO-2.

Despite these improvements, fine cracks began to emerge within the strut zone at higher load levels. However, these cracks remained shallow and barely visible, as the beam experienced premature failure due to crushing in the nodal zone similar to the failure observed in (**G1-CO-1**). This type of failure highlights a limitation in the compressive strength of the concrete, which in both beams was approximately 25 MPa. The relatively low concrete strength was insufficient to resist the concentrated compressive stresses at the nodal regions, leading to localized crushing before the full development of diagonal or strut-related cracks. Overall, although the arch-shaped reinforcement in (**G1-CO-2**) demonstrated some improvement in delaying the onset of cracking and in directing crack propagation more efficiently, the overall structural behavior and failure mode remained governed by the compressive weakness of the nodal zone. This underscores the critical importance of concrete strength in the performance of

deep beams, especially where nodal crushing is a dominant failure mechanism.

The third beam (**G1-CO-3**), constructed with high-strength concrete and reinforced using a triangular steel configuration, demonstrated superior performance compared to the previous two control specimens. When subjected to a gradually applied load, the beam exhibited predominantly elastic behavior during the initial loading phase. The first visible crack appeared at a load of approximately 180 kN. This value represents an increase of 5.9% compared to the first beam (**G1-CO-1**) which was cast using normal-strength concrete. Following the onset of the first crack, the beam transitioned into the plastic stage, during which a series of cracks began to develop within the tensile zone. As the load continued to increase, the number of flexural cracks grew progressively, propagating toward the region beneath the loading point. The distribution and density of these cracks reflected the beam's enhanced capacity to redistribute internal stresses and absorb energy beyond the elastic limit. At more advanced stages of loading, additional cracks began to emerge along the inner edges of the strut region. These cracks widened progressively as the beam approached failure, indicating the increasing dominance of diagonal tensile stresses. The failure ultimately occurred as a result of excessive cracking and stress concentration in the strut zone, despite the higher compressive strength of the concrete as illustrated in Fig. 4.3.

Overall, (**G1-CO-3**) beam's performance underscores the significant impact of using high-strength concrete in deep beams, particularly in terms of enhancing load capacity and improving the beam's toughness. The results also suggest that while reinforcement geometry influences crack patterns and failure progression, the compressive strength of the concrete remains a critical factor in determining both the cracking behavior and the ultimate failure load.

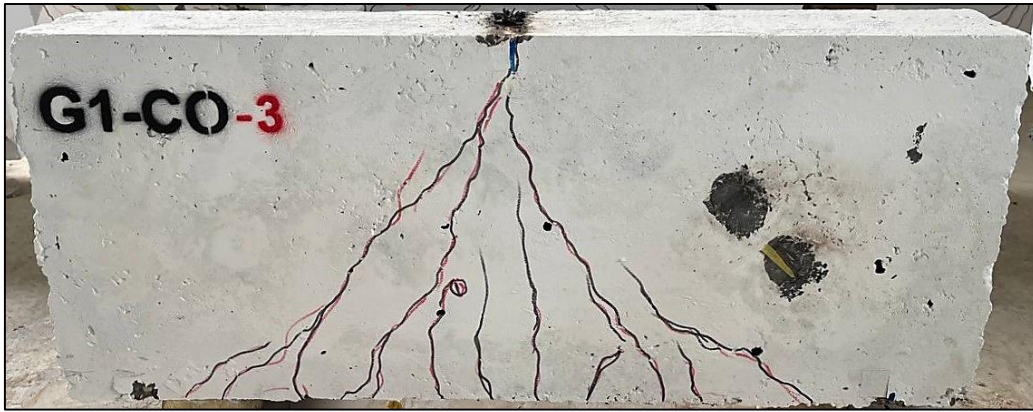


Figure 4.11 Cracks propagation for specimen G1-CO-3.

Finally, the fourth beam **G1-CO-4**, constructed using high-strength concrete and reinforced with an arch-shaped steel configuration, demonstrated enhanced structural performance in terms of both cracking resistance and ultimate load capacity. Under gradual loading, the beam exhibited elastic behavior during the initial phase, maintaining linear load-deflection characteristics until the appearance of the first visible crack at a load of 200 kN. This value represents an increase of 17.65% and 11.1% compared to the first (**G1-CO-1**) and second (**G1-CO-2**) beams, respectively—both of which were cast using normal-strength concrete. The improved resistance to cracking in (**G1-CO-4**) can be attributed to two key factors. These are the use of high-strength concrete, which reached a compressive strength of 87.83 MPa, and the beneficial influence of the arch-shaped reinforcement configuration that promotes efficient load transfer and structural stability through arch action. Upon the formation of the first crack, the beam entered the plastic phase, during which additional cracks began to develop within the tension zone. These cracks gradually increased in number and length, propagating toward the loading region as the applied load intensified. As loading continued, fine diagonal cracks also emerged at the inner edges of the strut zone. These cracks progressively widened, reflecting the concentration of internal stresses and the progression toward failure. The final failure occurred as the

diagonal cracks in the strut zone reached critical width, leading to structural collapse, as illustrated in Fig. 4.4.

Overall, the performance of beam **(G1-CO-4)** highlights the combined benefits of using high-strength concrete and arch reinforcement. This configuration not only delayed the initiation of cracking but also enhanced the beam's capacity to withstand higher loads before failure, confirming the effectiveness of arch action in improving the structural behavior of deep beams.

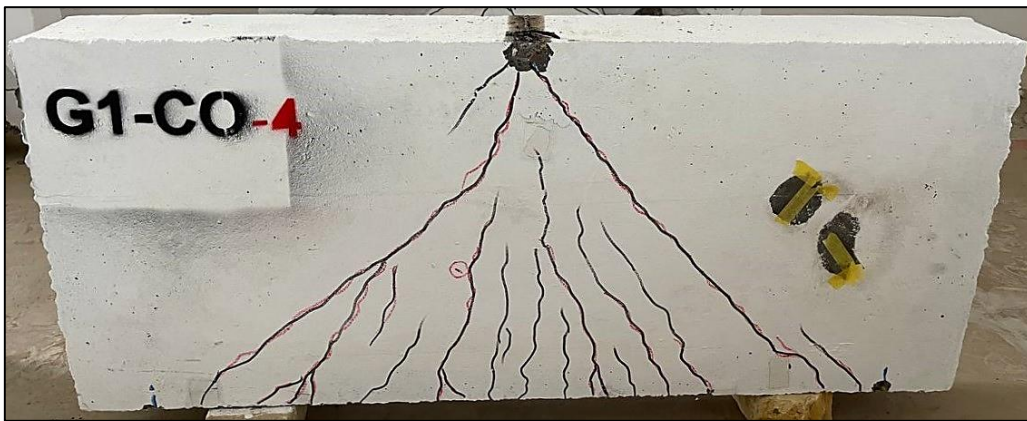


Figure 4.12 Cracks propagation for specimen G1-CO-4.

4.7.1.2 Second Group Specimens (G2)

The second group of specimens was distinguished by an arc-shaped hybrid configuration, where high-strength concrete was strategically applied in the strut regions in conjunction with conventional reinforcing steel bars. The structural detailing and material composition of this group are thoroughly described in Chapter Three. The following outlines the performance and failure characteristics observed in the beams within this group during the experimental testing phase.

The first specimen in this group, designated as **(G2-HA-B-1)**, exhibited the initial appearance of cracking at a comparatively lower load level approximately 160 kN compared to all control specimens. This early cracking can be primarily attributed to the hybrid nature of the beam. Due to the variation in mechanical properties and load distribution characteristics between the high-strength and

normal-strength concrete components, differential behavior under loading occurred, leading to premature crack initiation. As the applied load increased, visible cracks began to develop within the strut regions, following the anticipated stress trajectory along the strut axis. With continued loading, additional cracks emerged, propagating parallel to the initial crack within the same regions. These progressive crack formations signaled a redistribution of internal stresses, ultimately culminating in structural failure. The final failure pattern and crack propagation behavior are illustrated in Fig.4.5, highlighting the concentration of damage in the strut-dominated regions.



Figure 4.13 Cracks propagation for specimen G2-HA-B-1.

The second beam in this group, identified as (**G2-HA-B-2**), differed from the first beam (**G2-HA-B-1**) primarily in the reinforcement strategy applied to the tie. In this specimen, stirrups were used along the length of the tie, and high-strength concrete was employed throughout. These modifications significantly influenced the structural response of the beam. Notably, the first visible crack in (**G2-HA-B-2**) appeared at a load of 240 kN the highest among all the tested specimens. This cracking load represented an increase of approximately 33.3%, 20%, and 50% compared to specimens (**G1-CO-2**), (**G1-CO-4**), and (**G2-HA-B-1**), respectively. The enhanced cracking resistance observed in (**G2-HA-B-2**) can be primarily attributed to the revised tie reinforcement method, in conjunction with the use of high-strength concrete. These modifications enabled the tie region

to behave more effectively as a tension-resisting element, exhibiting improved performance under load and delaying the onset of cracking. This interpretation is supported by the location and nature of the initial crack, which emerged at the upper edge of the tie, indicating tensile stress concentration in that zone. As the applied load increased, the initial cracks widened and became more pronounced. Simultaneously, additional cracks began to develop in the area bounded between the arched strut and the tie, propagating upward from the tie toward the loading point. With further loading into advanced stages, cracks also appeared in the strut region and the nodal zone, ultimately leading to failure. The failure mechanism was characterized by the formation and extension of a dominant diagonal crack within the strut region, culminating in the collapse of the beam. The progression of crack development and failure mode is illustrated in Fig 4.6.

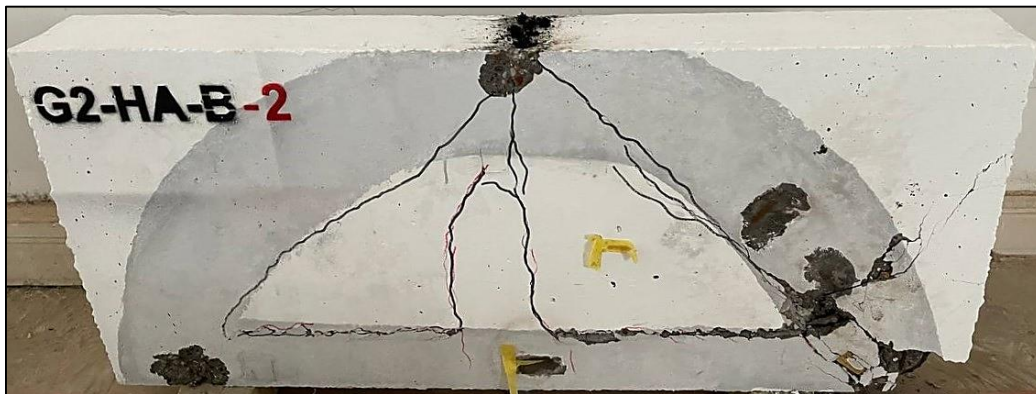


Figure 4.14 Cracks propagation for specimen G2-HA-B-2.

The third specimen (**G2-HA-B-3**), shares a nearly identical design with the second beam (**G2-HA-B-2**), with the primary distinction being the incorporation of two additional ribs intended to reinforce the arching action of the strut region. Based on the structural behavior observed in (**G2-HA-B-2**), the third beam exhibited a comparable response under loading. The first visible crack appeared at a load of 210 kN higher than that recorded in the control specimens (**G1-CO-2**) and (**G1-CO-4**), as well as the first hybrid beam (**G2-HA-B-1**), by 16.67%, 5%, and 31.25%, respectively. However, this cracking load was 12.5% lower than that observed in (**G2-HA-B-2**). This reduction in the load corresponding to the

first crack may be attributed to the presence of the added ribs, which likely altered the internal force distribution. Specifically, these ribs may have redirected a portion of the compressive load within the strut region toward the tie region. As a result, the tie was subjected to direct bending stresses, particularly concentrated at its midpoint, where the ribs intersected with the tie. This hypothesis is supported by the observed crack patterns: flexural cracks were noted developing in the tie region, initiating from the bottom face and propagating upward toward the load application point. This behavior contrasts with that of beam **(G2-HA-B-2)**, in which no flexural cracking penetrated the body of the tie; instead, cracking was limited to the upper surface of the tie, indicating a different stress path. The crack map shown in Fig.4.7 illustrates the distribution and orientation of cracks in **(G2-HA-B-3)**, further validating this interpretation of the structural response.



Figure 4.15 Cracks propagation for specimen G2-HA-B-3.

The fourth and final specimen in this group, designated as **(G2-HA-B-4)**, is an extension of the previous configuration **(G2-HA-B-3)**, with the key modification being the addition of a third rib to support the arching action within the strut region. This brought the total number of supporting ribs to three, further enhancing the structural stiffness and load distribution characteristics in the strut zone. Despite this structural enhancement, the overall behavioral pattern of **(G2-HA-B-4)** closely mirrored that of beam **(G2-HA-B-3)**. The first visible crack in **(G2-HA-B-4)** emerged at a load of 230 kN, substantially higher than the values

recorded for the control specimens (**G1-CO-2**) and (**G1-CO-4**), as well as beams (**G2-HA-B-1**) and (**G2-HA-B-3**). Specifically, the cracking load represented increases of approximately 27.78%, 15%, 43.75%, and 9.52%, respectively. Similar to the third beam, initial cracking originated within the tension zone, beginning from the lower edge of the tie region and propagating upward toward the point of load application. This cracking pattern further reinforces the interpretation made in the previous case: the additional ribs likely redirected a portion of the compressive forces from the strut region into the tie region, introducing significant bending moments, particularly at mid-span.

As a result, the tie exhibited flexural cracking under combined axial and bending stresses. As the applied load increased, additional cracks began to develop within the strut region. However, these cracks did not progress extensively due to premature crushing in the nodal zone, which marked the onset of structural failure. The failure was thus governed more by compressive failure in the nodal zone than by crack propagation in the struts. Fig.4.8 illustrates the crack pattern and failure mode observed in this specimen.

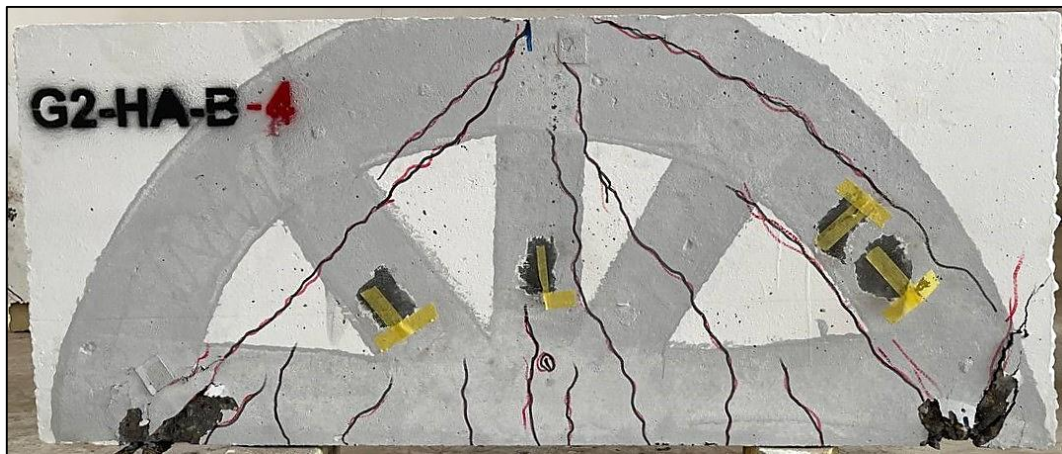


Figure 4.16 Cracks propagation for specimen G2-HA-B-4.

4.7.1.3 Third Group Specimens (G3)

The reinforcement configuration in this group closely resembled that of the previous group (**G2**), utilizing an arched reinforcement layout. However, it

differed notably through the incorporation of angle steel sections to reinforce the strut region. This group also did not exhibit any significant improvement in terms of the first-crack load when compared to the control specimens. In fact, the first-crack loads were generally lower across the group, with the exception of beam **(G2-HA-S-3)**, which demonstrated a marginal enhancement in cracking resistance relative to the control.

In the case of the first beam in this group **(G3-HA-S-1)**, a key distinguishing feature was the robust and tightly arranged strut reinforcement. This enhancement significantly contributed to a stronger arching action within the beam. Despite this improved reinforcement, it did not delay the initial appearance of cracking. The first crack was observed at a load of 150 kN, which is consistent with the performance of the initial specimen from the second group **(G2-HA-B-1)**. As previously discussed, this early crack initiation is primarily attributed to the different concrete types used between the groups. As the applied load increased, the first visible crack emerged near the strut region, specifically at the commencement of the arch on the support side.

With continued loading, cracking began to manifest in the tensile zone at the midspan of the beam, on the underside. Simultaneously, additional cracks started to propagate within the strut region itself. During this stage of loading, intensive cracking was also observed in the nodal zone, indicating significant stress concentration. At the peak and ultimate load stages, a major crack formed along the inner edge of the strut. However, this crack did not propagate fully to the loading point due to the strategic placement of the angle steel sections in close proximity, which helped to delay the damage.

Despite this, the nodal zone experienced considerable structural deterioration. Ultimately, the failure mechanism of the beam can be classified as a combination of shear failure and bearing failure degradation, influenced by both the reinforcement detailing and the inherent material properties. See Fig 4.9.

Beam (**G3-HA-S-2**), which was designed with only half the amount of strut reinforcement used in the previous beam (**G3-HA-S-1**), exhibited structural behavior that was not markedly different overall. Upon the application of load, the first visible crack appeared at 180 kN. This value is comparable to that of the control specimen (**G1-CO-2**) and approximately 10% lower than that of control specimen (**G1-CO-4**). As loading progressed, cracks began to develop in the tensile zone, particularly near the strut side. At more advanced stages of loading, a prominent crack initiated on the inner edge of the strut.

With continued load application, this crack widened progressively and ultimately led to a separation indicative of a splitting shear failure in the strut region. It is noteworthy that the strut reinforcement in this beam did not prevent the formation or progression of this critical crack, in contrast to the behavior observed in beam (**G3-HA-S-1**). This may be attributed to the reduced quantity of strut reinforcement in (**G3-HA-S-2**), which not only provided less overall confinement but also supported the strut from only one side, thereby offering limited restraint. This behavior is illustrated in Fig 4.10.



figure 4.17 cracks propagation for specimen G3-HA-S-1.

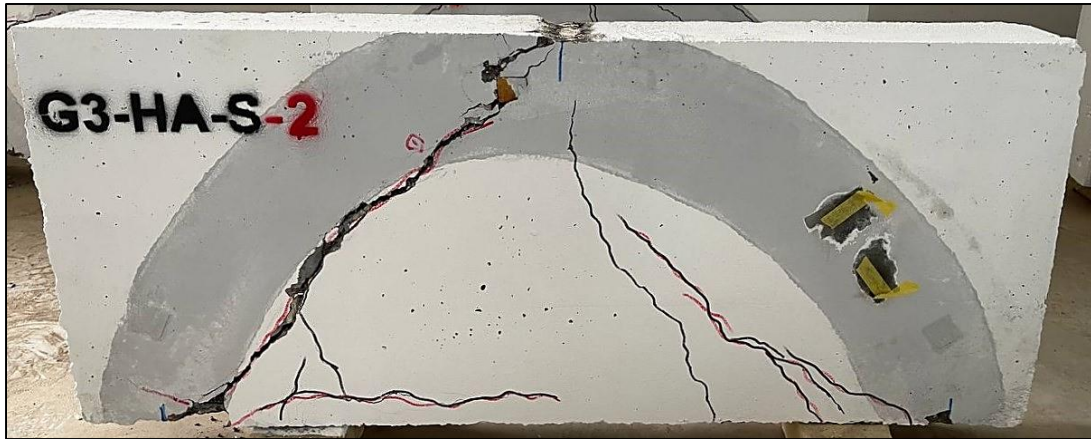


Figure 4.18 Cracks propagation for specimen G3-HA-S-2.

The final specimen in this group, designated as beam (**G3-HA-S-3**), exhibited notably different structural behavior compared to the previous beams within the same group. One of the most significant observations was the delay in the formation of the first visible crack, which occurred at a load level of 200 kN. This value represents an 11.1% increase relative to the first-crack load of the control specimen (**G1-CO-2**), and it matches the corresponding value recorded for the second control specimen (**G1-CO-4**). This improvement in cracking resistance highlights the potential effectiveness of the slight modification introduced to the reinforcement detailing in this beam. In terms of reinforcement configuration, specimen (**G3-HA-S-3**) was largely similar to (**G3-HA-S-2**), with one key exception: the incorporation of two additional transverse ribs. These ribs were strategically placed to provide additional support to the arched strut region, thereby aiming to improve the internal stress distribution and potentially strengthen the beam's capacity to resist cracking and failure mechanisms. As the applied load increased beyond the initial cracking of beam. A widespread and well-distributed pattern of cracks began to emerge in the tensile zone, particularly concentrated around the midspan of the beam. Among these, a relatively large and prominent crack developed at the central region of the beam, extending vertically between the two added ribs. This observation suggests a significant accumulation of tensile stresses in that area, which may be associated with the

altered stiffness and force path induced by the presence of the ribs. Simultaneously, as loading progressed, additional cracks began to form within the strut region, indicating that while the ribs contributed to improved behavior in the tensile zone, the strut region remained susceptible to stress-induced damage. At more advanced loading stages approaching ultimate capacity, further cracking was observed in the strut area. These new cracks developed in a pattern that was generally parallel to the initial cracks, reflecting the ongoing propagation of stress and the progressive deterioration of the concrete area in this critical region. At the final stages of loading, near or at the ultimate load capacity, the crack development reached its peak. Despite the presence of reinforcement and the added ribs, failure eventually occurred, marking the end of the crack propagation phase. The failure pattern, dominated by extensive cracking in both the strut and mid-span tension zones, as illustrated in Fig.4.11. This behavior highlights the complex relationship between reinforcement detailing, stress distribution, and structural response. The improved cracking resistance due to the added ribs is evident, but the failure still followed a mechanism involving both flexural tension cracking and degradation within the strut region, emphasizing the need for comprehensive reinforcement strategies in such configurations.

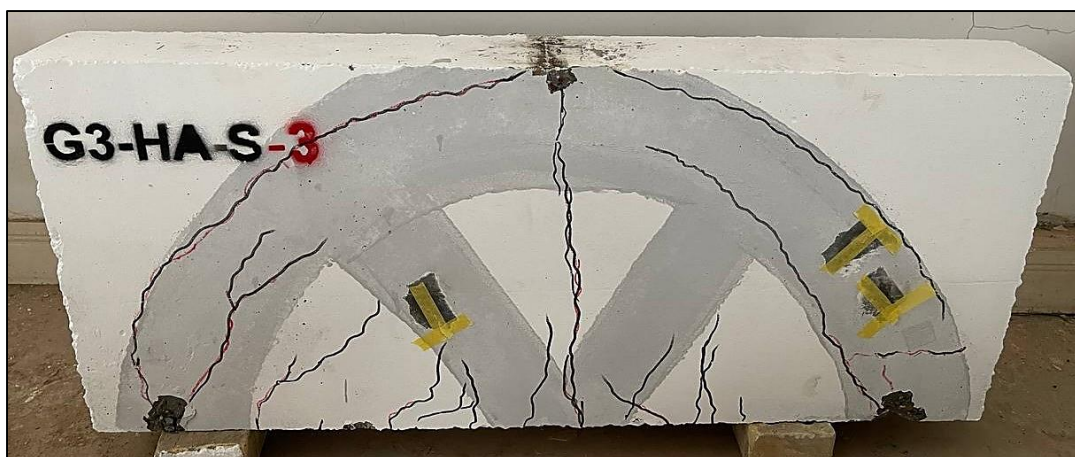


Figure 4.19 Cracks propagation for specimen G3-HA-S-3.

4.7.1.4 Fourth Group Specimens (G4)

The fourth group of specimens (**G4**) was uniquely reinforced compared to the previous groups. In this group, reinforcement was concentrated exclusively within the strut region, arranged in a triangular configuration in accordance with the reinforcement recommendations provided in The ACI 318M-19 [9]. Additionally, angle steel sections were employed to provide supplementary support and confinement to the strut region.

All specimens within this group demonstrated consistent structural behavior throughout the loading process up to failure, exhibiting nearly identical cracking patterns and failure mechanisms. While minor variations were observed in the load levels at which the first cracks appeared, the initial cracking loads for all beams in this group were lower than those recorded for the control specimens (**G1-CO-1**) and (**G1-CO-3**). This suggests that although the triangular strut reinforcement may have provided adequate confinement within the strut region, it did not significantly enhance the beam's ability to resist initial cracking.

For the first specimen in this group, beam (**G4-HT-S-1**), the initial crack was observed at a load of 150 kN. This value represents a decrease of approximately 11.76% and 16.67% compared to the first-crack loads of the control specimens (**G1-CO-1**) and (**G1-CO-3**), respectively. The initial crack appeared on the inner face of the strut region. As the applied load increased, additional cracks formed in the tensile zone near the midspan of the beam. This progression is illustrated in Fig 4.12.



Figure 4.20 Cracks propagation for specimen G4-HT-S-1.

Beam (**G4-HT-S-2**) displayed very similar behavior to (**G4-HT-S-1**). The first crack appeared at a slightly lower load of 145 kN, marking a 14.7% and 19.4% reduction compared to both specimen (**G1-CO-1**) and (**G1-CO-3**), respectively. This crack originated at the same location as that of the previous beam on the inner face of the strut. Subsequent crack propagation occurred in the midspan tensile zone as the load increased, consistent with the behavior observed in (**G4-HT-S-1**). Refer to Fig 4.13 for visual documentation.

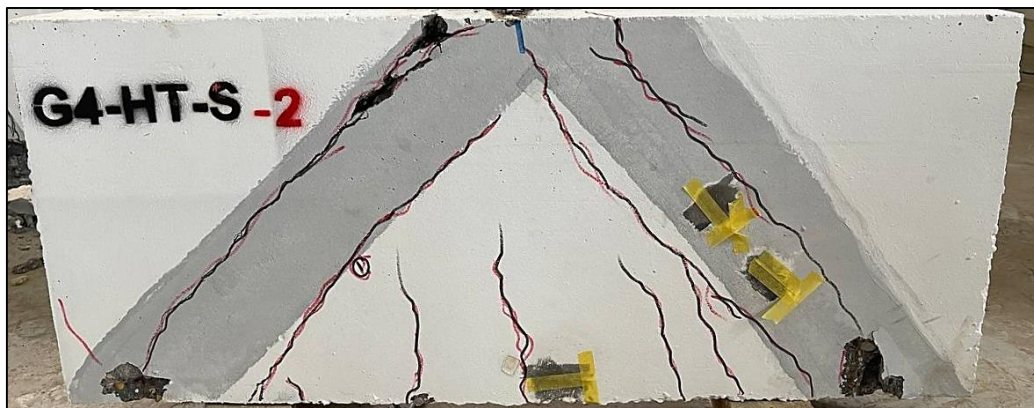


Figure 4.21 Cracks propagation for specimen G4-HT-S-2.

The third and fourth specimens, beams (**G4-HT-S-3**) and (**G4-HT-S-4**), also exhibited closely aligned behavior. In both beams, the initial crack developed at an identical load level of 140 kN, corresponding to a reduction of approximately 17.65% and 22.2% compared to the control specimens (**G1-CO-1**) and (**G1-CO-3**), respectively. Unlike the earlier beams in this group, the first crack in these

specimens occurred directly in the midspan tension zone, rather than initiating within the strut region. As loading progressed, cracking extended into the strut region, indicating the onset of stress redistribution and increased structural demand on this localized area. This sequence of cracking and damage propagation is shown in Figs.4.14 and 4.15.

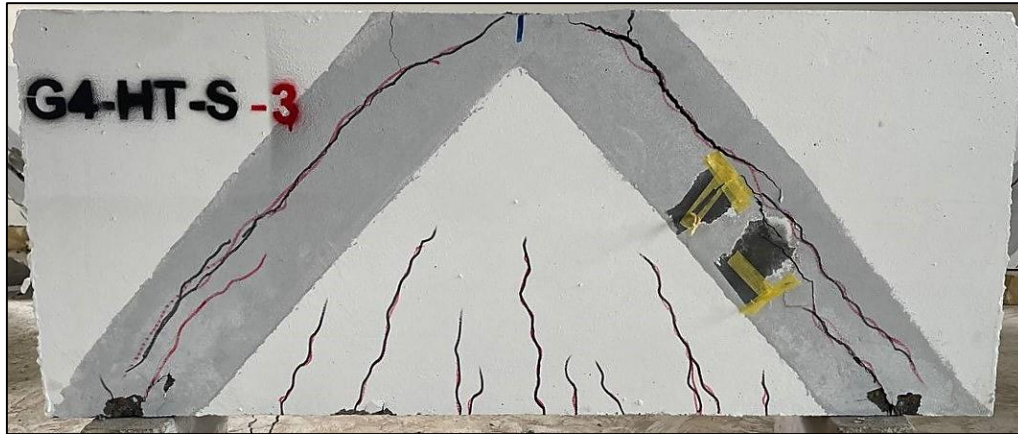


Figure 4.22 Cracks propagation for specimen G4-HT-S-3.

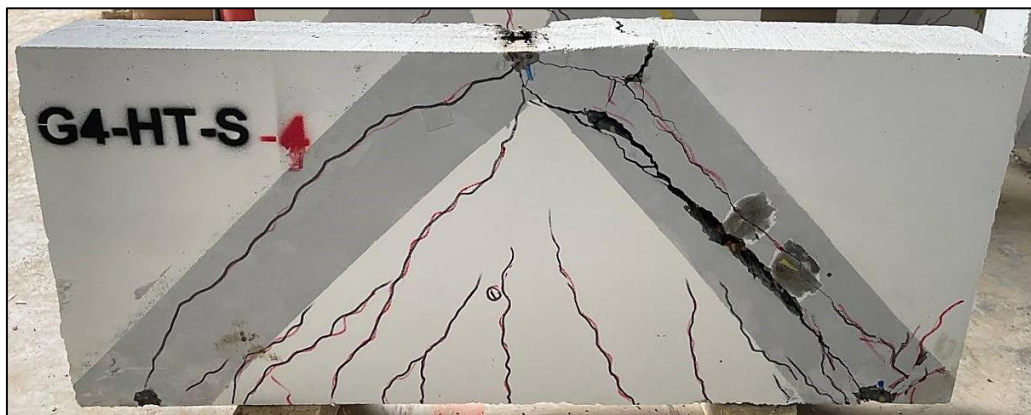


Figure 4.23 Cracks Propagation For (G4-HT-S-4).

Following the formation of the initial cracks and the emergence of secondary cracking in both the midspan tension zones and strut regions, all specimens in Group (G4) proceeded to exhibit very similar failure behavior under increasing load. As the beams approached their maximum load-carrying capacity, multiple cracks developed and propagated extensively throughout the strut region. These cracks intensified in number and width, ultimately resulting in failure

predominantly localized within the strut area. This consistent failure mode across all specimens in Group (**G4**) highlights the limitations of localized strut reinforcement, even when enhanced with steel angle sections. Although the reinforcement may have delayed damage progression within the strut to some extent, it was not sufficient to prevent failure in this critical region, especially under high shear and compressive stresses.

In conclusion, the groups exhibited variations in the first crack load. Some groups, such as group four **G4** and specimens **G2-HA-B-1** and **G2-HA-S-1**, demonstrated lower first crack loads compared to the control specimens. This behavior is attributed to the hybridization of concrete and the use of multiple reinforcement layers, which can result in the early initiation of cracks due to the different mechanical responses of the constituent materials. These variations hinder the ability of the composite system to act as a unified structure. Conversely, specimens that showed an increase in the first crack load benefited from modifications to the reinforcement approach in the tie region and the use of high-strength concrete in that area. Both of these factors have been confirmed by other researchers as contributing to improved crack resistance [53].

4.8 Concrete Surface Strain

To evaluate the strain behavior of the concrete under loading, strain gauges were installed on the surface of the specimens. These gauges were positioned at critical locations to capture the strain distribution and monitor the deformation characteristics of the concrete during the loading process, as illustrated in Fig.4.24. The recorded surface strain values for all tested specimens are summarized in Table 4.8, facilitating a comprehensive comparison of performance across different reinforcement and strut configurations.

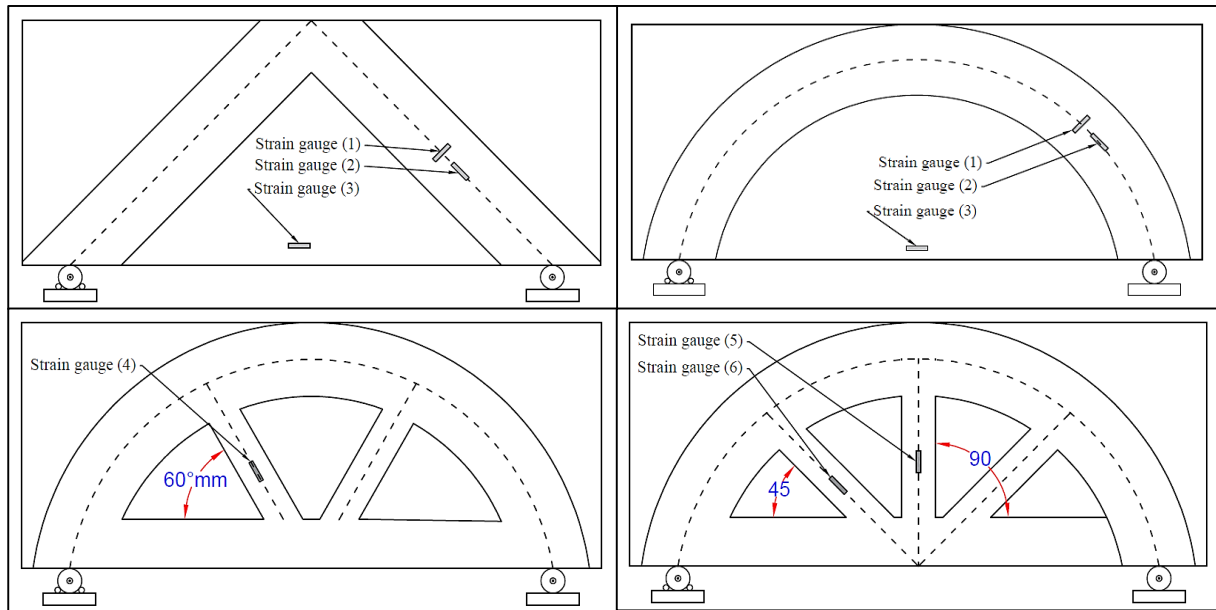


Figure 4.24 Strain gauges location.

Strain gauge (1): refer to Tensile Strain

Strain gauge (2): refer to Compressive Strain

Strain gauge (3): refer to tie Strain

Strain gauge (4,5 and 6): refer to ribs Strain

Table 4.8 The Concrete Surface Strain for All Tested Specimens.

Groups No.	No.	Specimens	Tensile Strain (mm/mm)	Compressive Strain (mm/mm)
G1	1	G1-CO-1	0.0008710	0.002830
	2	G1-CO-2	0.0006520	0.002950
	3	G1-CO-3	0.0003410	0.002025
	4	G1-CO-4	0.0005300	0.002100
G2	1	G2-HA-B-1	0.0003258	0.002787
	2	G2-HA-B-2	0.0006722	0.002959
	3	G2-HA-B-3	0.0004700	0.002495
	4	G2-HA-B-4	0.0007360	0.002399
G3	1	G3-HA-S-1	0.0007500	0.002070
	2	G3-HA-S-2	0.0006620	0.002025
	3	G3-HA-S-3	0.0003393	0.002920
G4	1	G4-HT-S-1	0.0002100	0.003110
	2	G4-HT-S-2	0.0002320	0.002000
	3	G4-HT-S-3	0.0004356	0.004048
	4	G4-HT-S-4	0.0001550	0.004981

4.8.1 Compressive strain

4.8.1.1 Strut strain

To calculate the compressive strain in the concrete within the strut region, strain gauge (2) was installed on all tested specimens, as illustrated in Fig 4.25. Among the tested groups, the fourth group recorded the highest strain values. This result is likely attributed to the effectiveness of the Strut-and-Tie Model (STM) system in facilitating efficient load transfer within the deep beam.

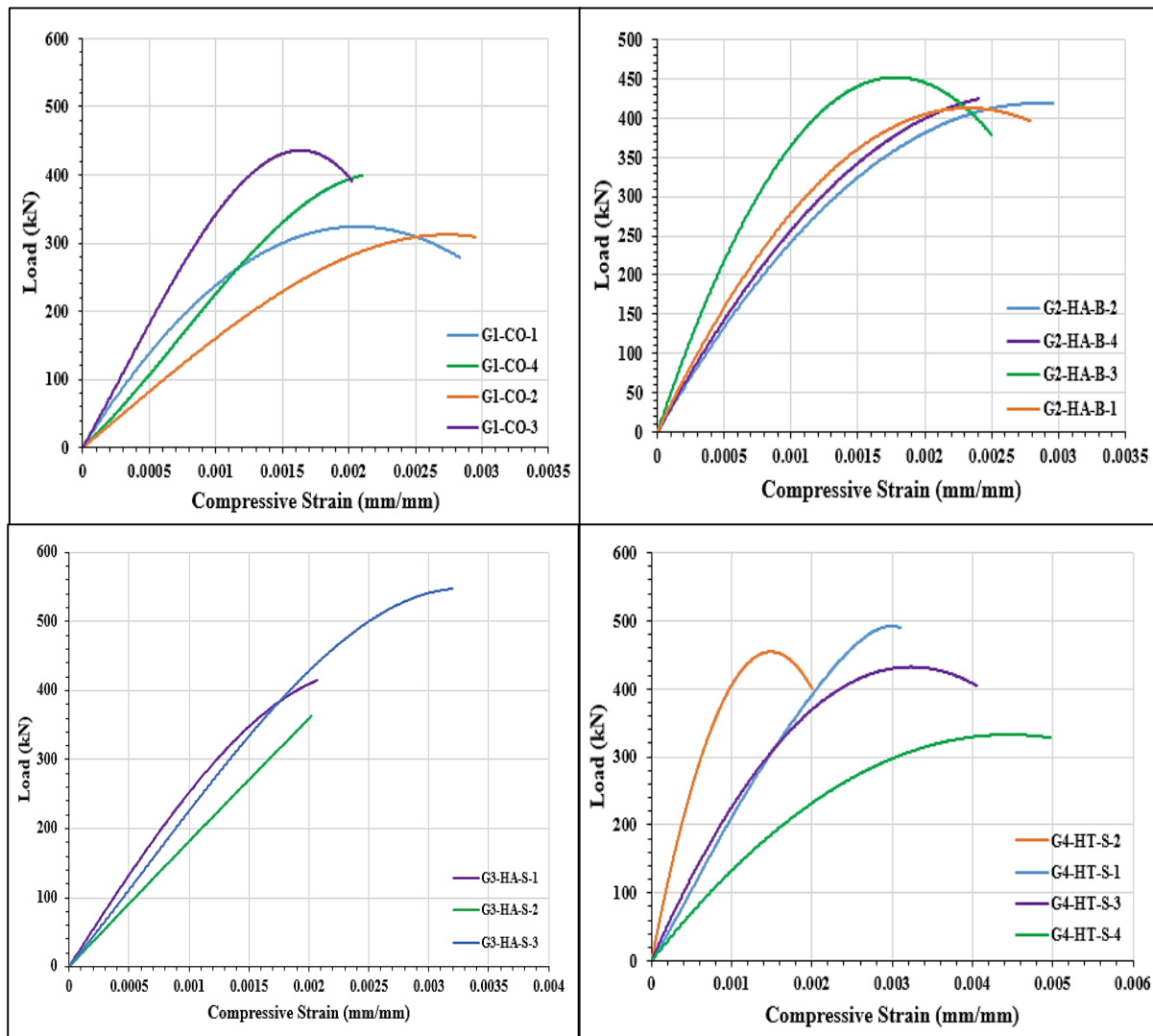


Figure 4.25 Compressive Strain For All Tested Specimens

4.8.1.2 Strut-Ribs strain

To investigate the influence of adding ribs to the strut arch and to assess the effect of rib orientation within the arch, strain gauges 4, 5, and 6 were installed

on the ribs. The results revealed that the strain experienced by the ribs varied according to their angle of inclination within the arch. The highest strain was recorded at an angle of 60° , with a value of 0.00221 mm/mm, followed by 45° with a strain of 0.00042 mm/mm, and 90° with a strain of 0.000221 mm/mm. These findings suggest that the angle of the ribs significantly affects their contribution to the overall strut behavior. Refer to Fig. 4.26 for details.

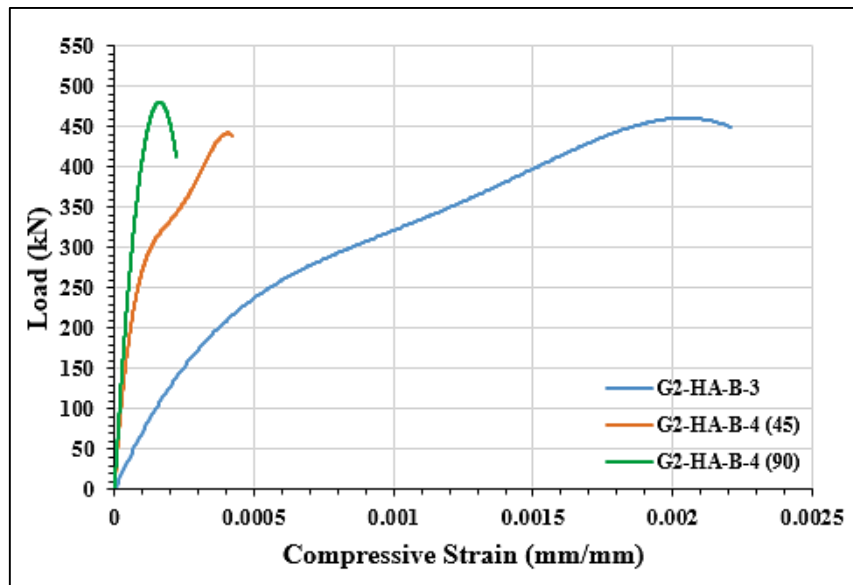


Figure 4.26 Compressive Strain at the middle of the ribs.

4.8.2 Tensile strain

When the strut region in a deep beam is subjected to compressive forces, the concrete tends to expand laterally due to Poisson's effect. This lateral expansion is a critical indicator of the material's proximity to failure. To measure the strain in this direction, Strain Gauge (1) was installed. Monitoring the tensile strain in this direction provides insight into the effectiveness of the confinement provided by angle steel sections or conventional stirrup reinforcement. Among all tested groups, Group 4 exhibited the lowest tensile strain in this region, indicating the superior confinement performance of the angle steel sections. The tensile strain results for all tested specimens are presented in Figure.4.27.

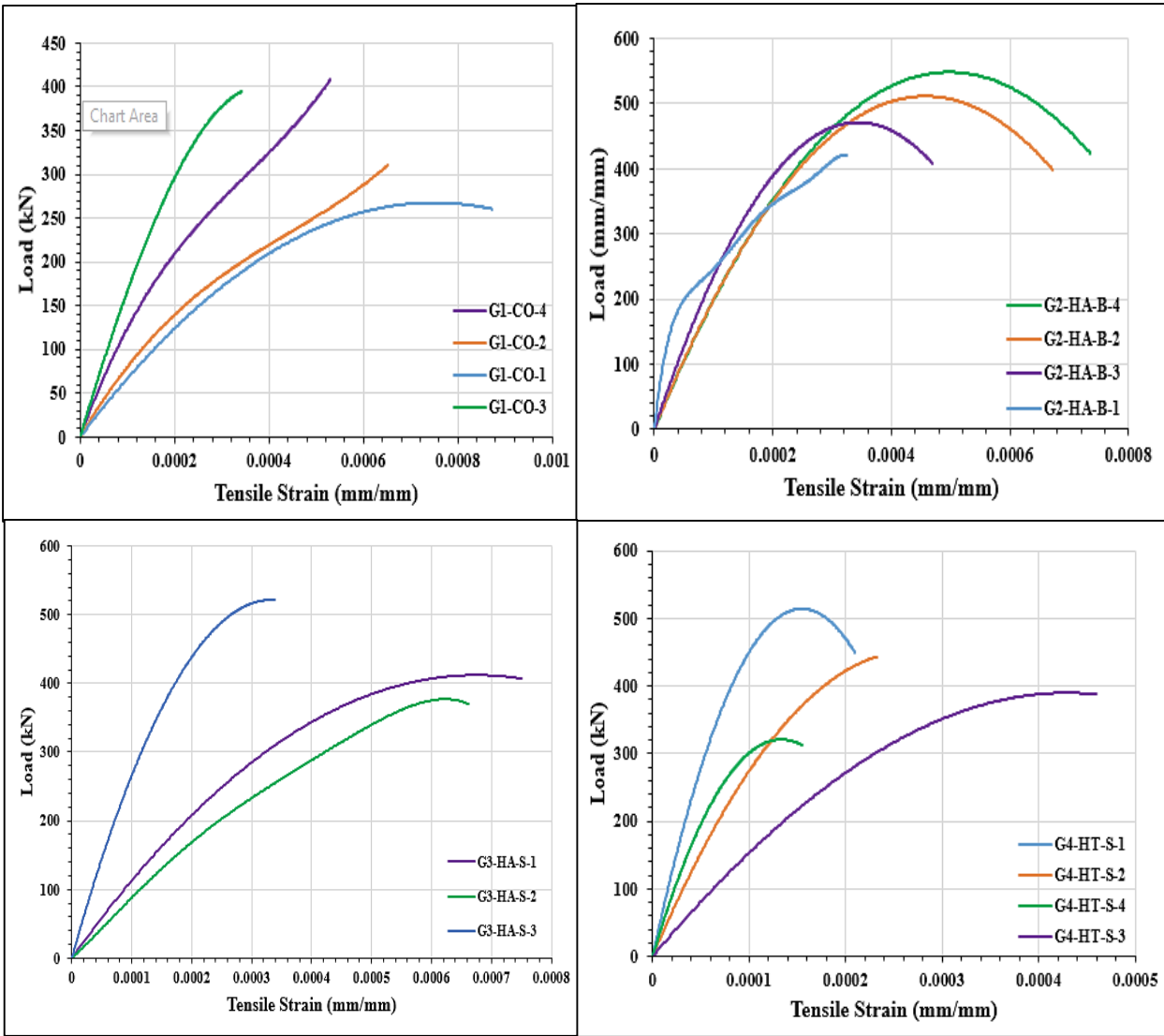


Figure 4.27 The tensile strain results for all tested specimens

CHAPTER FIVE: CONCLUSIONS AND RECOMMENDATIONS

5.1 Conclusions

This chapter presents the key conclusions derived from the investigation into the behavior of deep beams, focusing on the primary variables studied in this research: reinforcement type, hybridization method, and strut shape, as outlined below.

1. Altering the reinforcement shape in the strut region from triangular to arched resulted in an increase in load-bearing capacity of 10.7% for normal-strength concrete (G1-CO-1 vs. G1-CO-2) and 5.13% for high-strength concrete (G1-CO-3 vs. G1-CO-4), due to the arch action.
2. Moreover, changing the concrete type from normal-strength to high-strength concrete effectively enhances load-bearing capacity by 39.3% between specimens (G1-CO-1) and (G1-CO-3), and by 32.25% between (G1-CO-2) and (G1-CO-4). However, this improvement comes at the expense of increased weight and cost.
3. The second group of beams (G2), featuring a hybrid arch with conventional strut reinforcement, showed marked performance gains. Compared to G1-CO-2, capacity, stiffness, toughness, and ductility improved by 45.2%, 83.54%, 121.32%, and 38%, respectively. Against G1-CO-4, the gains were 9.75% in capacity, 50.62% in stiffness, 11% in toughness, and 14.36% in ductility.
4. In the third group (G3), which used angle steel sections for reinforcement, structural improvements were more pronounced. Relative to G1-CO-2, capacity increased by 74.2%, stiffness by 98.94%, toughness by 194%, and ductility by 38%. Compared to G1-CO-4, improvements included 31.7% in capacity, 63.25% in stiffness, 47.5% in toughness, and 14.36% in ductility.
5. The fourth group (G4), utilizing STM hybrid concrete with angle steel reinforcement, demonstrated the best overall performance. Compared to the

control beam G1-CO-1, load capacity increased by 75%, stiffness by 235.6%, toughness by 77.45%, and ductility by 116.4%. When compared to G1-CO-3, improvements were 25.6% in capacity, 77% in stiffness, 18.4% in toughness, and 96% in ductility.

6. Incorporating angle steel sections for strut reinforcement for the third group effectively increased the shear capacity of the beams, which was due to the arch action of the steel frame.
7. The use of ribs to strengthen the arched strut region contributes to enhancing load-bearing capacity; however, the effectiveness is influenced by the installation angle. In the second group, applying ribs at a 60° angle (G2-HA-B-3) resulted in a 4.65% increase in load bearing capacity, while a 45° angle (G2-HA-B-4) led to a smaller increase of 2.32%.
8. The use of normal-strength concrete, particularly with a compressive strength of 25 MPa in deep beams, contributed to local failure in high-stress regions such as the nodal zones due to crushing, as observed in the control specimens (G1-CO-1) and (G1-CO-2).
9. Hybridizing the tie region with high-strength concrete and modifying the reinforcement method using stirrups, as implemented in the second group of beams, significantly contributed to delaying the appearance of the first crack. The first cracking load improved by 33.3% compared to the control beam (G1-CO-2) and by 20% compared to the control beam (G1-CO-4).
10. Regarding the compressive strain in the ribs used in the second group, the highest strain was observed in ribs placed at a 60° angle, reaching 0.00221 mm/mm, followed by the 45° angle ribs with a strain of 0.00042 mm/mm. This aligns with the observation noted in point seven, confirming that as the angle increases, the ribs become more effective and contribute more significantly to carrying a portion of the arched strut loads.

5.2 Recommendation for Future Works

It is recommended that further research and investigation be conducted on the following set of problems, as addressing these issues could significantly contribute to advancing knowledge and improving outcomes in the field.

1. It is recommended that future studies investigate the use of alternative steel sections, such as channel sections, for strut reinforcement in deep beams. These studies should evaluate their influence on the overall structural behavior, including shear capacity and other key performance characteristics.
2. Conduct a comprehensive investigation into the influence of incorporating spiral stirrups within the reinforcement of strut regions, with the aim of evaluating their effectiveness in enhancing the structural integrity, confinement, and load-carrying capacity of these critical areas
3. Repeat the same procedure, but without using normal-strength concrete, and restrict the use of high-strength concrete to only the strut and tie regions. This will allow for a focused study of the structural behavior and performance of the concrete under applied loads.
4. Examine the structural behavior of non-prismatic deep beams under various loading conditions, with particular focus on their stress distribution, load transfer mechanisms, and potential failure modes, in order to better understand their performance and optimize their design.
5. The behavior of deep beams subjected to uniformly distributed loads warrants further investigation, particularly focusing on their performance and failure mechanisms when reinforced with angle steel sections. Future research should aim to deepen the understanding of how such reinforcement influences the structural response and ultimate strength of deep beams under these loading conditions.

APPENDICIES

APPENDIX A: DESIGN OF DEEP BEAM

Design of Concrete Deep Beams

Deep beams have been designed according to the design equations for the deep beam, based on ACI-19 code[9] chapter 23 (strut and tie method STM) and achieving the determinates of deep beam according to the chapter 9, section 9-9. Figure (A-1) shows description of strut-and-tie model.

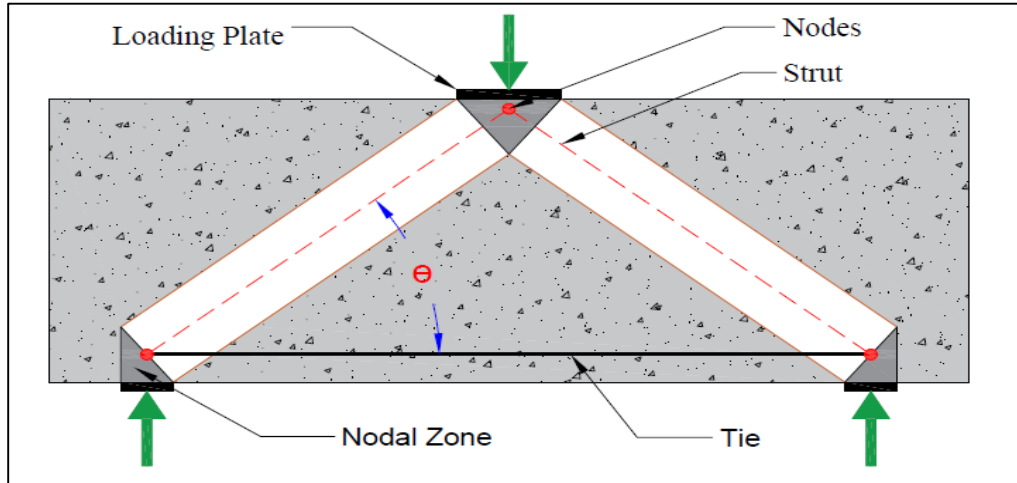


Figure (A-1) Description of strut-and-tie model (STM).

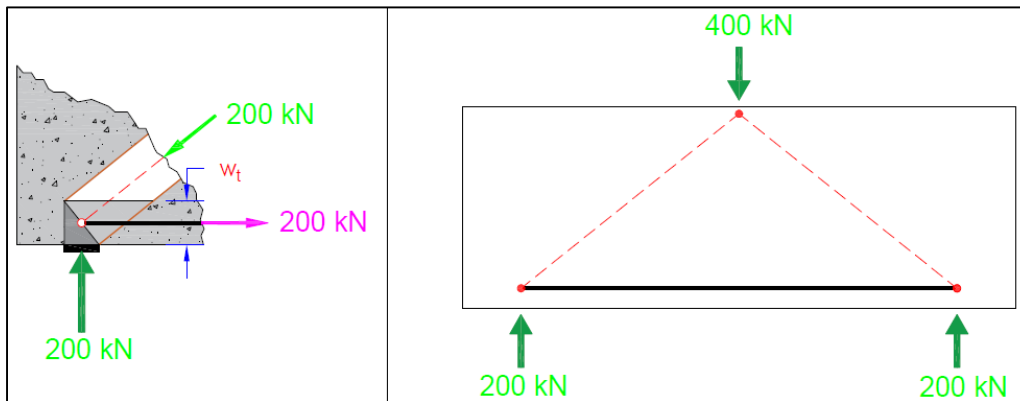


Figure (A-2) Forces analysis.

Beam Properties:

Length: 1200 mm

Height: 500 mm

Width: 150 mm

$L_n=1000\text{mm}$

$4h=4\times 500=2000\text{mm}$

$L_n < 4h \quad \therefore$ Deep Beam

W_{sb} : The width of strut at bottom

W_t : The effective tie width

W_{st} : The width of strut at top

Check the dimensions of section

$$V_n = (0.83) \times \sqrt{f'_c} \times b_w \times d \quad \text{ACI318M-19 [9.9.2.1]}$$

$$\phi V_n = \phi (0.83) \times \sqrt{f'_c} \times b_w \times d$$

$$\phi = 0.75 \quad \text{ACI318M-19 [21.2.1]}$$

f'_c = Compressive strength of concrete (MPa)

b_w = Width of concrete deep beam (mm)

d = Effective depth (mm)

Compute the effective compressive strength at struts and nodal points.

$$f_{ce} = 0.85 \times \beta_s \times \beta_c \times f'_c \text{ (at struts)} \quad \text{ACI318M-19 [23.4.3]}$$

$$f_{ce} = 0.85 \times \beta_n \times \beta_c \times f'_c \text{ (at nodal points)} \quad \text{ACI318M-19 [23.9.2]}$$

β_s : strut coefficient ACI318M-19 table [23.4.3.a]

β_c : strut and node confinement modification factor. ACI318M-19 table [23.4.3.b]

β_n : Nodal zone coefficient ACI318M-19 table [23.9.2]

Calculate θ : "the angle between the axis of any strut and any tie entering a

entering a single node shall be at least 25 degrees " ACI318M-19 [23.2.7]

Calculate the forces in all truss members

Design strength

$$F_{nt} = A_s f_y \quad \text{ACI318M-19 [23.7.2]}$$

$$F_{nt} = (F_{ut} / \phi)$$

F_{ut} : Force at tension zone

Compute main reinforcement

$$A_s f_y = (F_{ut} / \phi) \quad \text{ACI318M-19 [23.9.1]}$$

f_y = Yield strength of reinforcement, MPa

Compute minimum strut reinforcement

$$A_{vs} = 0.0025/(\sin\alpha)^2 \times b_w \times S$$

ACI318M-19 table [23.5.1.b]

Results:

$$b_w = 150 \text{ mm}, d = 475 \text{ mm}$$

$$P_u = 400 \text{ kN}$$

$$V_u = P_u/2 = 200 \text{ kN}$$

$$f'_c = 25 \text{ MPa}$$

$$\beta_s = 0.75$$

$$\beta_c = 1$$

$$\beta_n = 1 \text{ (C-C-C nodal)}, \quad \beta_n = 0.8 \text{ (C-C-T nodal)}$$

$$f_{ce} = 18.75 \text{ MPa (interior strut)}$$

$$f_{ce} = 20 \text{ MPa (nodal points)}$$

$$\phi V_n = \phi(0.83) \times \sqrt{f'_c} \times b_w \times d$$

$$0.75 \times V_n = 0.75(0.83) \times \sqrt{18.75} \times 150 \times 475$$

$$V_n = 256 \text{ kN} > V_u \text{ OK}$$

$$a = 500, d = 475 \quad a/d = 1.05$$

$$\theta = 45^\circ > 25^\circ$$

$$F_{ut} = 200 \text{ kN}$$

$$F_{nt} = A_s f_y$$

ACI318M-19 [23.7.2]

$$f_y = 400 \text{ MPa}$$

$$200 \times 1000 = A_s \times 400$$

$$A_s = 500 \text{ mm}^2$$

Use 2 Ø16 and 2 Ø12 as a tension reinforcement

$$(2 \times 113.04 + 2 \times 200.96) = 628 \text{ mm}^2 > A_s \text{ required} \quad \therefore \text{OK}$$

Use 4Ø8 as a shear reinforcement (at the strut region)

APPENDIX B: PRODUCT DATA SHEETS

BUILDING TRUST



PRODUCT DATA SHEET

Sika® ViscoCrete®-180 GS

Set retarding, high range water reducing & superplasticizing admixture

DESCRIPTION

Sika® ViscoCrete®-180 GS is a Set retarding, high range water reducing & superplasticizing admixture for Concrete & Mortar utilizing Sika's 'ViscoCrete®' polycarboxylate polymer technology (3rd Generation).

USES

1. High-performance Concrete (HPC).
2. Flowing Concrete.
3. Durable Concrete.
4. Pumped Concrete.

CHARACTERISTICS / ADVANTAGES

1. High water reduction, resulting in higher density, higher strength and reduced permeability.
2. Easier and faster pumping of concrete.
3. Increased workability and easier placeability.
4. Increased concrete durability and uniformity.
5. Reduced shrinkage and cracking.
6. Reduced rate of carbonation of the concrete.

PRODUCT INFORMATION

Composition	Aqueous solution of modified polycarboxylates
Packaging	1000 LTRs IBC 20 kg Pail
Shelf life	12 months from date of production if stored properly in undamaged unopened, original sealed packaging.
Storage conditions	In dry conditions at temperatures between +5°C and +35°C. Protect from direct sunlight. It requires recirculation when held in storage for extended periods.
Appearance and colour	Light brownish
Specific gravity	1.070 ± (0.02) g/cm ³
pH-Value	4 - 6

PRODUCT DATA SHEET
Sika® ViscoCrete®-180 GS
December 2022, Version 04.01
02130501 1000003885

TECHNICAL INFORMATION

Concreting guidance	The standard rules of good concreting practice, concerning production and placing, are to be followed. Laboratory trials shall be carried out before concreting on site, especially when using a new mix design or producing new concrete components. Fresh concrete must be cured properly and curing applied as early as possible.
---------------------	--

APPLICATION INFORMATION

Recommended dosage	(0.5 % - 2 %) by weight of total cementitious materials.
Dispensing	Sika® ViscoCrete®-180 GS is added to the gauging water or added with it into the concrete mixer. To take advantage of the high water reduction, a wet mixing time, which is depending on the mixing conditions and mixer performance, of at least 3 mins. per cubic meter after the admixture addition is recommended. Sika® ViscoCrete®-180 GS shall not be added to dry cement.
Compatibility	Sika® ViscoCrete®-180 GS can be used in conjunction with : 1. Sika® Aer 2. Sika® ViscoFlow® 3. Sika® ViscoCrete® 4. SikaPlast® 5. Sika® Retarder IQ 6. SikaFiber® 7. Sika® Plastocrete® N IQ All admixtures must be added separately. Trials are always recommended before combining products . For additional information, please contact Sika technical personnel.

BASIS OF PRODUCT DATA

All technical data stated in this Product Data Sheet are based on laboratory tests. Actual measured data may vary due to circumstances beyond our control.

IMPORTANT CONSIDERATIONS

1. A suitable mix design has to be taken into account.
2. Do not use Sika® ViscoCrete®-180 GS with naphthalene based admixtures.
3. Over dosage of Sika® ViscoCrete®-180 GS with excess water will cause :
 - Increase in air entrainment.
 - Bleeding & Segregation.
 - Extend Initial & Final setting time.

ECOLOGY, HEALTH AND SAFETY

For information and advice on the safe handling, storage and disposal of chemical products, users shall refer to the most recent Safety Data Sheet (SDS) containing physical, ecological, toxicological and other safety-related data.

Sika Iraq (Sika Trading LLC)
Erbil / Baghdad / Basra
Tel: +96 477 301 71451
info@iq.sika.com
iq.sika.com

LOCAL RESTRICTIONS

Please note that as a result of specific local regulations the declared data for this product may vary from country to country. Please consult the local Product Data Sheet for the exact product data.

LEGAL NOTES

The information, and, in particular, the recommendations relating to the application and end-use of Sika products, are given in good faith based on Sika's current knowledge and experience of the products when properly stored, handled and applied under normal conditions in accordance with Sika's recommendations. In practice, the differences in materials, substrates and actual site conditions are such that no warranty in respect of merchantability or of fitness for a particular purpose, nor any liability arising out of any legal relationship whatsoever, can be inferred either from this information, or from any written recommendations, or from any other advice offered. The user of the product must test the product's suitability for the intended application and purpose. Sika reserves the right to change the properties of its products. The proprietary rights of third parties must be observed. All orders are accepted subject to our current terms of sale and delivery. Users must always refer to the most recent issue of the local Product Data Sheet for the product concerned, copies of which will be supplied on request.

Sika ViscoCrete-180GS-en-IQ-(12-2022)-4-1.pdf

PRODUCT DATA SHEET
Sika® ViscoCrete®-180 GS
December 2022, Version 04/01
021301011000003885





MegaAdd MS(D)

Densified Microsilica

DESCRIPTION

MegaAdd MS(D) is a very fine pozzolanic, ready to use high performance mineral additive for use in concrete. It acts physically to optimize particle packing of the concrete or mortar mixture and chemically as a highly reactive pozzolan.

MegaAdd MS(D) in contact with water, goes into solution within an hour. The silica in solution forms an amorphous silica rich, calcium poor gel on the surface of the silica fume particles and agglomerates. After time the silica rich calcium poor coating dissolves and the agglomerates of silica fume react with free lime (CaOH_2) to form calcium silicate hydrates (CSH). This is the pozzolanic reaction in cementitious system.

STANDARDS

ASTM C1240

USES

MegaAdd MS(D) can be used in a variety of applications such as concrete, grouts, mortars, fibre cement products, refractory, oil/gas well cements, ceramics, elastomer, polymer applications and all cement related products.

ADVANTAGES

- High to ultra high strength
- High resistance to chlorides and sulfates
- Protection against corrosion
- Increased durability, longer service life for structures
- Enhanced rheology, control of mixture segregation and bleed
- Greater resistance to chemicals

TYPICAL PROPERTIES at 25°C

PROPERTY	TEST METHOD	VALUE
State	Amorphous	Sub-micron powder
Colour	-	Grey to medium grey powder
Specific Gravity	-	2.10 to 2.40
Bulk Density	-	500 to 700 kg/m ³
Chemical Requirements		
Silicon Dioxide (SiO_2)	-	Minimum 85%
Moisture Content (H_2O)	-	Maximum 3%
Loss on Ignition (LOI)	-	Maximum 6%
Physical Requirements		
Specific Surface Area	-	Minimum 15 m ² /g
Pozzolanic Activity Index, 7 days	-	Maximum 105% of control
Over size particles retained on 45 micron sieve	-	Maximum 10%

COMPATIBILITY

MegaAdd MS(D) is suitable for use with all types of cement and cementitious materials.

With Admixtures :

MegaAdd MS(D) is compatible to use with all types of water reducing plasticisers / superplasticisers and poly carboxylate based superplasticiser.

DOSAGE

The normal dosage of **MegaAdd MS(D)** is 5 - 8% by weight of cement, but it can be used up to 10%. Site trials should be carried out to establish the optimum dosage for the mix to be used as the dosage varies depending on application.



MegaAdd MS(D)

BATCHING	Batch MegaAdd MS(D) into the concrete mixer and mix thoroughly with the other mixture ingredients, adopting a procedure that ensures full dispersion of the product.	
PACK SIZE	600 Kgs and 1200 Kgs Jumbo bags	
GENERAL INFORMATION	Shelf Life	12 months from date of manufacture when stored under warehouse conditions in original unopened packing. Extreme temperature / humidity may reduce shelf life.
	Cleaning	Clean all equipments and tools with water immediately after use.
HEALTH and SAFETY	PPE's	Gloves, goggles and suitable mask must be worn.
	Precautions	Contact with skin, eyes, etc. must be avoided.
	Hazard	Regarded as non-hazardous for transportation.
	Disposal	Do not reuse bags. To be disposed off as per local rules and regulations.
	Additional Information	Refer MSDS. (Available on request.)
TECHNICAL SERVICE	CONMIX Technical Services are available on request for onsite support to assist in the correct use of its products.	



MSASA
Construction Solutions for Africa

CAPE TOWN
Tel: +27 (0)87 231 0253

Unit 5 | M5 Freeway Park
Upper Camp Rd | Maitland | 7405
Cape Town | South Africa

Email: info@msasa.co.za | www.msasa.co.za

JOHANNESBURG

Tel: +27 (0)82 785 8529

64 Maple Street | Pomona
Kempston Park | Johannesburg | 1619
South Africa

Manufacturer:
CONMIX LTD.
P.O. Box 5936, Sharjah
United Arab Emirates
Tel: +971 6 5314155
Fax: +971 6 5314332
Email: conmix@conmix.com

Sales Office:
Tel: +971 6 5682422
Fax: +971 6 5681442
www.conmix.com



It is the customer's responsibility to satisfy themselves by checking with the company whether information is still current at the time of use. The customer must be satisfied that the product is suitable for the use intended. All products comply with the properties shown on current data sheets. However, Conmix does not warrant or guarantee the installation of the products as it does not have any control over installation or end use of the product. All information and particularly the recommendations relating to application and end use are given in good faith. The products are guaranteed against any manufacturing defects and are sold subject to Conmix standard terms and conditions of sale.

REFERENCES

- [1] ACI-ASCE Committee 426, "The Shear Strength of Reinforced Concrete Members ", ACI Manual of concrete Practice, Part 4, 1985, pp 111.
- [2] Varghese P. C., and Krishnamoorthy C.S., "Strength and Behavior of Deep Reinforced Concrete Beams", Indian Concrete Journal, Vol.40, No.3, March 1966, pp.104-108.
- [3] ACI Committee 318, 2008, "Building Code Requirement for Structural Concrete (ACI 318-08) and Commentary," American Concrete Institute, Farmington Hills.
- [4] ACI Committee 318, "Building Code Requirements for Structural Concrete (318-08) and Commentary (318-08)", American Concrete Institute, Detroit, 2008.
- [5] Zhang, Z, Cheng-Tzu, Thomas Hsu, ASCE and Moren, J., "Shear Strengthened of Reinforcement Concrete Deep Beams Using Carbon Fiber Reinforced Polymer Laminate", Journal of Composite for Construction.Vol.8, No.5, October 2004, pp.403-414
- [6] Kalyanaraman, V., Y., Pao H., and Rayan, M.A., "Shear Tests of Deep Beams with Flanges", Journal of the Structural Division, ASCE, Vol. 105, No. ST12, Dec. 1979, PP. 2760–2766.
- [7] Nilson, A. H., and Darwin, D., "Design of Concrete Structures," McGraw-Hill International Editions, 12th Edition, 1997, pp. 151.
- [8] Russo, G., Venir, R., and Pauletta, M., "Reinforced Concrete Deep Beams - Shear Strength Model and Design Formula," ACI Structural Journal, Vol. 102, No.3, May-June, 2005, pp. 429-437.
- [9] ACI Committee 318-19, "Building Code Requirement for Structural Concrete and Commentary", American Concrete Institute, Farmington Hills, Michigan, 2019.

- [10] K. Sh. Mahmoud, "Nonlinear Analysis of Pre-stressed concrete Deep Beams", M.SC. Thesis, University of Technology, Iraq, 2004.
- [11] D.Birrcher, R.Tuchscherer, M.Huizinga, O.Bayrak, S.Wood and J.Jirsa,"Strength and Serviceability Design of Reinforced Concrete Deep Beams", CTR Technical Report, December, Center for Transportation Research at The University of Texas at Austin, 2009.
- [12] S. A. Hassan and A. H. Mheb," Behavior of High Strength Hybrid Reinforced Concrete Deep Beams under Monotonic and Repeated Loading" The Open Civil Engineering Journal, vol.12, 2008, pp. 263-282.
- [13] A.A. Abdel-Razzak, "The Effect of Low Shear Span Ratio on the Shear Strength of RC Beams",M.Sc. Thesis, University of Technology, Baghdad, (2001).
- [14] N.K. Subbedi, E.V. Alan, and N. Kubtatm," Reinforced Concrete Deep Beams-Some Test Results", Magazine of Concrete Research, Vol.38, No.137, Dec.1986, pp.206-219.
- [15] SHAKIR, Q. M., & ALGHAZALI, A. F. (2024). Behaviour of arched hybrid sustainable precast deep beams including green Concrete. *Journal of Materials and Engineering Structures «JMES»*, 11(1), 5-20.
- [16] Pereira, P.M., and Vieira, C.S. (2022). "A Literature Review on the Use of Recycled Construction and Demolition Materials in Unbound Pavement Applications". *Sustainability*. Vol. 14, No. 21.
- [17] Shakir, Q. M., & Hanoon, H. K. (2023). Behavior of high-performance reinforced arched-hybrid self-compacting concrete deep beams. *J Eng Sci Technol*, 18(1), 792-813.
- [18] ACI Committee 363 "Guide to Quality Control and Testing of High Strength Concrete (ACI- 363, 2R-98)", American Concrete Institute, Detroit, 1998.
- [19] Antoni, C. B., & Antoio, R. M. (2002). Shear Design of Reinforced High Strength Concrete Beams. Doctorial thesis, Barcelona.

- [20] Amornpinnyo, P., & Teerawong, J. (2014). Shear Behavior of Reinforced Concrete Deep Beams with Various Horizontal to Vertical Reinforcements and Shear Span-to-Effective Depth Ratios. *Advanced Materials Research*, 931, 473-477.
- [21] Suresh G.S., and Kulkarni S., "Experimental study on behavior of RC deep beams," *International Research Journal of Engineering and Technology (IRJET)*, Vol. 03, 2016, pp 676-680.
- [22] Ismail, K. S. (2016). Shear behaviour of reinforced concrete deep beams (Doctoral dissertation, University of Sheffield).
- [23] Demir, A., Caglar, N., and Ozturk, H. (2019). "Parameters Affecting Diagonal Cracking Behavior of Reinforced Concrete Deep Beams". *Engineering Structures*. Vol. 184, pp. 217-231.
- [24] Jabir, H.A., Mhalhal, J.M., Al-Gasham, T.S., and Abid, S.R. (2020). "Mechanical Characteristics of Deep Beams Considering Variable a/d Ratios: An Experimental Investigation". In *IOP Conference Series: Materials Science and Engineering*. Vol. 988, No.1.
- [25] Zhang, J.H., Li, S.S., Xie, W., and Guo, Y.D. (2020). "Experimental Study on Shear Capacity of High Strength Reinforcement Concrete Deep Beams With Small Shear Span–Depth Ratio". *Materials*. Vol. 13, No. 5.
- [26] Chen, H., Yi, W.J., and Zhou, K.J. (2022). "Diagonal Tension Cracking Strength and Risk of RC Deep Beams". *Buildings*. Vol. 12, No. 6.
- [27] El-hakeem R.A., Shoeib, A.E., Tawhead, W.F.M., and Arafa, A.N.M. (2022). " Evaluation of The Behavior of Hybrid GFRP/Steel Bars in Reinforced Concrete Deep Beams". *International Conference on Civil Engineering*. Vol. 2.
- [28] Ammash, H.K., and AL-Mousawi, M.M. (2021). "Effect of Development Reinforcement Strut in Concrete Deep Beam". *IOP Conference Series: Materials Science and Engineering*. Vol. 1076, No. 1.
- [29] Si, X.Y., Zhang, G.Y., Zheng, C., Xu, C.Y., Xu, H., and Wang, Y.L. (2022). "Experimental Study on Shear Behavior of Reinforced Concrete Deep Beams

With High-Strength Bars Under Uniform Load". In Structures Elsevier. Vol. 41, pp. 553-567.

- [30] Construction Industry Research and Information Association. (1977). CIRIA GUIDE 2: The Design Of Deep Beams In Reinforced Concrete.
- [31] Foster, S. J., & Gilbert, R. I. (1998). Experimental studies on high-strength concrete deep beams. *Structural Journal*, 95(4), 382-390.
- [32] Oh, J. K., & Shin, S. W. (2001). Shear strength of reinforced high-strength concrete deep beams. *Structural Journal*, 98(2), 164-173.
- [33] Yang, K. H., Chung, H. S., Lee, E. T., & Eun, H. C. (2003). Shear characteristics of high-strength concrete deep beams without shear reinforcements. *Engineering structures*, 25(10), 1343-1352.
- [34] Liu, S.B., & Xu, L. (2012). Experimental Study on Shear Behavior of Hybrid Fiber Reinforced High Performance Concrete Deep Beams. *Applied Mechanics and Materials*, 166-169, 664 - 669.
- [35] Aziz, O. Q., & Ali, M. H. (2013). Shear strength and behavior of ultra-high performance fiber reinforced concrete (UHPC) deep beams without web reinforcement. *Int. J. Civil Eng. Struct*, 2, 85-96.
- [36] Fahmi, H. M., AlShaarbaf, I. A., & Ahmed, A. S. (2013). Behavior of reactive powder concrete deep beams. *AL-Mansour Journal*, 20(1), 1-22.
- [37] Meleka, N. N., Bashandy, A. A., & Arab, M. (2014). Behavior and analysis of economically reactive powder RC beams. *Asian journal of civil engineering (BHRC)*, 15(5), 721-739.
- [38] Shuraim, A. B., & El-Sayed, A. K. (2016). Experimental verification of strut and tie model for HSC deep beams without shear reinforcement. *Engineering Structures*, 117, 71-85.
- [39] Yaseen, S. A. (2016). An experimental study on the shear strength of high-performance reinforced concrete deep beams without stirrups. *Eng. Technol. J*, 34(11 Part).

- [40] Ma, K., Qi, T., Liu, H., & Wang, H. (2018). Shear behavior of hybrid fiber reinforced concrete deep beams. *Materials*, 11(10), 2023.
- [41] Chen, B., Zhou, J., Zhang, D., Su, J., Nuti, C., & Sennah, K. (2022, May). Experimental study on shear performances of ultra-high performance concrete deep beams. In *Structures* (Vol. 39, pp. 310-322). Elsevier.
- [42] Abdul-Razzaq, K. S., Ali, H. I., & Abdul-Kareem, M. M. (2017). A new strengthening technique for deep beam openings using steel plates. *International Journal of Applied Engineering Research*, 12(24), 15935-15947.
- [43] Mhalhal, J. M., Al-Gasham, T. S., & Abid, S. R. (2020, December). Tests on reinforced concrete deep beams with different web reinforcement types. In *IOP Conference Series: Materials Science and Engineering* (Vol. 988, No. 1, p. 012032). IOP Publishing.
- [44] Chiriki, S. S., & Harsha, G. S. (2020). Finite element analysis of RC deep beams strengthened with I-section and truss reinforcement. *Materials Today: Proceedings*, 33, 156-161
- [45] Abadel, A. A., & Albidah, A. S. (2021). Investigation of shear reinforcement schemes for RC deep beams. *Arabian Journal for Science and Engineering*, 46, 4747-4763.
- [46] Chai, K. F., Woon, K. S., Wong, J. K., Lim, J. H., Lee, F. W., & Lee, Y. L. (2023). Experimental and numerical study of the strength performance of deep beams with perforated thin mild steel plates as shear reinforcement. *Applied Sciences*, 13(14), 8217.
- [47] Hassan, H. F. (2015). Behavior of hybrid deep beams containing ultra high performance and conventional concretes. *Engineering and Technology Journal*, 33(1), 30-50.
- [48] Ali, A. Y., & Zghair, M. G. (2015). Experimental investigation and nonlinear analysis of hybrid reinforced concrete deep beams. *Al-Qadisiyah Journal in Engineering Sciences*, 8(2), 99-119.
- [49] Hassan, S. A., & Faroun, G. A. (2016). Behavior of hybrid reinforced concrete deep beams under repeated loading. *Civil and Environmental*

Research, 8(10), 14-37.

- [50] Al-Bayati, N. A. (2018). Experimental Behavior of Hybrid Steel and Polypropylene Fiber Reinforced Concrete Deep Beam Containing Openings. *Engineering and Technology Journal*, 36(2 Part A).
- [51] Saad, A. Y., & Rasheed, L. S. (2018, November). Behaviours of hybrid deep beams with RPC Layers in the tension region. In *IOP Conference Series: Materials Science and Engineering* (Vol. 433, No. 1, p. 012032). IOP Publishing.
- [52] Sada, M. J. Saad (2021, February). Shear performance of hybrid concrete deep beams of trapezoidal section. In *IOP Conference Series: Materials Science and Engineering* (Vol. 1067, No. 1, p. 012015). IOP Publishing.
- [53] Ahmed, N. A. M., Khalil, A. H. H., & Mostafa, E. E. D. (2021). Behavior of Deep Beams using Different Concrete Grades. *International Research Journal of Innovations in Engineering and Technology*, 5(8), 75.
- [54] Yager, J., Hoult, N. A., Bentz, E. C., & Woods, J. (2022). Shear-critical deep beams with embedded functionally graded concrete struts. *ACI Structural Journal*, 119(6), 245-257.
- [55] Shakir, Q. M., & Hanoon, H. K. (2023). Behavior of high-performance reinforced arched-hybrid self-compacting concrete deep beams. *J Eng Sci Technol*, 18(1), 792-813.
- [56] Shakir, Q. M., & Hannon, H. K. (2023). A novel hybrid model of reinforced concrete deep beams with curved hybridization. *Jurnal Teknologi*, 85(2), 31-39.
- [57] Shakir, Q. M., & Hanoon, H. K. (2023, August). New models for reinforced concrete precast hybrid deep beams under static loads with curved hybridization. In *Structures* (Vol. 54, pp. 1007-1025). Elsevier.
- [58] Shakir, Q. M. (2023). New model of eco-friendly hybrid deep beams with wastes of crushed concrete. *Jurnal Teknologi*, 85(6), 145-154.
- [59] Shakir, Q. M., & Alghazali, A. F. (2023). Hybrid curved precast deep

beams composed partially from concrete made with recycled concrete aggregate. In E3S Web of Conferences (Vol. 427, p. 02025). EDP Sciences.

- [60] SHAKIR, Q. M., & ALGHAZALI, A. F. (2024). Behaviour of arched hybrid sustainable precast deep beams including green Concrete. Journal of Materials and Engineering Structures «JMES», 11(1), 5-20.
- [61] Shakir, Q. M., & Alghazali, A. F. (2024). Sustainable precast composite deep beams including concrete with partial replacement (50%) of recycled coarse aggregate.
- [62] Iraqi specifications 5/2019: Portland Cement. Central Organization for Standardization and Quality Control Iraq (in Arabic).
- [63] Iraqi Specification No.45, "Natural Sources for Gravel that is used in concrete and construction", Baghdad, 1984.
- [64] Iraqi specifications 1703/2018: Water Used for Concrete. Central Organization for Standardization and Quality Control Iraq (in Arabic).
- [65] ASTM C1240-03, "Standard Specification for the Use of Silica Fume as a Mineral Admixture in Hydraulic Cement Concrete, Mortar and Grout", Vol. 4.2, 2003, pp. 6.
- [66] ASTM C494/C494M-13, "Standard Specification for Chemical Admixtures for Concrete", Annual Book of ASTM Standard, 2013
- [67] Standard Specification for Deformed and Plain Carbon-Steel Bars for Concrete Reinforcement, ASTM A615/A615M-20, 2020
- [68] ASTM International Committee E-28 on Mechanical Testing. (2021). Standard test methods for tension testing of metallic materials. ASTM international.
- [69] AWS., D. (1978). Structural welding code-Steel. Mar Lin.
- [70] Standard Test Method for Slump of Hydraulic-Cement Concrete, ASTM C143-17, 2017.

- [71] Standard Practice for Making and Curing Concrete Test Specimens in the Field, ASTM C31/C31M-21a 2021.
- [72] Standard Test Method for Splitting Tensile Strength of Cylindrical Concrete Specimens, ASTM C496/C496M-17,2017
- [73] ASTM C78-09, Standard Test Method for Flexural Strength of Concrete (Using Simple Beam with Third-Point Loading), 2009.
- [74] ASTM C469/C469M-14, "Standard Test Method for Static Modulus of Elasticity and Poisson's Ratio of Concrete in Compression", Annual Book of ASTM Standard, 2014.
- [75] Jaafer, A. A., Al-Bazoon, M., & Dawood, A. O. (2020). Structural topology design optimization using the binary bat algorithm. *Applied Sciences*, 10(4), 1481.
- [76] Shakir, Q. M., & Abd, B. B. (2020). Retrofitting of self compacting RC half joints with internal deficiencies by CFRP fabrics. *Jurnal Teknologi (Sciences & Engineering)*, 82(6), 49-62.
- [77] Shakir, Q. M., & Kamonna, H. H. (2018). The behavior of high strength self-compacting reinforced concrete corbels strengthened with NSM Steel Bars. *Int. J. Adv. Sci. Eng. Inf. Technol*, 8(4), 1022-1028.
- [78] Shakir, Q. M., & Alliwe, R. (2021). Strengthening the self-compacting reinforced concrete dapped ends with near surface mounted (NSM) steel bar technique. *Int. J. Adv. Sci. Eng. Inf. Technol*, 11(2), 663-673.
- [79] MacGregor, J. G., Wight, J. K., Teng, S., & Irawan, P. (1997). *Reinforced concrete: Mechanics and design* (Vol. 3). Upper Saddle River, NJ: Prentice Hall.
- [80] Shakir, Q.M. and Hamad, S.A. (2021). "Behavior of Pocket-Type High-Strength RC Beams Without or With Dapped Ends". *Practice Periodical on Structural Design and Construction*. Vol. 26, No. 4.

الخلاصة

تبحث هذه الدراسة عملياً في تأثير أنظمة التسليح البديلة لمقاومة القص على الأداء القصي للعتبات العميقة. كما تهدف إلى تحديد التوزيع الأمثل لأنواع الخرسانة في العتبات العميقة الهجينة بهدف تقليل التكلفة والوزن مع الحفاظ على السلامة الإنشائية. تم صب خمسة عشر نموذجاً من العتبات العميقة بأبعاد موحدة بلغت 1200 مم طولاً، 500 مم عمقاً، و150 مم عرضاً. خضعت جميع النماذج لاختبار التحميل بنقطة واحدة، مع الحفاظ على نسبة ثابتة بين فضاء القص والعمق الفعال ($a/d = 1$). تضمنت المتغيرات الرئيسية في هذه الدراسة شكل ونوع التسليح المستخدم في منطقة الدعامة، بالإضافة إلى دمج أنواع مختلفة من الخرسانة (الخرسانة الهجينة). وقد تم استخدام الخرسانة عالية المقاومة في مناطق الإجهاد المرتفع مثل الدعامة، وأضلاع الدعامة، ومنطقة الشد، في حين استُخدمت الخرسانة العادية في بقية المناطق في العتبة. تم تقسيم النماذج إلى أربع مجموعات. المجموعة الأولى، والتي مثلت العتبات الضابطة، شملت أربع عتبات بتسليح دعامة تقليدي؛ اثنتان منها بتسليح مثلث الشكل واثنتان بتسليح مقوس، مع استخدام إما الخرسانة العادية أو الخرسانة عالية المقاومة في كل زوج. أما المجموعة الثانية فقد احتوت على أربع عتبات عميقة هجينة بتسليح مقوس تقليدي، اختلفت فيما بينها في عدد الأضلاع المضافة لدعم فعالية القوس وفي طرق تسليح منطقة الشد. تميزت المجموعة الثالثة بتهجين مقوس و تسليح باستخدام مقاطع حديد الزاوية بقياس (40×40×4) ملم بدلاً من التسليح التقليدي للدعامة. وقد اختلفت هذه النماذج من حيث كمية الحديد المستخدم وإدخال أضلاع من مقاطع حديد الزاوية. أما المجموعة الرابعة فقد ضمت أربع نماذج ذات تهجين مثلث الشكل و تسليح باستخدام مقاطع حديد الزاوية، واختلفت من حيث كمية الحديد المستخدم ومدى استبدال جزء من تسليح الشد بهذه المقاطع. أظهرت العتبات الهجينة ذات التسليح المقوس تحسينات مقارنة بالعتبة الضابطة المصنوعة من الخرسانة العادية في كل من: حمل التشقق الأولي، سعة التحميل النهائية، والصلابة، واللدونة، وامتصاص الطاقة، بنسب بلغت 33.3%، 74.2%، 99%، 40%، و108.3% على التوالي. وعند مقارنتها بالعتبة الضابطة المصنوعة من الخرسانة عالية المقاومة، كانت نسب التحسن 20%، 31.7%، 63.3%، 16%، و30.4% على التوالي. أما العتبات الهجينة ذات التسليح المثلث فقد أظهرت تحسينات في سعة التحميل النهائية، والصلابة، واللدونة، وامتصاص الطاقة بنسبة 75%، 235.6%، 116.4%، و77.2% على التوالي مقارنة بالعتبة الضابطة ذات الخرسانة العادية المقاومة، وبنسب 25.6%، 77%، 96%، و51.8% على التوالي مقارنة بعتبة الخرسانة عالية المقاومة الضابطة.



جمهورية العراق
وزارة التعليم العالي والبحث العلمي
كلية الهندسة/ جامعة ميسان
قسم الهندسة المدنية

سلوك العتبات العميقة ذات الدعامات المتضمنة الخرسانة المُتدرجة وظيفيًا

من قبل

حسين كريم هاشم

بكالوريوس هندسة مدني 2017

رسالة

مقدمة الى كلية الهندسة في جامعة ميسان

كجزء من متطلبات الحصول على درجة الماجستير في علوم الهندسة المدنية / الانشاءات

ذو الحجة 1446 هـ

بإشراف

الأستاذ الدكتور: عبد الخالق عبد اليمه جعفر

الأستاذ المساعد الدكتور: حيدر عبد راضي